Progress and challenges in using sustainable carbon anodes in rechargeable metal-ion batteries

Niloofar Soltani, Amin Bahrami, Lars Giebeler [*], Thomas Gemming, Daria Mikhailova [*]

Leibniz Institute for Solid State and Materials Research (IFW) Dresden e.V., Helmholtzstr. 20, 01069 Dresden, Germany

A B S T R A C T

Rechargeable lithium-ion batteries (LIBs) are one of the most promising alternatives to effectively bypass fossil fuels. However, long-term energy application of LIBs could be restricted in the future due to the increased production cost of LIB arising from the shortage and inaccessibility of Li in the Earth's crust. Na or K have been considered as substitutes for Li but in spite of their natural abundance, they suffer from low gravimetric/volumetric energy density. An alternative to increase the efficiency of sodium-ion battery (SIBs) and potassium-ion battery (KIBs) is to focus on finding the high-performing negative electrode, the anode. The large volume changes of alloying and conversion type anodes for KIBs and SIBs make hard carbons to a better option on this regard than usual graphitic carbons, but a key obstacle is the reliance on unsustainable sources. Thus, biomass-derived carbon could offer a promising alternative, and it has indeed been in the focus of much recent work. This review highlights the recent advances in using carbon extracted from various biomass sources in rechargeable Li-, Na-, and K-ion batteries. Maximizing the energy and power densities as well as the lifetime of carbon anodes require an exploration of the right balance between carbon structures, pore morphology, chemical composition and alkali metal-ion storage. Thus, in this review, first, we take stock of key challenges and opportunities to extract carbon from various plants structural components and identify the extracted carbon structure compared to graphite-like structure. Then, we provide an overview on morphological and structural modification of the extracted carbons. Finally, we show how the physicochemical properties, structural alignment and morphological variation of the biomass-derived carbon can affect the storage mechanism and electrochemical performance. The extensive overview of this topic provided here is expected to stimulate further work on environmentally friendly battery design and towards the optimization of the battery performance. Electrode materials in alkali-metal-ion batteries that are based on biomass-derived carbon may allow not only a technical breakthrough, but also an ethically and socially acceptable product.

1. Introduction

Modern societies rely on exhaustible and unequally distributed fossil fuels to satisfy the high demand for electrical energy. But this reliance is associated with a high cost – anthropogenic global warming [1,2] – which has triggered the search for cleaner and more sustainable energy sources [3–9]. Rechargeable LIBs are one of the most promising alternatives in this regard. Their high energy and power densities make such batteries amenable for diverse applications, from portable electronic devices to medium- and large-scale systems in the automotive industry to grid support [1]. However, the application of LIBs is limited by some barriers such as safety considerations, uniformity of Li in Earth's crust, durability, and specially by the fabrication costs [1,10]. The costs of LIB

production could be cut by considering alternative raw materials, optimizing manufacturing schemes, reducing inactive material in the battery, and replacing expensive materials, such as rare-metal-containing inorganic compounds in electrodes and expensive polymers used as separators [11]. Furthermore, cheaper and sustainable raw materials can be refined to substitute for classical battery components. In that context, rechargeable sodium-ion batteries (SIBs) could replace LIBs, especially in large-scale storage devices, because Na is relatively cheaper and more abundant than Li. However, Na introduces some limitations because of its: 1) greater molecular weight and ionic radius than Li, 2) weaker binding to graphite as compared with Li, 3) higher standard reduction potential (-2.71 V vs. standard hydrogen electrode (SHE)), as compared with ~ -3.04 V for Li, and 4) lower gravimetric capacity (1165

mAh/g as compared with 3829 mAh/g for Li) [12]. Potassium (K) is another alternative for Li, and is used in potassium-ion batteries (KIBs). K is abundant in the Earth's crust (and thus relatively cheap) and has a low standard reduction potential (-2.93 V). It also has a high electrical conductivity, high rate of electron transfer between intercalated K atoms and the graphite layer, and fast ion-transportation kinetic in electrolyte as compared with Na cations [13,14]. Nevertheless, K also has some limitations that hinder its effective use in a technically relevant application. These include: i) poor ion diffusivity in the solid electrode, ii) large graphite volume change during cycling (∼ 61%), iii) severe consumption of electrolyte given the low electrochemical potential of K^+/K in propylene carbonate, iv) persistent tendency to deposit in dendritic form, and v) limited energy and power density because of its high atomic mass [15,16].

Another possibility is to focus on the negative electrode, or anode, in batteries. Typically, graphite is the most widely used form of carbon that forms anodes in batteries: it is able to react reversibly with Li with a theoretical specific capacity of 372 mAh/g vs. Li^+/Li. Highly crystalline graphite can host up to one Li atom per six C atoms. The low theoretical specific capacity can originate from the Coulomb repulsion between Li ions in nearest-neighbor sites. Because this is larger than the binding energy of Li to the graphite, nearest-neighbor sites cannot be occupied by Li [17,18]. Therefore, researchers were motivated to use hard carbon (non-graphitizable carbon) with capacities larger than that of graphite. Hard carbons show better electrochemical performance than that of graphite because of their relatively good cyclability, morphology that is tailorable to the initial organic precursors and processing temperature, and their ability to accommodate a much higher amount of Li than graphite. The latter can be attributed to the presence of hydrogen (H) and a large fraction of single graphene sheets, which allow the adsorption of a large amount of Li on both sides of the single-layer sheets [19]. In addition, the poorly or non-graphitizable carbons, owing to their large interlayer distance (d_{002}-spacing) and high porosities, can resolve the intercalation and extraction of Na^+ and K^+ ions to an extent [20].

A sustainable yet cost-effective alternative is to use biomass-derived materials obtained via low-cost chemical processes in the anode. Biomass includes agricultural residues and animal or wood wastes. Based on the nature of the biomass, the pyrolysis temperature and pre- or post-processing procedures can be optimized to fabricate high-quality, porous carbonaceous materials with channels and interstitial sites. In point of fact, biomass materials make it possible to avoid using expensive templates and, in most cases, environmentally harmful post-removal process. For example, the pyrolysis of residues from pulp-paper production and the influence of functional groups and molecular subunits in the polymeric structure is roughly described to show their amazing and porosity-directing influence. During pyrolysis, oxygen from the functional groups in cellulosic and hemicellulosic biomass transforms easily into H_2O, CO and CO_2 and enables an easier activation and generation of micropores. By contrast, the aromatic subunits in lignin conduct to form nonporous carbon despite the presence of oxygen-containing groups, because these are less effective in pore creation [21,22]. The dimensions of these porous systems ranging from macro- to meso- to micropore can be tuned to enable a particular design to be used in practical application. Therefore, extensive efforts have been undertaken to make this process a low-cost, high-volume, and commercially sustainable one. However, the distinct structure and different reactivity of hemicellulose, cellulose, and lignin to temperature result in different decomposition rates during the pyrolysis process, which makes the study of their carbonization mechanism rather challenging [21,23,24].

The physical and chemical characteristics of biomass-derived carbons, such as (hierarchical) porosities, crystallinity, and morphology, directly affect their electrochemical performance. Therefore, the optimization of processing parameters such as pyrolysis temperature, acid or base treatment, reaction time, and doping elements considerably affect the efficiency of the electrode and, hence, that of the eventual battery.

However, the industrialization of biomass-based hard carbon production faces some obstacles. These include the low initial Coulombic efficiencies of hard carbons used in batteries, resulting from an over-proportionated formation of the solid-electrolyte interphase (SEI); low carbon yield of the biomass precursors; and their chemical diversity. Therefore, by knowing better the biomass structure and its composition, surface modification of extracted carbon by eliminating adsorbed molecules and oxygenated groups bonded to the carbon and optimization of electrolytes as well as understanding of the structure and function of the SEI in alkaline ion batteries, we help to facilitate the industrialization of the biomass anodes into batteries system.

Here, we review recent advances in understanding the intercalation behavior of the metal cations Li^+, Na^+, and K^+ in graphite and the potential of biomass-derived carbons as anode materials. Although, the behavior of metal-ion storage differs based on the biomass used, the good performance of biomass-derived carbon with expanded graphite demonstrates its potential applicability as electrode material. The review will explore how the structure, porosity, and surface chemistry of the biomass-derived hard carbon can be tailored by simple synthesis methods to enable metal-ion storage. It will also explore how single- and multi-element doping of N, P, B, and F could enhance the performance of the produced carbon as anode material.

2. Structural forms of carbon

Carbon shows unique versatility of its bonding chemistry among the elements. Free carbon atoms have the valence configuration of $2s^2\ 2p^2$. These four valence electrons can be hybridized in three configurations of sp^1, sp^2 and sp^3. The ability to hybridize s- and p-orbitals results in various types of chemical bonds that eventually lead to the formation of various crystalline and disordered structures. In the sp^3-configuration, the coordination of the four hybrid orbitals toward the four corners of a regular tetrahedron leads to the formation of a strong σ bond with an adjacent atom. In the sp^2 configuration, three sp^2-orbitals are occupied by three electrons, each pointing to one of the vertices of a triangle and forming σ bonds, whereas the fourth electron is located in the p_z orbital that is perpendicular to the plane of the σ bonds [25–27].

The two most common natural crystalline forms of carbon, graphite and diamond, exhibit dramatic differences as a result primarily of short-range order [28].

Diamond-like structures possess a covalently bonded face-centered cubic structure, which consists of fully saturated sp^3-bonded carbon atoms with a density of 3.515 g/cm^3. By contrast, graphite, with a density of 2.267 g/cm^3, consists of covalently-bonded atoms in a hexagonal structure of sp^2-sites bound together by weak Van-der-Waals forces provided by π orbitals. Due to the high surface area of graphene layers and π-π interactions between them, the stacking these layers is unavoidable. This stacking results in a low surface area of graphene with a poor energy-storage performance [29]. Therefore, some spacers such as metal oxides [30], conducting polymers [31], carbon black [32], or carbon nanotubes (CNTs) [33] are introduced into the interlayer spaces.

Graphite occurs naturally, is mined and subsequently purified via hydrofluoric acid, but its reserves are limited. It can also be produced artificially by coking natural pitches or residues of crude-oil distillation by heating in the absence of air. The coke obtained after this long and complex process is calcined and extruded or molded to form rough blocks of the desired shape. After the density of the blocks has been adjusted by reimpregnation and several baking processes, the material is converted to graphite at around 3000°C by passing a current through a conducting coke bed surrounding the blocks. The need for high-energy heat treatment means that synthetic graphite for use as anode material is currently twice as expensive as treated natural graphite [34]. Battery-grade graphite used in lithium-ion anodes is typically a mixture of synthetic and natural graphite [35].

Unlike crystalline carbon or highly ordered graphite, which is formed by ABAB-stacked graphene, the turbostratic carbon with

disordered multilayered graphene domains co-exists with various proportions of sp²- and sp³-hybridization. In this kind of carbon, the presence of strong crosslinks between the disoriented and few layered graphene domains inhibits the rearrangement of the disoriented layers into a more parallel structure [25–27], [36,37]. Glassy and pyrolytic carbons obtained from organic polymer and hydrocarbon gas, respectively, are two examples of turbostratic carbons [38]. Carbon quantum dots (CQDs) of less than 10 nm in size and graphene quantum dots (GQDs) with structures smaller than 100 nm in size and less than 10 layers thick [39,40] are also classified into this category. CQDs are composed of turbostratic carbon and a nanocrystalline core with sp²-hybridized carbon while GQDs with similar structures compared to CQDs have higher crystallinity [41,42]. Extracted carbon from agricultural biomass with disordered structure is also considered in the family of turbostratic carbons. Biomass as the less expensive source of carbon compared to polymer and hydrocarbon gas, plays the leading role for production of disorder carbons. However, due to complex structure of biomass, a deep understanding of its structural and chemical characteristics is required to optimize extraction process of disordered carbon with high carbon content and optimum porosity.

2.1. Biomass-derived carbon

Biomass, the oldest renewable source of stored energy according to its biological diversity, source and origin, is classified into four categories: wood, crops, seaweed, and animal wastes. All types of biomass receive their energy, directly or indirectly, from photosynthesis, during which plants convert sunlight, water, and CO_2 to oxygen and carbohydrates. Subsequently, the consumption of carbohydrates as food by animals and humans provide them with nourishment [43]. Biomass contains a type of turbostratic carbon that can be obtained in a cheaper and environmentally more friendly way than carbon extracted from fossil sources [44]. In addition, extracting carbon from biomass is cheaper than extracting it from rare-metal-bearing inorganic compounds, and has thus received greater attention in recent years [45]. Such hard carbon with a disordered microstructure can accommodate substantial amounts of Na and K ions between its enlarged interlayers, and it can thus function as highly efficient anode material. This section provides a detailed information of the structure of biomass and the pyrolytic behavior of each main component of biomass as carbon sources.

2.2. Biomass structure

Cell walls of plants are composed of essentially three organic compounds: cellulose, hemicellulose, and lignin (Fig. 1). Each compound has its own characteristics. Hemicellulose and lignin show only short-range ordering, whereas cellulose is crystalline. The proportion of these compounds change with species, the plant part they belong to, the nature of the cells, and the geographic location [46,47].

Since each species has different proportions of compounds and each compound possesses an individual amount of carbon, the total carbon content varies for various biomass. In woody plants, organs with higher lignin content (e.g. stems) tend to have a higher carbon content than organs with lower lignin content (e.g., leaves, roots, and reproductive organs). Also, in herbaceous plants, more carbon content is found in leaves than in stems and roots [49]. The carbon content in each plant organ also depends on the age of the plant [50]. In general, woody plants, because of their relatively low growth rate, exhibit higher carbon content than herbaceous plants. On average, dried biochar from wood and wood-agricultural residue contain 52 wt.% carbon, whereas herbaceous and agricultural biomass contain 49 wt.% carbon. However, among the sources of agricultural biomass, some materials with the higher biochar yields content than that in woody plants, such as walnut shells, olive husk, and coconut shells containing 55, 58, and 51 wt.% carbon respectively exist [51,52].

Biomass with varying contents of hemicellulose, cellulose, and lignin can be thermally decomposed using different process parameters to tailor surface chemistry, structure, total carbon content, and pore morphology of the resulting carbon.

Despite the higher C/O ratio of lignin as compared with the other components, biomass-derived carbon with higher cellulose content shows greater potential for porosity formation but not necessarily behaves proportional. The porosity of char due to evaporating compounds is governed by the crystallinity, morphology, and functional groups of cellulose [49,53–56]. Following example shall demonstrate the influence of a nearly similar cellulose content on specific surface area of the extracted carbon. Cotton seed hair and paper with a cellulose content of 80-95 % and 85-99 % could be considered as a desirable source for fabricating porous carbon materials with high specific surface areas of 2573 and 3524 m²/g, respectively [57,58].

The thermal decomposition of lignin is slower over a broader temperature range (200-500°C) than that of cellulose and hemicellulose. Cellulose decomposes between 200-400°C, whereas hemicellulose decomposes in the 200-320°C range. Regarding to higher oxygen to carbon content of cellulose and its high polymeric degree compared to lignin, it tends to be decomposed as H_2O, CO_2, and CO at lower temperature. Interestingly, the total carbon content does not linearly correlate with the amount of cellulose in plants [21,23,59]. The treatment temperature
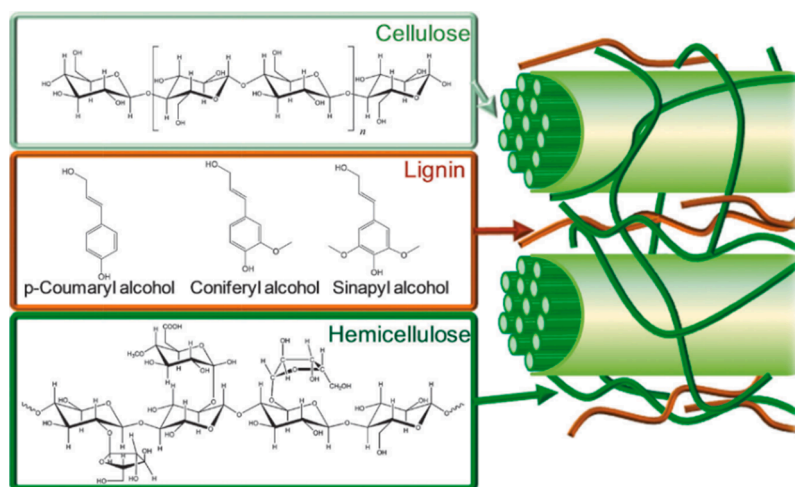

Fig. 1. Structure of lignocellulosic biomass with cellulose: Linear large polymeric molecules, lignin: a complex and highly cross-linked aromatic polymer and hemicellulose: amorphous and highly branched macromolecular structure. Adapted from [48] after the required permission.

higher than 600°C may result in a complete decomposition of lignin and the collapse of the structure. Nevertheless, the thermal treatment of biomass at 600°C could guarantee complete carbonization of the cellulosic components while preserving parts of the aromatic building units [60]. However, the commonly found elements as K, Na, Mg and Ca in biomass by accelerating the degradation of the polymeric structure of cellulose and lignin, result the formation of lower molecular weight compounds. In order to increase char yield, rapid removal of char from the pyrolysis reactor is essential [61].

Pyrolysis of biomass at a low temperature with a low heating rate but a high inert gas flow rate is expected to give a maximum yield of biochar that is highly enriched in carbon [62]. Fast pyrolysis at moderate pyrolysis temperature of 400-600°C increases the yield of bio-oil. However, the biomass composition is the main influence on the char yield of the final carbon. For example, the char yield has been calculated to be 13.2 and 34.4 wt.% for wheat straw and coir, respectively [63]. In addition, walnut shells show fast charring speeds, high char yield of 51.3 wt.%, and an abundant porosity [64].

Besides the conventional pyrolysis processes, molten salts Li_2CO_3, KCl, Na_2CO_3, $ZnCl_2$, K_2CO_3 etc. due to their high heat transfer, high thermal stability and catalyst characteristics in the conversion process, represent a new possibility to produce charred materials. In this process, thermal decomposition of organic components in biomass is carried out in a molten salt bath. The higher heating rate in this process increases the possibility of obtaining less char yield and more tar fraction (pyrolysis oil). This reduction of char yield is mainly attributed to the further production of C-H and C-O bonds and the aromatization of the carbon by the molten salts during pyrolysis [65–67]. Each salt has own catalytic effect that has a significant influence on the yield of products after the conversion process. Different metal ions promote different pyrolysis reactions. For example, potassium and sodium ions increase the char yield, while it is only slightly affected by calcium ions for the pyrolysis of wood. However, other additives such as chlorides, nitrates, and sulfates accelerate levoglucosan generation and, therefore, decrease the amount of the obtained char [68]. In addition, the salt itself has an influence on the specific surface area of the carbon. For example, peanut shells carbonized in a Li_2CO_3/K_2CO_3 mixture have a higher specific surface area than those treated in $LiCO_3/Na_2CO_3/K_2CO_3$, $CaCl_2$, or $CaCl_2/NaCl$ [65]. Shang *et al.* [69] also prepared a porous carbon from peanut shells by carbonization in a $ZnCl_2$ molten salt with a S_{BET} of 1642 m^2/g compared to the conventional oven-driven pyrolysis with S_{BET} = 95.51 m^2/g.

The temperature of the molten salts also affects the char yield. For example, the char yield, bio-oil and -gas products from cellulose pyrolysis in $ZnCl_2$-KCl at 410 °C under N_2 flow were estimated to 38%, 48%, and 14%, respectively [70]. With increasing the temperature to 520°C, the bio-oil and -gas yields increased indicating a de-polymerization of cellulose. The pyrolysis to the oil fraction was the dominant reaction at this higher pyrolysis temperature. He *et al.* [71] reported on lignite brown coal chars obtained with and without molten carbonate salt (Li_2CO_3-Na_2CO_3-K_2CO_3) at 800 °C. The char obtained with the molten salt showed a lower char yield of 43% and higher d_{002} value of 0.371 nm in comparison to 58% and 0.364 nm for the samples treated without a molten salt. The char yield for samples treated in molten salt decreased from 67% at 500 °C to 43% at 800 °C. Lu *et al.* [72] also obtained micro-sheet like porous carbon with specific surface area of 843 m^2/g and d-spacing value of 0.393 nm by treatment of bamboo shell with molten Na_2CO_3-K_2CO_3 at 850 °C. The discussion above suggests that the key issues for having high char yields with optimized porosities are the selection of biomass and the conversion efficiency of biomass into carbon. Fig. 2 illustrates various biomass sources to synthesize char with different compositions. It shows the final properties of the biochar could be engineered by optimizing the composition of the biomass, temperature and heating rate [73,74]. In addition, it is illustrated how the extracted carbon inherits the texture and pore structure of the pristine biomass [75–78].
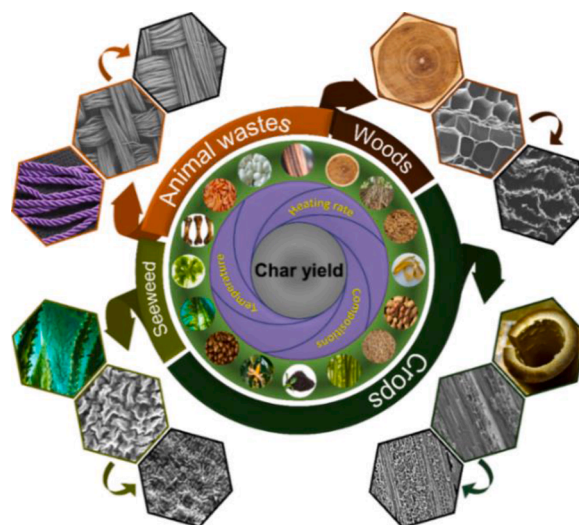
Fig. 2. The diverse range sources of biomass to synthesize biochar. Some parameters such as heating rate and temperature, as well as selecting the biomass with a favorable composition, directly affect the final quality of the biochar and lead to optimized biochar yield.

2.3. Extraction of carbon from biomass

Biomass-derived carbon is obtained by two stages of carbonization and polymerization. In the first stage, at temperatures between 400 and 700°C, volatile matter containing H, N, and O is lost, and some C–O and C–C bonds are cleaved to form small molecules including CO, H_2O, and CO_2. At a temperature close to 700°C, the residual carbon atoms form planar aromatic structures with predominantly H-terminated edges. However, at this temperature the pyrolyzed carbon can still contain other elements such as O and N. At this low temperature range (~ 700°C), the poor stacking of C-C aromatic structures can lead to the formation of micropores. In the second stage, at 600-1200°C, the H atoms are removed and, based on the nature of carbon resource, the wrinkled graphite sheets are stacked either in a near-parallel fashion in regions called "organized carbon' or arranged in a geometry resembling a 'house of cards'. The pyrolyzed carbon displays a microporous structure with a density of about 2.22 g/cm^3 that is lower than that of graphite. The structure contains many interstices that result from the irregular cross-linked graphene sheets that form the micropores [79,80]. The final structure can vary based on the type of starting material and the operational temperature (Fig. 3 (a)).

The pyrolyzed carbon, which cannot be converted into crystalline graphite with infinite parallel layers of graphene (Fig. 3 (b)), even at temperatures >3000°C, is called non-graphitizing carbon or hard carbon (Fig. 3 (c)). However, different biomass resources show different graphitization behavior. For examples biomass waste materials with higher cellulose content such as sugarcane bagasse [81], pineapple leaf fibers [82], mengkuang leaves [83], wastepaper [84] and cotton [85] showed a relatively high degree of crystallinity. Rouzaud described that the graphitization improves in the presence of hydrogen and at a shortage of oxygen in the precursors [86].

Soft carbon can undergo graphitization more easily than hard carbon. The soft carbon usually starts to transform into a liquid phase at a temperature around 400-500°C, and the planar graphene sheets arrange themselves easily in a near-parallel manner (Fig. 3 (d)). The tendency of soft carbons to graphitization depends on the nature of the carbon precursor. Carbon derived from highly condensed aromatic hydrocarbon precursors is particularly amenable to graphitization [36,37,87,88].

The difficulty of graphitizing hard carbons even at high temperatures could be exacerbated for densely 3D crosslinked polymers and source materials enriched with lignin and hemicellulose [89]. Although lignin
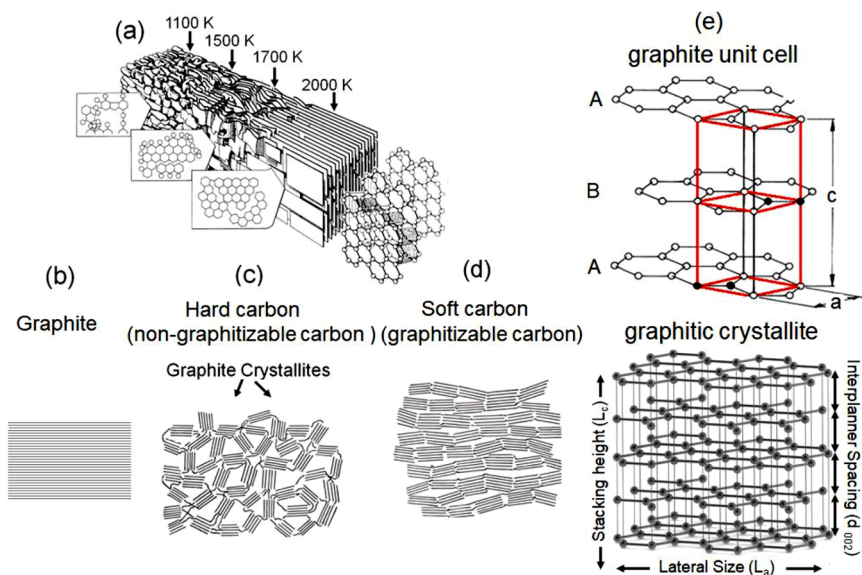
Fig. 3. a) Graphitization of carbon as a function of temperature by growing micrographitic crystallites of highly disordered aromatic carbon at 1100 K to graphitic structure at 2000 K [94], b) Structure of graphite, c) structure of non-graphitizing carbon, d) Structure of graphitizing carbon [95], and e) Illustration of graphite unit cell (with a = 2.46 Å and c =6.71 Å) and graphitic crystallite (L_a, crystallite size; L_c, thickness) [96],[97]. Adopted from mentioned references after the required permission.
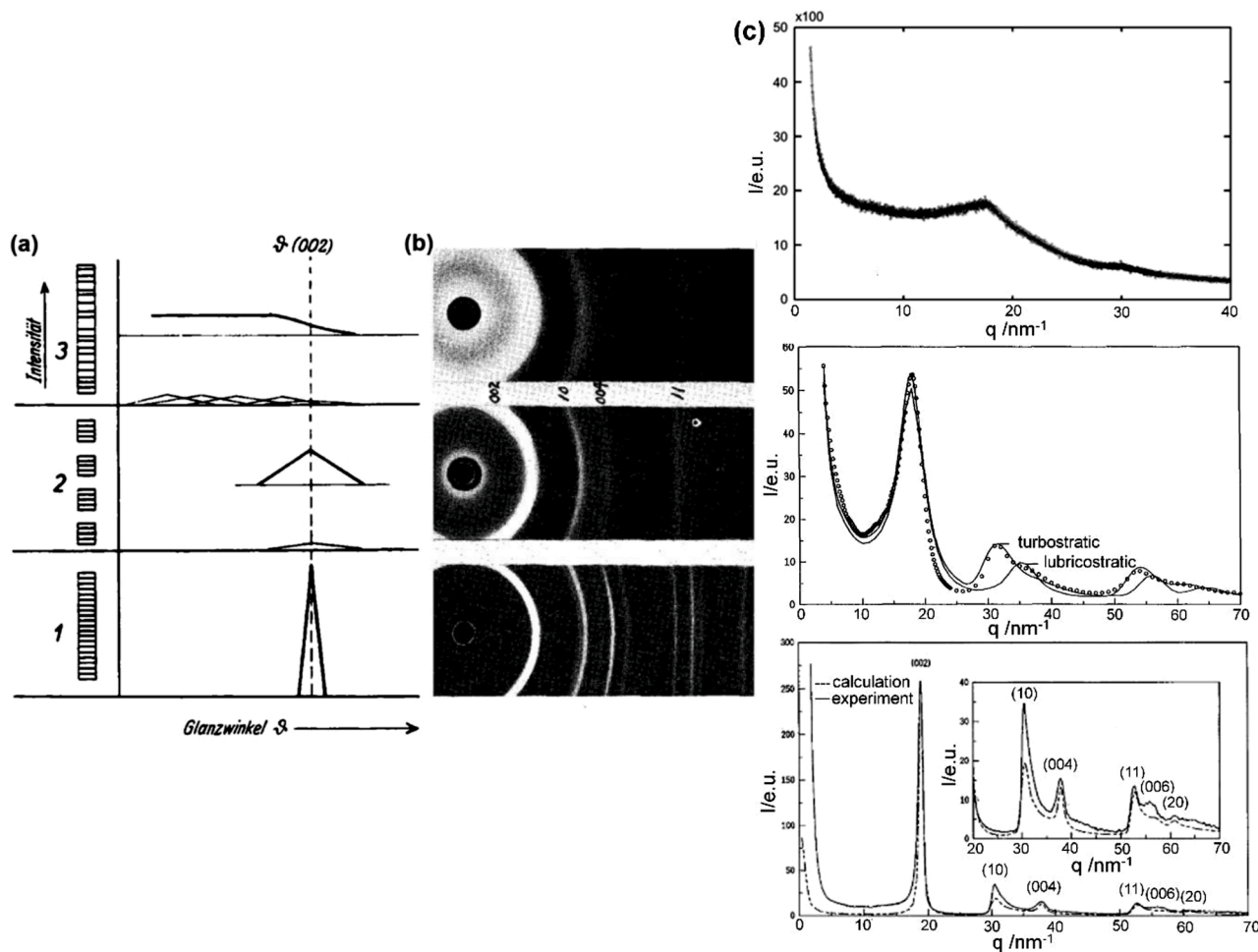
Fig. 4. a) Idealized carbon structures (left column) and their expected signals for the 002 reflection (right column), 1 for a crystalline, graphitic carbon, 2 for a nanocrystalline, turbostratic carbon and 3 for an amorphous carbon (Intensität, german = Intensity, Glanzwinkel, german = Bragg angle). Adapted from [98] with permission of DeGruyter. b) X-ray photographs of a crystalline carbon (bottom), nanocrystalline/turbostratic carbon (middle) and of an amorphous carbon (top). Adapted from [99] with permission of IOP Publishing. c) X-ray patterns of a crystalline, graphitic (bottom), a nanocrystalline/turbostratic (middle) carbon, adapted from [100] and of the amorphous carbon SuperPLi from Timcal, recorded as a transmission powder sample on a STOE Stadi P diffractometer, λ = 1.78896 Å, by one of the authors (top).

possesses low oxygen content, its short-range-ordered structure postpones the graphitization. Biomass which contains glucose has lower onset temperature for graphitization. Indeed, glucose melts to form a liquid intermediate and accelerates the graphitization process [35]. However, Gomez *et al.* [90] have shown that the impregnation of medium-density fiberboard (MDF) wood in a 1 M $FeCl_3$ solution could promote the graphitization of disordered carbon at lower temperature of 700°C. Here, the degree of graphitization α of a hydrocarbon reached 0.8 at 2000°C, as determined from the I_G-to-I_D intensity area ratio according to $\alpha = I_G/(I_G + I_{D1})$. For the iron-catalyzed pyrolysis of the wood, 0.7 was calculated which was only slightly lower. However, in an uncatalyzed reaction the degree of graphitization of the wood hard carbon was determined to 0.3 only, even at temperatures up to 2800°C. Graphite from hard carbons is produced in a Fe-catalyzed reaction, by continuous dissolution of disordered carbon into iron or iron carbide particles, which are obtained in situ by the carbothermal reduction of Fe^{3+} ions to Fe^0. By decreasing the temperature, graphite precipitates from the Fe-Fe_xC-C solution. The removal of the iron or the iron carbide particles via acid etching can result in a microporous structure [91]. Xu *et al.* [92] showed presence of trace metals such as iron in bean shells. This Fe content improved the degree of graphitization. Derbyshire *et al.* [93] also reported the formation of laminar graphite after cooling of a solution of non-ordered carbon in cobalt and nickel foils heated to ~1000°C before. Ni and Co carbides are instable above 500°C which led to traces of these compounds. With an Fe foil, only iron carbide was formed and no graphite was observed.

2.4. Characteristics of biomass derived carbon

To investigate the structure of carbons in general, several physical methods have proven to be of value. One of the most used techniques is X-ray diffraction (Fig. 4). From the models for the different structures of carbons, graphitic (crystalline, Fig. 4 (a.1)), turbostratic (nanocrystalline, Fig. 4 (a.2)) and amorphous (Fig. 4 (a.3)), the influence of the structure on the signal width and the intensity of the related X-ray patterns are exemplary shown in Fig. 4 (b) and 4 (c) [98]. It has been shown de-graphitized carbon black in addition to orientational disorder around normal layer (turbostratic stacks) features translational disorder along the layer plane (lubricostratic stacks). Measurements of the real, corresponding carbons are compared to the models by the circular X-ray patterns of a Debye-Scherrer film camera (Fig. 4 (b)) [99] and X-ray patterns recorded with the nowadays used modern X-ray diffractometers (Fig. 4 (c)) [100].

Based on the conventional rhombic unit cell as determined for graphite [101], the structure of turbostratic carbon is classified in terms of basal-plane correlation length L_a and *c*-axis correlation length L_c, which are estimated from the positions of the 002 and 100 Bragg reflections in diffraction pattern, respectively [25–27] (see Fig. 3 (e)). The d_{002} spacing is calculated by the Bragg's equation, whereas the thickness (L_c) and average width of the graphitic domains (L_a) are calculated from the Scherrer equation. The 100 reflection corresponds to the honeycomb layers in the plane of the hexagonal lattice that are formed by sp^2-hybridization, whereas the 002 reflection is responsible for the domains of coherent parallel-stacked graphene sheets. The 002 reflection is clearly observed in soft carbon, which points to the stacking of carbon layers in a near-parallel orientation. By contrast, hard carbon exhibits a less intense and weakly shaped 002 reflection, which indicates the presence of a substantial number of single graphene sheets. The intensity of the 002 reflection increases with the carbonization temperature and moves to the higher angle. Because the hexagonal layers in turbostratic carbon rotate randomly with respect to each other about the *c*-axis, the interlayer spacing (d_{002}), increases from 3.34 to 3.44 Å as compared to 3.35 Å in graphite. The L_c and L_a values were observed to be between 4 nm and 10 nm for hard carbon and 100 nm for soft carbon. However, both types of carbon show approximately the same values of L_c and L_a (1 nm) at temperatures below 1000°C [25–27], [36,37,102]. Increasing the

carbonization temperature will cause more horizontal growth of pseudographitic instead of vertical growth, therefore at higher temperature higher L_a value than L_c value is expected [103].

Lotfabad *et al.* [104] observed the bimodal distribution in *d* spacing for 002 reflection for carbon extracted from banana peels. Fig. 5 (a) shows the X-ray diffraction pattern of carbon obtained via carbonization of banana peel pseudo-graphite (BPPG) at temperatures between 800 and 1400°C. The carbon contains two graphene interlayers with spacing of 3.86 and 3.354 Å, respectively, as well as 2.12- and 5.49-nm-thick pseudo-graphitic domains. The bimodal distribution of the interlayer spacing, d_{002}, indicated that the temperature was high enough to form equilibrium graphite ($c/2 = 3.354$ Å). This graphitization was due to small molecules of free sugars presented in banana peels which transformed to liquid phase at 1400°C and allowed the graphene sheets to partially align themselves. Moreover, pectin in the banana peels underwent some aromatic ordering, which is similar to the behavior of cross-linked lignin. However, no equilibrium graphite was observed to form at a lower carbonization temperature of 800°C, and an interlayer spacing of 3.97 Å with pseudo-graphitic domains of 1.53 nm was reported [104]. High-resolution transmission electron microscopy (HRTEM) (Fig. 5 (b-d)), revealed more ordered carbon with increasing carbonization temperature. In both samples, which were heat-treated at 800 and 1100°C, well-defined mesopores were observed throughout the structure [104].

Raman spectroscopy is another technique to show the degrees of graphitic ordering (Fig. 6). Carbon with various proportions of sp^2- and sp^3-hybridization shows different structure and physical properties. The degree of disorder and domain size of sp^2 are proportionate to the I_D/I_G intensity ratio obtained from Raman spectra. The Tuinstra-Koenig [105] law (Eq. (1)) relates the I_D/I_G ratio to the crystallite size of graphitic samples, which can be used as a good approximation for the ratio. For the large crystallite size with few defects the G-peak is more intense than D-peak while by increasing the defects the I_D/I_G ratio increases. This increasing trend stops when the amount of defects exceed a certain value and the D-peak intensity starts to decrease [106].

More precise determination of the crystallite size (L_a) in the graphitic parts of the carbons can be calculated by an adapted Tuinstra-Koenig law as described by Mallet-Ladeira *et al.* [107].

$$\frac{I_D}{I_G} \propto \frac{1}{L_a[nm]} \qquad (1)$$

For the highly amorphous carbon, the corresponding Raman spectrum (Fig. 6 (a) upper) shows a plateau between 1300 $cm^{-1} \leq 1/\lambda \leq$ 1700 cm^{-1} representing the sum of vibrations mainly related to a disordered graphite lattice [36]. Turbostratic carbons are less disordered with curved graphene layers and the Raman signals are reduced to a relatively sharp G-band at about 1600 cm^{-1} and the broad D-band at about 1340 cm^{-1} [36]. The G-band for the crystalline carbon at around 1580 cm^{-1} (belonging to active E_{2g} mode) corresponds to in-plane vibration of sp^2-bonded carbon atoms in the hexagonal lattice. The D band at around 1350 cm^{-1} (belonging to A_{1g} symmetry) mainly reflects the small amounts of disordered carbon, edges, and other structural defects (e.g. sp^3-bonded carbon, vacancies, and topological defects) [108].

Doping of carbon by other elements leads to an energy shift of the G band. For example, a shift of the G-band to a higher energy (blue shift) was observed in nitrogen-doped carbon because of the increased carrier concentration from doping [109]. As the pyrolysis temperature increases, the full-width half-maximum of G-band and I_D/I_G decreases, indicating more ordered structures [110,111].

X-ray photoelectron spectroscopy (XPS) has suitably been developed to determine hybridization states of carbon and carbon atoms bound to non-carbon atoms to form functional groups [112,113]. As seen in Fig. 7, the de-convoluted C 1s signal of the XP spectrum of a mesoporous carbon can show many participating C-C and C-O species at different binding energies. To give an impression on the respective functional groups shown in the XP spectrum, such groups are marked with their
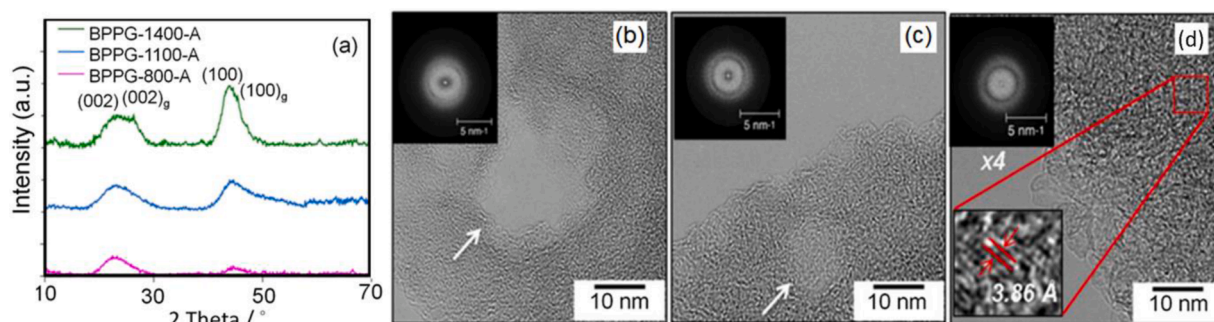
Fig. 5. a) XRD pattern of BPPG heat-treated at 800, 1100, and 1400°C with post air-activation, b-d) HRTEM micrographs of samples BPPG-800-A, BPPG-1100-A, and BPPG-1400-A, respectively [104]. Adapted from mentioned reference with permission of the American Chemical Society.
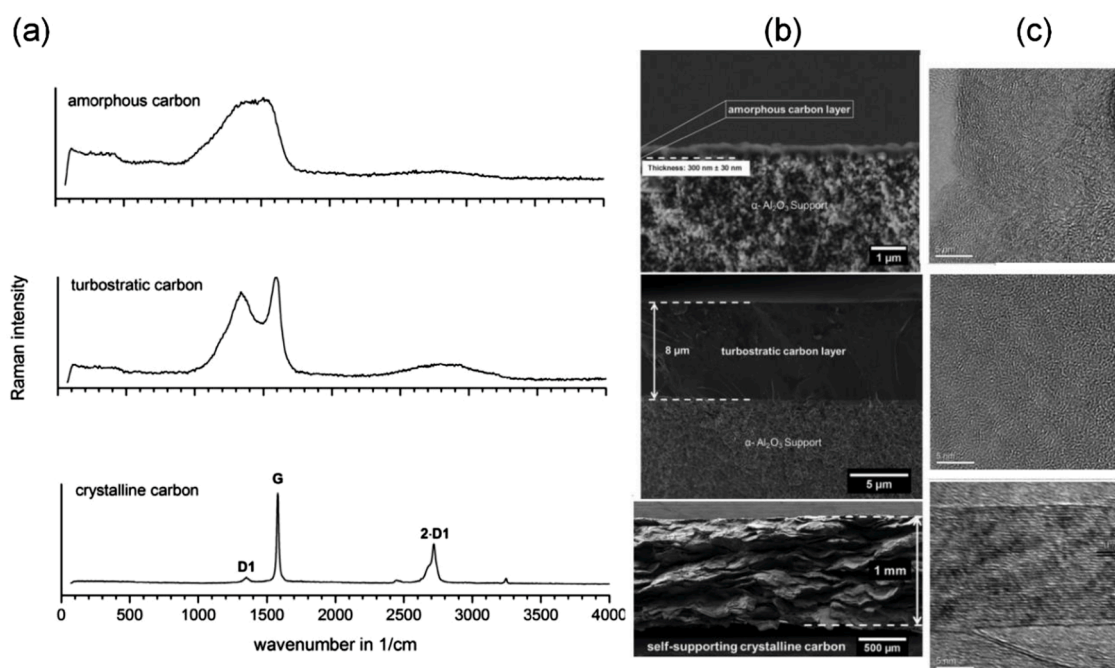
Fig. 6. a) Raman spectra of crystalline, graphitic carbon (bottom), nanocrystalline turbostratic (middle) made by pyrolysis of polymer precursor film and amorphous carbons made by physical vapor deposition (PVD (top)). The corresponding scanning electron microscopy pictures in b) Show the individual sample architecture and c) The transmission electron microscopy images support the crystallinity complimentary to the Raman spectra. Adapted from ref. [36] with permission of Elsevier B.V.

numbers in an exemplified carbon network. For a hard carbon, similar spectra can be measured with deviations in the binding energies according to the binding energy referencing and general composition of the carbon, e.g. the influence of other elements like N, S or halogens. The sp^2 carbon double bonds C=C of a typical hard carbon are located at a binding energy of 284.6 eV [114]. The sp^3 carbon bonds C-C, the C-O and the C=O bonds, as well as the $\pi-\pi^*$ graphitic shake-up satellite cover binding energies of 285.6, 286.7, 288.3, and 290.4 eV, respectively [114–116]. A higher peak-intensity ratio of sp^2/sp^3 points to lower levels of structural defects in the hard carbon. Note that variations of the $\pi-\pi^*$ contribution, typically related to the delocalization of p electrons e.g. in sp^2-hybridized carbon system, can hint to different degree of (local) disorder. Higher disorder might be responsible for a localization of the π charge and the disappearance of the $\pi-\pi^*$ contribution [117,118].

However, the participation of the $\pi-\pi^*$ contribution can alter e.g. by a degraded overlap of p orbitals compared to graphite, a shorter life time of the excited state, changes in the layer-to-layer interactions and/or topographic effects [117–120].

3. Tailored carbon anodes derived from biomass

Pyrolyzed biomass-derived carbon is non-graphitizing, hard carbon with varying textures, morphologies, and degrees of crystallinity. It provides short diffusion paths for ionic and electron transport and can therefore be an attractive material for anodes in metal-ion batteries. The solid structure of such carbon with short diffusion pathways is the basis for the excellent cyclability in batteries without substantial exfoliation during the insertion and extraction of ions. In addition, the tailorable porous architecture with hierarchical pore structure, if desired, can support high gravimetric specific energy capacity in the batteries. For example, the formation of Li layers on the graphene sheet, the storage of Li in the micropores, and the formation of LiC_2, C–H–Li, or N–Li bonds, makes the turbostratic carbon structure more likely to have extra charge than fully-intercalated graphite with LiC_6 stoichiometry [121,122].

To date, many studies have sought to improve the performance of pyrolyzed biomass-derived chars by engineering the char porosities (e.g. sacrificial silica template [123], chemical and physical activation [124, 125]), chemical substitutional doping (e.g. boron [126], nitrogen [127], and phosphorous [128]), and the fabrication of hybrid nanocomposites
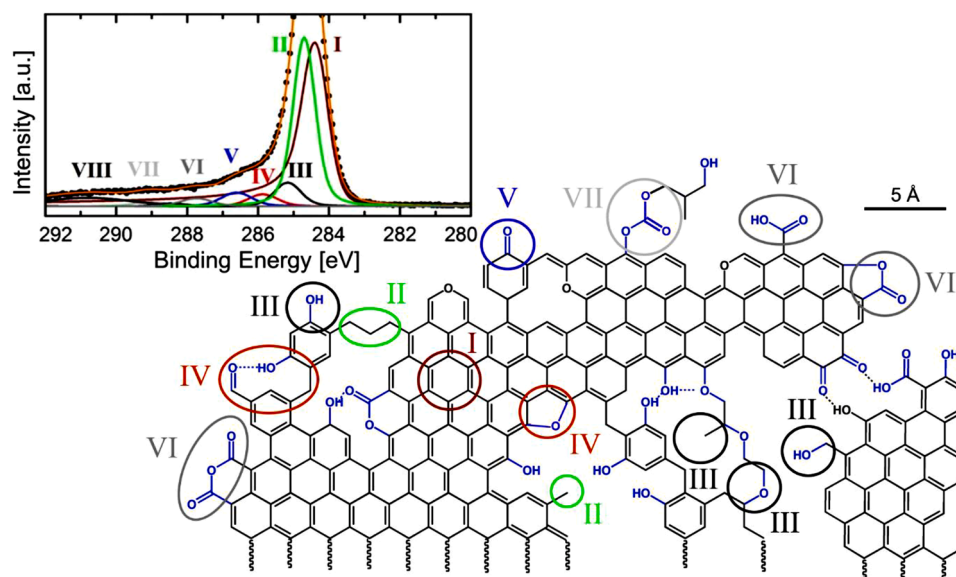
Fig. 7. XP high resolution spectrum of the C 1s signal of mesoporous carbon (upper left). The spectrum fits represent eight contributions which can be related to several chemical functionalities in an exemplified carbon lattice (lower right). Adapted from ref. [112] with permission of Elsevier B.V.

consisting of a carbonaceous matrix and a transition metal oxide [129–131]. However, the performance of electrochemical energy-storage devices using existing carbonaceous material is limited in terms of charge capacity, rate capability, and electronic conductivity. Addressing these issues require the following: 1) electrodes composed of hard carbon with an optimized specific surface area to facilitate charge capacity [132–134]; 2) nanostructured carbon to shorten the diffusion pathways at the electrode/electrolyte interface [135]; 3) hetero-atom-doped carbon materials to alter electronic properties [136,137]; and 4) hierarchically porous carbon to accelerate ion transport with improved rate capability [138,139]. Indeed, the hollow macroporous cores, which are connected and open to the outer mesoporous shell can serve as an electrolyte reservoir and facilitate mass transport [140]. We discuss each of these in detail in the following sections.

3.1. Morphological modification

In most cases the extracted carbon inherits the textural architecture and porous structure of the pristine biomass. However, the structure and morphology of carbon could be modified to yield nano particles, nano-tubes, nanofibers, nanosheets, and porous carbons with desired shape by using some chemical techniques [141–144]. In the following sections, we will explain the most common modification techniques which modify the morphology of the extracted carbon from biomass and affect the electrochemical properties of restructured carbon.

3.1.1. Carbon quantum dots (0 D)

During the past decades, zero-dimensional carbon dots (CDs) of less than 10 nm and with sp^2/sp^3 hybridization as a special class of carbon-based nanostructures with tunable band gap have shown exceptional chemical and physical properties that may facilitate a wide range of potential applications in optics, energy storage, medicine and others [40,145,146]. There are two routes for successful CD syntheses: I) the bottom-up method by converting suitable organic precursors to CDs via chemical, thermal decomposition, solvothermal/hydrothermal treatment or microwave synthesis, and II) the top-down approach by breaking down a large carbon structure e.g. found in graphite, soot, CNTs or activated carbons into CDs via an arc discharge method, laser ablation, electrochemical synthesis and etc. However, these paths need either costly and toxic organic precursors or a complex equipment and post-treatment processes to synthesize CDs. Recently, natural

carbon-based materials such as silkworm chrysalides [147], rice husk [148], coconut husk [149], garlic [150], Jinhua bergamot [151], orange juice [152], and bagasse [153] can save expenses for the organic starting and can become of interest for the syntheses of CQDs and GQDs. Although, not reaching a precise particle size is the main drawback of biomass as the growth rate of the particles can only be controlled by heating rate, reaction time and temperature to some extent. CDs with a high concentration of oxygen-containing surface groups, high defect density or a large specific surface area show superior performances in supercapacitors. CDs derived from biomass that possess a large specific surface area and a high content of nitrogen as dopant are favored as electrodes in supercapacitors due to their higher storage performance. Additionally, it is easier to synthesize high N-doped CDs from biomass compared to a bottom-up approach [154–157]. While CDs show inter-esting results in supercapacitors, the reports about their utilization in batteries are still scarce. CDs as conductive additives in composite anode materials can significantly increase the electrochemical performance of the anodes. Thus, GQDs coated on VO_2 enable a specific capacity ->420 mAh/g and capacity retention of 94% after 1500 cycles at 18 A/g vs. Li^+/Li [158], CDs coated on a Mn_3O_4 composite reach a capacity of 934 mAh/g after 50 cycles at a 0.1 A/g vs. Li^+/Li [159], and a Sb@CQDs composite with specific capacity of 510 mAh/g after 120 cycles at 0.5 A/g vs. Na^+/Na [160]. Hierarchical TiO_{2-x} imbedded in GQDs give a specific capacity of 160 mAh/g at 10 C after 500 cycles vs. Li^+/Li [161]. All these examples support the positive effect of CDs in electro-chemical energy storage devices. In the previously described cases the electronic conductivity of the samples and the ion transfer rate between the electrolyte and the active material were increased by the combina-tion of highly conductive CDs and their large specific surface area. The large potential of CDs in energy storage applications utilizing materials from renewable sources have not been reflected by literature yet. There are only few reports on the application of CDs derived from biomass in electrochemical processes. Yi *et al.* [162] reported on the synthesis of GQD/Fe_3O_4 nanocomposite via a one-step thermochemical reaction. The thickness of synthesized GQD was measured about 10 nm accom-panied with some multi- layer graphene with thickness of 10 to 150 nm. GQD/Fe_3O_4 delivered high specific capacity of 3829 mAh/g at 0.05 A/g vs. Li^+/Li, which is four times higher compared to pure Fe_3O_4 having a theoretical specific capacity of 924 mAh/g. Alkaline lignin, the main component of the effluents of paper pulping, with a large number of hydrophilic groups, provided remarkably reactive sites for the growth

and anchoring of iron nanoparticles, to be found back in the interlayer of the graphene-like carbon sheets. Abundant reactive sites for Li coordination and an optimized electronic structure for a fast charge transfer are the main reasons for the superior electrochemical performance. Peng *et al.* [163] produced CDs from glucose with 5 nm in diameter by a simple aqueous solution route. The carbohydrates were dehydrated using concentrated sulfuric acid followed by a decomposition into carbogenic (called carbogenic due to their oxygen content) nanoparticles by nitric acid. The glucose-derived carbon dots using chemical oxidation method provide a superior conductivity and a rapid ion transport. Therefore, a good cycling performance and a high rate capability in LIBs and SIBs were reached, namely specific capacities of 864 mAh/g at 0.5 C and 153 mAh/g at 20 C after 500 cycles vs. Li^+/Li and 324 mAh/g at 0.5 C and 55.7 mAh/g at 20 C after 500 cycles vs. Na^+/Na [164].

3.1.2. Nanotubes and nanowires (1D)

CNTs are members of the fullerene structural family and related to spherical fullerenes. Bending and rolling a graphene layer theoretically forms seamless single-walled cylindrical structure composed of sp^2-hybridized atoms that can be extended to a multi-walled one if layered graphene is considered. In this type of structure, the graphite monolayer planes are often parallel to the tube axis [165,166].

Arc-discharge, laser ablation, and chemical-vapor deposition are typically used for the synthesis of CNTs [167]. Alternatively, CNTs and nanofibers can also be obtained sustainably from biomass. For example, Xie *et al.* [168] claimed that CNT can be extracted from bamboo or wood by pre-carbonizing the raw materials in air at 240°C and cyclically heating the obtained materials to 400°C in the presence of oxygen at pressures below atmospheric (1 KPa). This cyclic oxidation procedure leads to the decomposition of the carbon from cellulose microfibrils because it has a lower resistance to oxidation at elevated temperatures than lignin. Consequently, a channel forms within the residual lignin matrix. Since the volatile carbon-containing vapor was trapped inside the channel covered by carbonized lignin, it is concentrated on the internal surface of this "nano-channel" and finally forms the CNT. The pre-carbonization promotes the dehydration of cellulose to reach higher carbon contents and to stabilize the lignin to shift its decomposition to higher temperatures. To test this mode of formation of CNTs from

biomass sources, these authors treated pure lignin and pure cellulose with the same heating-oxidation protocol. However, they were not successful in producing CNTs. The authors attributed the failure to the molecular and spatial arrangement of cell walls [169].

Gao *et al.* [170] reported the synthesis of CNTs from yeast-wheat flour dough (Fig. 8 (a)). The fermented dough was cut into small pieces and dried at 50°C for 6 h, and the pieces were then heated to 750°C for 2 h in argon gas. During the heating process, highly dense CNTs were formed simultaneously on both the inner and outer surfaces of the porous activated wheat dough (AWD). The growth of yeast cells in the dough caused the adhesion of gluten proteins and the dough captured CO_2 released during the decomposition of carbohydrates (starch and sugars) via the metastatic reactions of yeast. This preparation led to an expansion in size and an interconnected porous structure. SEM and TEM analysis (Fig. 8 (b-d)) revealed highly dense CNTs with 3-20 μm in length and crystal-lattice spacing of ~0.35 nm on the activated dough surface and pore walls of AWD.

CNTs are considered to be a good anode material for Li/Na-ion batteries in view of their unique structure; high electrical conductivity (10^6 S/m) owing to π-orbital overlap; low density; high thermal conductivity to dissipate heat from electrodes; and high rigidity (Young's modulus of the order of 1 TPa) [171–173]. Specific features of CNTs that help to increase Li intercalation include the presence of delocalized electrons due to bended planar orbitals of sp^2-hybridized carbon and its greater electronegativity as compared with graphitic sheets [174]. However, CNT have an irreversible Li ion capacity, such that the rate of intercalation surpasses the removal rate and also lower binding energy with Li compared to cohesive energy of bulk Li: these are key factors that limits their applicability. In addition, unlike graphite, CNT anodes show broad voltage changes during the discharge process, which inhibits the use of CNTs in applications that require a stable power source. Various reversible capacities have been reported for CNT anodes and, in some cases, they exhibit an intercalation of up to LiC_3, as compared with the LiC_6 of graphite. This behavior shows that Li-storage in CNTs proceeds via mechanisms that differ from those in graphite [175–180].

The low capacity of CNT anodes is related to large energy barriers if Li^+ ions need to diffuse through the sidewalls. Opening the closed ends of the CNTs and introducing lateral topological defects on CNTs enable a
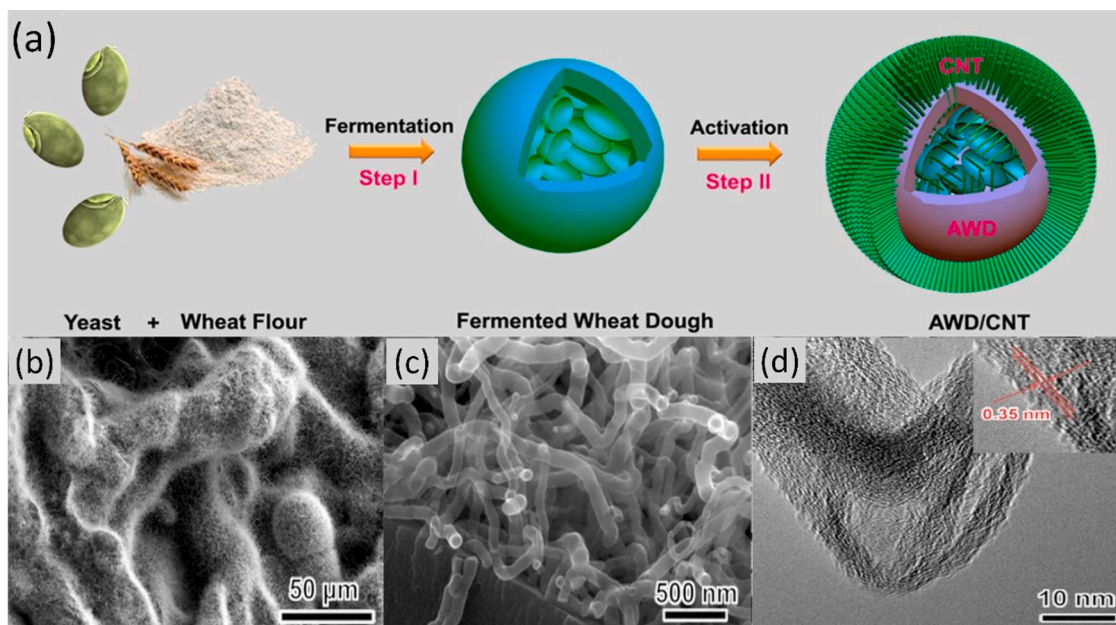
Fig. 8. (a) Schematic illustration of the formation and morphology of yeast-derived CNTs. b) SEM image of the filamentous CNTs on the AWD surface. c) High-magnification SEM image of the filamentous CNTs, (d) HRTEM image of CNT; inset shows lattice fringes of the tube wall. Adopted from [170] after the required permission.

regular intercalation of Li^+ ions [181]. After the removal of a carbon atom introduces a hole inside the CNT wall with open ends, Li^+ ions can access the internal walls of CNTs more easily and absorb on them more readily, and therefore accumulate successfully in the interior as well as on the exterior of CNTs. The energy barrier for the diffusion of Li^+ ions into the CNT can be decreased by simply cutting the ends. Long CNTs, with high aspect ratios ranging from several to tens of micrometers and diameters of up to a few nanometers, cause an effective reduction in the diffusion of Li^+ ions by forcing the ions to pass through a long, one-dimensional pathway [171]. These results underline the importance of optimizing the CNT morphology to improve their Li^+ ion storage capacity [171]. Two effective ways of modifying the length of CNTs are chemical etching and ball milling, which increase the reversible capacities for Li intercalation to 681 mAh/g ($Li_{1.8}C_6$) [182] and 641 mAh/g ($Li_{1.7}C_6$) [183], respectively.

The defects and disordered structures of CNTs derived from biomass could also facilitate the penetration of ions into the cavities of CNTs. For example, carbonized microtubular carbon extracted from cotton exhibited a reversible specific capacity of 315 mAh/g vs. Na^+/Na. It also delivered specific capacities of 275 and 180 mAh/g at current rates of 0.5 C and 1 C, respectively. The sloping potential profile was attributed to Na^+ ion adsorption on defects, edges, and the surface of the nano-graphitic domains, whereas the plateau region was related to nanovoid filling [184].

In contrast with CNTs, the graphite layers in nanofibers (graphitic filamentous structures) are arranged either perpendicular to the fiber axis or at an angle to it [171,185]. Carbon nano-fibers (CNFs) with more disordered, less oriented structure and more defects could increase the reversible capacities. However, the presence of too many defect sites could break the conjugated π bonds and make CNFs electrical insulators [186,187].

CNFs performance can be further improved by creation of a 3D porous structure out of them. It will be explained in section 3.1.4 how interconnected pores networks can improve the electrochemical performance of the battery. Xing *et al.* [188] showed that by synthesis of phenolic resin-based mesoporous nanofibers using hard template the delivered Li-storage capacity reached up to 1132 mAh/g at 0.1 A/g after 100 cycles. A high rate capability with a specific capacity of 880 mAh/g at a current density of 5 A/g was demonstrated as well [189].

Tao *et al.* [142] showed that although the capacity of CNFs is less than that of graphene, it is comparable with that of electrospun carbon nanofibers from walnut shells. The carbon extracted from walnut shells exhibits long nanofibers with diameters of 280 nm and smooth surfaces with abundant pore structure and good flexibility. To prepare the nanofibrous carbons, the liquefied products of the mixed walnut shell powder, phenol, and sulfuric acid, together with formaldehyde and sodium hydroxide, were first mixed and diluted by distilled water and 12 wt.% polyvinyl alcohol. Polyvinyl alcohol adjusted the viscosity, and a nanofiber composite was produced by electrospinning. Finally, the dried electrospun material was carbonized at 1500°C for 1 h in an argon flow. The electrochemical performance of the nanofibers reached a specific capacity of 270 mAh/g at 0.03 A/g, and displayed a good cycling performance and high reversibility of above 280 mAh/g after 200 cycles at 0.1 A/g vs. Li^+/Li. These results demonstrate that the 1D nano-structured carbon, mutually interconnected in all directions, can reduce the path length and facilitate faster electron and metal-ion migration. Further, the presence of graphite-like crystallite layers and abundant pore volume led to an increased specific capacity [142].

Luo *et al.* [190] proposed a novel hard carbon nanofiber derived from cellulose nanofibers. Cellulose nanofibers were prepared from bleached pulp and carbonized at 1000°C under argon for 2 h. The resulting nanofibers were 50-100 nm wide, reached lengths of up to several microns, and had specific surface areas of 377 m^2/g. They were stacked on top of each other forming an interconnected network in all directions, which reduced the path length for faster electron and Na-ion migration. The nanofibers showed a reversible specific capacity of above 250 mAh/g at a current density of 0.04 A/g vs. Na^+/Na; good rate capability of 85 mAh/g at 2 A/g; and a cycling stability of 176 mAh/g over 600 cycles at a current density of 0.2 A/g.

Jayaraman *et al.* [191] produced 1D graphitic fibers with a hollow-structured morphology via a modified catalytic chemical vapor deposition process using vegetable cooking oil as a carbon source. The synthesized carbon was cycled at a voltage range of 0.005-1.5 V vs. Li^+/Li and delivered capacities of ~512 and ~336 mAh/g at a current density of 0.037 A/g for first discharge and charge, respectively, and a Coulombic efficiency of 84% after 80 cycles. The reason of this improvement is due to the 1D ordering that provides the features like shorter Li^+ ion diffusion pathways, high surface-to-volume ratio, tuning of the crystallographic orientation for facile charge transport.

3.1.3. Nanosheets and flakes (2D)

Carbon nanowalls (CNWs), carbon nanosheets, or nanoflakes are two-dimensional self-supported networks of vertically aligned graphitic walls with high surface-to-volume ratios and low thicknesses ranging from a few nanometers to several tens of nanometers. The edges of CNWs are composed of planar graphene sheet stacks that stand almost vertically on the substrate [192,193]. Regarding the adsorption of Li^+ ions on two sides of the graphene sheets, the theoretical specific capacity can increase to 744 mAh/g with the formation of an expected stoichiometry of Li_2C_6 . However, according to some reports, Li ions seem to not be adsorbed onto pristine monolayer graphene: instead, Li^+ ions were located mainly within the CNWs interlayers and on the edges, or in association with defects which are created during fabrication [194–197]. Positive lithiation energy of graphene compared to a negative value for graphite forces the absorbed Li atoms on graphene to aggregate into clusters and eventually macroscopic dendrites instead of a formation of a stable Li−graphene phase [179,180].

Two-dimensional carbon nanostructures, especially 2D porous carbon materials, are used in electrochemical energy storage. Large surface-to-volume ratios, sharp edges of the CNWs, continuous conducting pathways for electrons, and facile strain relaxation during battery operation results in significant improvements in power and energy density [198,199].

Various types of biomass materials have been used in previous work to produce nano sheets. Here, we give some examples to provide an overview of the extraction of nanosheets from waste biomass materials.

Wheat straw has been used to extract layered graphene (nanosheets) [200]. Wheat straw features layers of hydrophobic wax in its outermost part and also a loose layer of lignin and hemicellulose which protects the crystalline cellulose inside [201,202] (Fig. 9 (a)). Since the cross-linked polymers, including hemicellulose and lignin, do not undergo the complete removal during chemical activation, the crystalline cellulose was not separated efficiently and leads to the formation of carbon with honeycomb morphology [203]. However, using hydrothermal processes, e.g. with highly concentrated aqueous KOH solution, removed the wax and dissolved hemicellulose and lignin whereas the crystalline cellulose was partially degraded but not dissolved. The loose connections between the cellulose microfibrils were lost completely after carbonization at 800°C with the residual KOH, and finally the separated layers of graphene were obtained. Additional carbonization and chemical treatment with KOH (Fig. 9 (b-e)) led to the formation of a highly continuous, 1.2–3.5-nm-thick graphene sheet-like structure with abundant micro- and mesoporosity [200]. Note that a pristine graphene sheet is atomically flat with a well-known thickness of 0.34 nm [204].

In another study, 2D porous carbon nanosheets derived from silk were synthesized in the presence of metal salts such as $FeCl_3$ and $ZnCl_2$ [205]. Such salts not only facilitate the dissolution of natural silk but also act as effective activation and graphitization agents. Immersion of silk fibroin in $FeCl_3$ and $ZnCl_2$ solutions which induced a self-assembly of the hydrophobic and hydrophilic blocks of silk fibroin [206]. Lamellar-like layered structures were converted into carbonaceous materials at 900°C for 1 h in N_2 atmosphere. The synergistic effects of
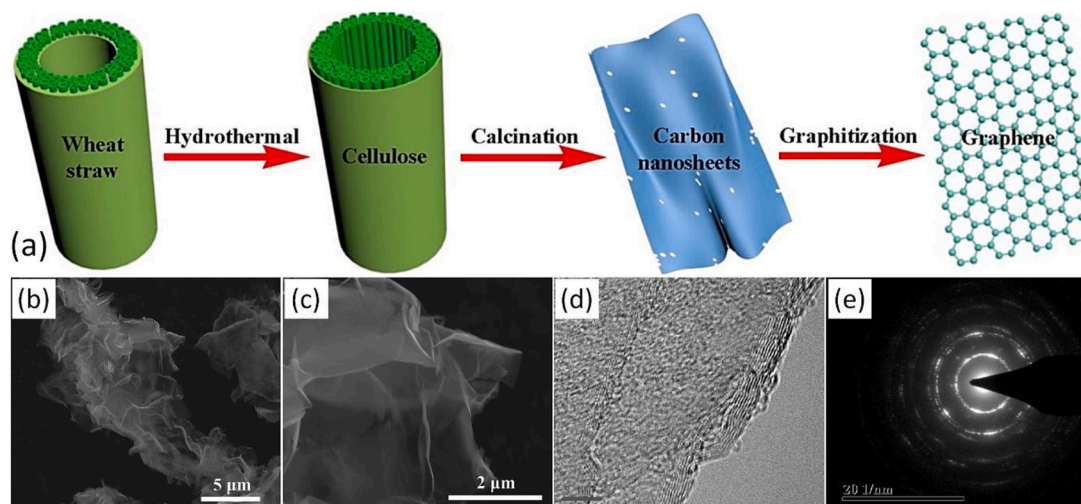
Fig. 9. a) Schematic diagram displaying the overall evolution of wheat straw into few-layer graphene, b, c) SEM, d) TEM, and e) SAED pattern of few-layer graphene. Adapted from [200] after the required permission.

high specific surface area (S_{BET}=2494 m^2/g), high volume of hierarchical pores (2.28 cm^3/g), and N-doping (4.7 wt.%) resulted in an ultrahigh reversible Li-storage capacity of 1865 mAh/g vs. Li$^+$/Li.

Another material used to produce sheets is waste-starch-based packing peanuts [207]. At a rate of 1 C, carbonized packing peanut showed a specific capacity of 250 mAh/g vs. Li$^+$/Li. This improved rate performance is related to the irregular 2D and porous microstructure of 3D interconnected carbon microsheets, which avoids agglomeration during electrode fabrication, facilitates electrode/electrolyte contact and reduces the interfacial charge transfer resistance. Moreover, the voids that form between microsheets buffer the slight volume changes during lithiation-delithiation process.

Using wheat stalk as a precursor, Zhou *et al.* [208] obtained mesoporous ultrathin 2D nanosheet carbon with high degree of graphitization (~90%) via hydrothermal synthesis followed by the mandatory graphitization process. The mesopores and the graphene layers thereby obtained were seen to provide extra active sites to store Li$^+$ ions and migration paths to facilitate a proper electron transfer. The intercalation sites for Li$^+$ ions are the main contributor to the rate performance and cycling stability. Flat voltage profiles with a negligible charge/discharge voltage hysteresis revealed the highly graphitic nature of the sample. The graphitic carbon nanosheet showed high reversible capacity (502 mAh/g at 0.1 C), excellent rate capability (461, 429, 305, and 161 mAh/g at 1, 2, 5, and 10 C, respectively) and superior cycling performance (215 mAh/g at 5 C after 2000 cycles and 139.6 mAh/g at 10 C after 3000 cycles).

Finally, carbonized and hydrothermally activated peanut skin has been used to successfully generate porous carbon with high surface area of 2500 m^2/g and a sheet-like structure [143]. These properties enable good rate capability and cycling stability of the carbon sheets. It delivered reversible capacity of 431 mAh/g at rate of 0.1 A/g and 47 mAh/g at rate of 10 A/g vs. Na$^+$/Na.

Sheet-like structure carbon was also successfully prepared from cherry petals [209]. It provided an initial reversible capacity of 310 mAh/g and delivered a high retention rate of 99.3% at 0.02 A/g after 100 cycles vs. Na$^+$/Na. The electrochemical process was also investigated by XPS analysis. The binding energy of the Na 1s spectral region of the electrode was measured during the charge/discharge at 1.6, 1.15, 0.25, 0.1, and 0.01 V. The measurements revealed that the binding energy at a discharge voltage of 0.01 V (1071.4 eV) is greater than that at discharge to 0.1 V (1071.2 eV). This shift to higher binding energy at lower voltage was interpreted by the authors as corresponding to sodium-ion insertion/ extraction in the interlayer of the graphitic microcrystallites due to significant increase in valence of Na. However, the binding energy of the Na 1s spectra from 0.1 V to 3 V is almost constant, which is indicative of Na$^+$ adsorption behavior on the surface of the material at high potential stage.

3.1.4. Porous carbon (3D)

Since the capacitive reactions occur on the surface of the electrode, it is important to use carbon with high surface area [210]. Porous carbon, because of its tunable morphology and surface functionality, offers a wide range of possibilities for improvement and tailored design of a battery anode. According to the International Union of Pure and Applied Chemistry (IUPAC), porous materials are classified into three groups: microporous ($d < 2$ nm), mesoporous (2 nm $\leq d \leq$ 50 nm), and macroporous ($d > 50$ nm) [211]. The micropores is generated from diminishing of functional groups, volatilization of small molecules while the meso- and macropores are originated from the natural structure of the biomass precursor. Ion-buffering reservoirs can be formed in the macropores to minimize the diffusion distances to the interior surfaces [212, 213]. Furthermore, the mesoporous walls provide low-resistant pathways to transport ions through a porous particle, and micropores confine the ions in their voids [214–216].

Drawbacks in the electrochemical energy storage properties can often be overcome by integration of 2D graphene sheets to establish 3D porous and interconnected networks such as films, scaffolds or hierarchical structures. Batteries with porous electrodes offer high power density in addition to high energy density [217,218]. They can compensate large volume if active material is placed in the voids. The foam-like nature of the porous 3D carbons allows the electrolyte to be homogeneously distributed in the entire electrode composite and reach active sites, even in the pore system (e.g. with the help of the capillary effect).

Despite the desirable specific capacity and rate capability of porous carbons [219], they suffer from parasitic reactions, in part because of SEI formation [220], poor Coulombic efficiency [221], and large (1 V or higher) charge/discharge voltage hysteresis [222]. Indeed, porous carbons with high specific surface area provide a large number of free high energy sites that irreversibly trap metals ions. A substantial overpotential is required to remove them [223]. Therefore, biomass-derived carbon with low micropore volume is desirable. For potassium, even mesopores can be beneficial.

Porous carbons are synthesized mainly by hard and soft templating processes [224–226]. Typical hard templates used for the fabrication of porous carbon are porous silica such as MCM-48 [227] or SBA-15 [228], colloidal silica [229], solid core/mesoporous shell silica [230], bimodal porous silica [231], metal carbides [232,233], and other materials. The

porous rigid and stable template is impregnated with a carbon precursor, but the template determines the size and morphology of the obtained carbon. However, removing the hard template is quite difficult, requiring acid or strong base. Another method in which a hard template is used is benign ceramic templating, whereby the template is formed *in-situ* [234–237]. Here, an Mg salt or an Mg-organic compound is mixed with a carbon precursor [238,239]. During the carbonization, the Mg compound converts to MgO at lower temperature, and leaching the carbon/MgO composite yields a porous carbon with a micropore size of 1-1.9 nm. For example, absorption of $Mg(NO_3)_2$ solution on cotton leads to the formation of an MgO-template within the cotton-derived carbon and results in high surface area of 1260 m^2/g [235] .

Nie *et al.* [240] reported the formation of hollow graphene-encapsulated Si particles by the magnesiothermic fabrication and a subsequent CVD process. Mesoporous SiO_2 particles were first prepared by an aerosol spraying process using colloidal silica solution and sucrose as the precursor followed by calcination in air. By reduction of mesoporous SiO_2 spheres via Mg at 900°C, composite particles of Si, MgO, and Mg_2Si were obtained. In the next step via a CVD process and using acetonitrile vapor as carbon and nitrogen source and MgO as template and catalyst, graphene shells were formed on the Si particles. Finally, after selectively removing MgO, Mg_2Si, and unreacted Mg by an acidic treatment, Si particles encapsulated in nitrogen-doped graphene cages were obtained. Another practical way to prepare mesoporous carbon is to employ a hard template with well-ordered regular channels, such as

anodic aluminum oxide (AAO) membranes. Xing *et al.* [188] synthesized mesoporous carbon nanofibers (MCNFs) by using porous anodic AAO membrane and colloidal silica Ludox TM-40 as the dual hard templates, and phenol resin as the carbon precursor. The as-prepared MCNFs material possesses large specific surface area, with a unique hierarchical nanostructure composed of open macroscaled channels derived from the channels of AAO template, in combination with mesoscaled pores developed from the removal of colloidal silica and micropores generated from the carbonization of phenol resins.

In approaches using the soft template, the network is established by amphiphilic copolymer surfactants or other non-inorganic polymer-like formers [241,242]. However, the mesoporous textur of a soft template is usually not as precisely controllable as that of a hard template. The soft template is often formed during the reaction and directs the formation of a porous carbon structure and may be readily removed by solvent washing, thermal decomposition, or different drying approaches [241]. However, the synthesis of porous carbon materials by these methods is complicated, comprises multiple reaction steps with low ultimate yield, and often involves expensive or toxic raw materials. These reasons limit the success of such carbons as many processes show insufficient scalability and can only be produced batchwise depending on the size of the reactor.

Therefore, biomass has attracted considerable attention as a resource. At the correct carbonization conditions, the chosen material preserves its natural pore and cell structure [243–248] which can be of
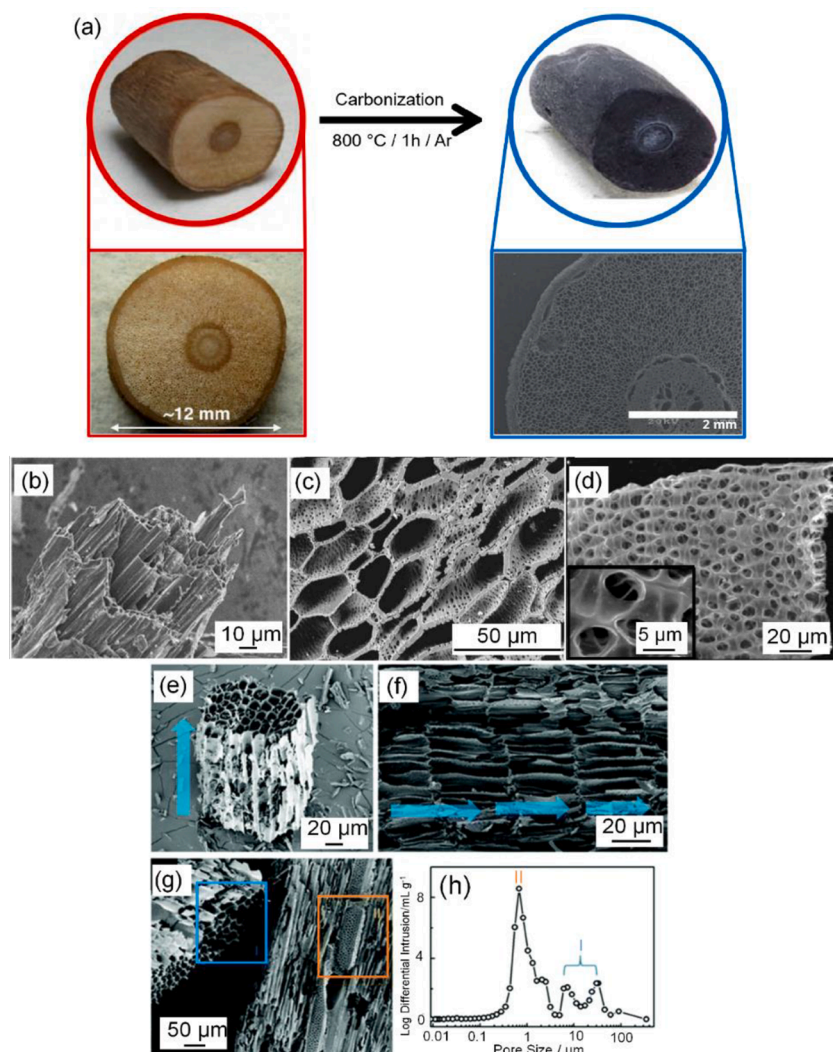
Fig. 10. a) Photographs of a natural red mangrove root piece and the carbonized structure of the aerenchyma tissue with a digital closeup view image and a scanning electron microscopic picture, respectively [247]. SEM micrographs of b) Carbonized porous carbon derived from rice straws at 800°C with post activated with KOH [249], c) Carbonized porous carbon derived from apricot shells [144], d) Carbonized peat moss at 1100°C and post-activated in dry air at 300°C [250], e-g) Carbonized hemp-derived carbon at 800°C and post-activated in steam at 800°C, (blue arrows indicate the primary flow of steam in the reactor), and h) Pore-size distribution of the hemp-derived carbon using Hg intrusion porosimetry with several tens of micrometers (I) and several micrometers (II) [251]. Adopted from mentioned references after the required permission.

interest for e.g. desalination as shown for a red mangrove root [247] or for energy storage applications [248] (Fig. 10 (a)) for which some more examples are given in the following paragraph.

Carbon with parallel macroporous channels was obtained from rice straws (silica fraction as an "*in-situ*" sacrificial template) [249] (Fig. 10 (b)), whereas carbon possessing pore channels with meso- and macro-porous walls was derived from apricot shells [144] (Fig. 10 (c)). Macroporous interconnected networks of carbon nanosheets were extracted from peat moss [250] (Fig. 10 (d)). Finally, channel-shaped pores and porous walls made from hemp [251] (Fig. 10 (e-g)) with diverse pore-size distributions confirmed the feasibility of tailoring pore diameter and pore shape of the carbonized biomass by the various synthesis process. Nevertheless, the original morphology of the biomass is the primary contributor to the pore shape of the final carbon. Fig. 10 (h) shows that channel-shaped pore size and also macro-porous walls of carbon are changed from several tens of micrometers (I) to several micrometers (II), respectively.

Hydrothermal carbonization can offer a green and effective preparation of hydrochars with a controlled distribution of pores from the nanoscale to macroscopic dimensions. In this technique, water is used as the reaction medium at working temperatures of 180–250°C under saturated pressure. The process involves numerous and simultaneously proceeding reactions of hydrolysis, dehydration, decarboxylation, condensation, polymerization, and aromatization of the original precursor. The carbon yield in this case (70–80%) is higher than that obtained by pyrolysis or chemical activation, because of the many functional groups on the surface [252]. However, different components of lignin, cellulose, hemicellulose, and pectin show differing sensitivities toward hydrothermal processes, which strongly affects the characteristics of the derived carbons. Lignin is most resistant to hydrolysis [253].

Some additional steps are needed for increasing the porosities and textural properties of the hydrochars. These include physical activation (that is, partial gasification of chars in an oxidizing atmosphere containing CO_2, O_2, or H_2O at high temperature) and chemical activation (that is, carbonization after impregnation with dehydrating chemical reagents such as Na_2CO_3, K_2CO_3, NaOH, KOH, $AlCl_3$, LiCl, KCl, $ZnCl_2$, and H_3PO_4 at moderate temperature) [254]. $ZnCl_2$ and H_3PO_4, owing to their excellent dehydration characteristics, are widely used in research but also for manufacturing [19]. The mechanism of the activation process is not fully understood. This provides a possible mechanism of activation that high concentrations of $ZnCl_2$ gives Brønsted acidity to the solution and helps dissolve the cellulosic constituents of the biomass [255]. The advantage of using $ZnCl_2$ is found in the evaporation of ZnO if the carbonization temperature is sufficiently high.

In the case of a base, oxygen removes any crosslinking bonds and facilitates the further rearrangement of the graphene layer to assume a crystallite form. Subsequently, the alkali-metal compound is leached out and micropores are created in the structure [256]. The final surface area of porous carbon and the pore-size distribution are influenced considerably by the amount of volatile matter removed during pyrolysis and the concentration of the activating agent for removing carbonaceous species. Dissolution of the reaction products of the activating agent in the carbon can create porosities with a specific surface area up to 3000 m^2/g.

A biomass precursor with a natural pore system is advantageous for chemical activation. Wheat straws have a porous fibrous structure and possess a number of capillaries with strong adsorbability that facilitate the access to KOH in solution, which helps to distribute the activating agent in the whole material. Carbonization and the leaching out of the reacted activation compound leads to the formation of a homogeneously porous material [257].

One study subjected peat moss to carbonization and KOH treatment, accompanied by mild air activation, to produce three-dimensional micro- and macroporous interconnected carbon nanosheets with a specific surface area of 196.6 m^2/g. This process led to a stable cycling capacity of 298 mAh/g after 10 cycles at 0.05 A/g, good cycling

retention of 255 mAh/g at the 210th cycle, and high rate capacity of 203 mAh/ g at 0.5 A/g vs. Na^+/Na [250].

One hard carbon was obtained by pyrolyzing and reducing apricot shells in H_2/Ar at 1300°C [144]. The carbon had a specific surface area of 13 m^2/g and exhibited excellent cyclic stability of 338 mAh/g vs. Na^+/Na after 300 cycle at 0.4 C, because of high sloping and plateau capacities. Hydrogen treatment appears to be beneficial to remove oxygen from the carbon to facilitate the rearrangement of the graphene layers and to allow for a microcrystalline orientation along the *a*-axis, which results in a little bit smaller d_{002} and L_c, and larger L_a. The change in the structure and reduction in the defects concentration due to dangling bonds or oxygen-containing covalent bond, resulted in the outstanding reversible Na-storage capacity of the obtained material. Samples pyrolyzed at lower temperature and without H_2 possess a high level of defects compared to the carbon reduced by hydrogen. The electrochemical characterization of these carbons revealed better performance at high rates of up to 4 C, which demonstrates the favorable behavior of highly defective carbon for fast Na^+ ion diffusion resulting from the higher interlayer distances [144]. However, hard carbon that is carbonized at low temperature and with high level of defects suffers from low electronic conductivity owing to its disordered microstructure [114]. Fingolo *et al.* [258] showed annealing under isopropanol vapors enabled to increase the sp^2 carbon content and degree of graphitization of the biocarbons, which has improved electrical conductivity of these materials by up to three times.

3.2. Element-doped carbon materials

Although many novel materials have been proposed as anode materials for metal-ion batteries, only a few exhibits the efficiency required for anodes for alkali-metal storage. For example, hard carbon, metal alloys, and metal oxides.

Hard carbon has received most attention because of its potentially low production cost, abundant resources, and its high storage capacity suitable for use as a battery anode material. The performance of hard carbon anodes can be enhanced by heteroatoms substituting for carbon atoms in the graphene layers. Doping of carbon atoms by heteroatoms, such as nitrogen, boron, phosphorous and fluorine and etc. with electron acceptor or donator capability, changed bond distances due to the substituted heteroatom, single or multiple doping and the total amount of heteroatoms in the carbon structure, can provoke disorder in the carbon structure and provide a higher number of point defects which may facilitate metal ion transport through modulated band structure of the graphene layers [259,260]. These modifications contribute to enhanced charge-carrier-transport kinetics by influencing the electronic conductivity [261,262].

However, the synthesis method for doping the graphene sheets in a defined way is the main determinant of whether the heteroatoms are incorporated into functional groups or directly into the graphene lattice. This, in turn, affects the final electronical and electrochemical properties [263]. Most of the biomass materials naturally contain inevitable heteroatoms such as N, O, P and K. The carbonization of biomass containing doping elements are performed at relatively low temperatures of 600–1100°C. At higher temperature the doping level decreases dramatically. The formation of large amounts of defects and micropores in such a low temperature-treated hard carbons, hinders the crystallization of the hexagonal carbon structure (small L_a and L_c values) and finally increases the contribution of high-voltage sloping capacities in the voltage profile. Although, the interlayer spacing of graphite increases with some doping elements like P, which extends the low-voltage plateau capacity, while increasing the defect concentration with the doping element leads to higher sloping capacity. With an elevated carbonization temperature and a continued crystallization process to the ordered hexagonal carbon structure, the low-voltage plateau capacity becomes more prominent [264,265].

Table 1 lists the elemental composition of some types of biomass

including nitrogen, carbon, and oxygen, together with phosphorus oxide (P_2O_5). A more complete list for 86 biomass varieties is presented by Vassilev [266]. Despite the positive effect of heteroatoms on the electrochemical performance of hard carbons, the attention should be paid to presence of unwanted impurities such as Al_2O_3, SiO_2 and CaO and etc. in biomass which can have a negative effect on the anode performance. Hot washing and acid leaching can reduce the concentrations of alkali metals and alkaline earth metals. For example, animal bone is primarily composed of hydroxyapatite (HA, $Ca_x(PO_4,CO_3)_y(OH)$) which can be removed with diluted hydrochloric acid. However, the removal of silica and alumina from biomass is more laborious [267,268]. The hard carbon derived from washed and unwashed pinecone biomass treated at 1400°C was reported to have a capacity of 328 mAh/g and 299 mAh/g vs. Na^+/Na, respectively. After 100 cycles, a drop-in plateau capacity was observed for the unwashed sample. This decay was explained by the sodium-ion-insertion process being hindered by impurities that occupy some active sites [102].

3.2.1. Nitrogen doping

Nitrogen, owing to its higher electronegativity of compared to carbon with 2.5 increases the repulsive interaction between carbon layers and enlarges the interlayer spacing, which is expected to improve Na^+ ion battery performance [269,270]. It has been reported the carbon doped with electron donors such as N exhibit greater conductivity than that of carbon doped with electron acceptors [271]. Nitrogen doped into graphene exists in three main bonding configurations: pyridinic, pyrrolic, and as graphitic nitrogen. The high-resolution N1s XP spectrum of nitrogen-doped carbon derived from bamboo was fitted with four different species with binding energies of 398.8, 400.3, 401.5, and 403.7 eV. These correspond to pyridinic nitrogen, pyrrolic nitrogen, graphitic nitrogen (the most stable nitrogen species after carbonization), and N-O bonds, respectively [272]. Graphene doped with electron-rich graphitic N due to electrostatic repulsion between N and Li shows more efficient delithiation while pyridinic and pyrrolic N formed at the edges and defect sites promote the perpendicular diffusion of Li. It is known that pyridinic N (sp^2-hybridization) bonded with two carbon atoms and pyrrolic N with sp^3-hybridization can create defects to provide active sites for alkali-metal ion storage. With an increasing pyrolysis temperature up to 1100°C, the specific capacity decreased congruently with the content of the pyridinic nitrogen. This behavior indicated the significance of a high nitrogen content for the realization of high performance LIBs [273]. Graphitic N (sp^2hybridized) bonded with nitrogen atoms, which substitute carbon atoms in the hexagonal structure, can enhance the conductivity of carbon [274]. This property is explained by the engagement of one electron in the formation of a π bond while the other electron is partially localized in the π*-state of the conduction band. (Fig. 11 (a)). In a nitrogen-doped graphene layer, pyridinic N and pyrrolic N donate one and two electrons, respectively, to the π-system of the carbon to give the carbon network a partially negative charge, which enhances the electrochemical activity for Na and K-storage. However, in these two structures the Fermi level is shifted slightly to the valence band since the defects impose the *p*-type effect by withdrawing electrons from the graphene sheet.

The materials with high protein content, such as soybeans [275],

bean shells [92], egg white [276], ginkgo leaves [277], human hair [278], chitosan [279], catkin [280], grass [281], and typha orientalis [136] can yield carbon with high nitrogen content. In plants, N concentrations are expected to be higher in the leaves than in the roots [282]. Nitrogen in biomass varies usually from 0.1 to 12 wt.% and, in general, the highest and lowest N contents in biomass have been observed in animal waste and wood, respectively [266]. Biomass with a protein concentration of approx. 50 wt.% can contain nitrogen between 8 and 10 wt.% [283]. The chemical-activation process and carbonization temperature are the two main factors that define the N-content in carbon. Increasing the temperature and including an activating agent, e. g. to reach a porous structure and high specific surface area, can significantly decrease the N content. Therefore, it is quite challenging to design carbon that simultaneously possesses high surface area, high N content, and partially graphitized structure [284].

Sun *et al.* [285] used pomelo peels to produce carbon with a high surface area, a uniform mesoporous structure, and an ultra-high nitrogen doping level of 14.51 wt.%. Li *et al.* [137] also succeed in obtaining hierarchical mesoporous carbon from eggs, with a surface area of 806 m^2/g and a bulk N-content of 6 wt.%. This carbon exhibited a reversible discharge capacity of 1780 mAh/g at 0.1 A/g as LIB anodes. Hou *et al.* [205] reported a reversible Li-storage capacity of 1865 mAh/g at 0.1 A/g for hierarchical porous nitrogen-doped carbon derived from silk with nitrogen contents of 4.7 wt.%. Yang *et al.* [127] demonstrated that the carbonization of okra, followed by an exfoliation process, led to carbon with nitrogen content of 9.89 at%. The carbon exhibited high specific capacity of 292 mAh/g and extremely long cycle life exceeding 2000 cycles vs. Na^+/Na.

Due to improvement in the electrical conductivity and wetting behavior of the electrode/electrolyte contact [286], N-doped carbons can also give high rate capabilities, along with long-term cycling stability. Chen *et al.* [257] showed the pretreatment of wheat straw as raw material with HCl, followed by an activation by KOH during the carbonization process, resulted in the successful fabrication of nitrogen-doped porous carbon with thin pore walls. Such carbon, owing to the content of nitrogen up to 5.3 wt.%, exhibits high specific capacity, long-term stability of 976 mAh/g at 0.37 A/g after 300 cycles and, in particular, ultra-high rate capability of 198 mAh/g, even at a current density of up to 37 A/g vs. Li^+/Li.

Disordered nanocrystalline carbon fibers extracted from lignin possess low flexibility if they are not mixed with any synthetic polymer, which causes unstable rate capacity and poor cycling performance [287]. Higher molecular weight lignin also showed enhanced graphitic structure with improved mechanical properties [288]. Tenhaeff *et al.* [289] reported that the lignin carbon extracted from hardwood and treated at 2000°C showed a specific capacity of only about 100 mAh/g at a current density of 0.015 A/g over 40 cycles. In recent years, studies have reported the development of nitrogen-doped lignin as a precursor for carbon with high stability against electrolytes at low potentials and improved energy/power performance [290–292]. Zhao *et al.* [293] showed lignin-derived nitrogen- doped carbon delivered a high cyclic stable capacity up to 225 mAh/g at a current density of 0.06 A/g after 50 cycles. Nitrogen can be doped artificially into carbons especially those extracted from lignin-enriched biomass [294] via chemical vapor deposition [295], thermal annealing in NH_3 [296], N_2 plasma treatment [297], alkaline treatment [294], an arc-discharge method [298], or mechanochemistry [299].

Mechanochemistry entails the induction by mechanical energy (i.e. grinding, milling, ultrasonication, etc.), which enables reactions by reducing the particle size, breaking chemical bonds, and creating new surfaces. Because of the relatively simple procedure and, in most cases, substantially reduced post-reaction treatment, this synthesis method is regarded as cost-effective and efficient for promoting chemical reactions between solids without the need for solvents. Schneidermann *et al.* [299] have reported the synthesis of nitrogen-doped carbon using a mixture of lignin, urea, and K_2CO_3 with a mechanochemical process. The mixture

Table 1
Chemical composition of four groups of biomass [266]

Biomass group	N (wt. %)	P_2O_5 * (wt.%)	C (wt. %)	O (wt. %)	Enriched in
1. Wood	0.4	3.5	52.1	41.2	CaO, SiO_2
2. Herbaceous and agricultural crops	1.2	6	49.3	42.9	K_2O, SiO_2
3. Aquatic biomass	2.2	9.8	43.2	45.8	Na_2O, SO_3
4. Animal waste	9.2	28.2	58.9	23.1	CaO, P_2O_5

* Chemical ash composition
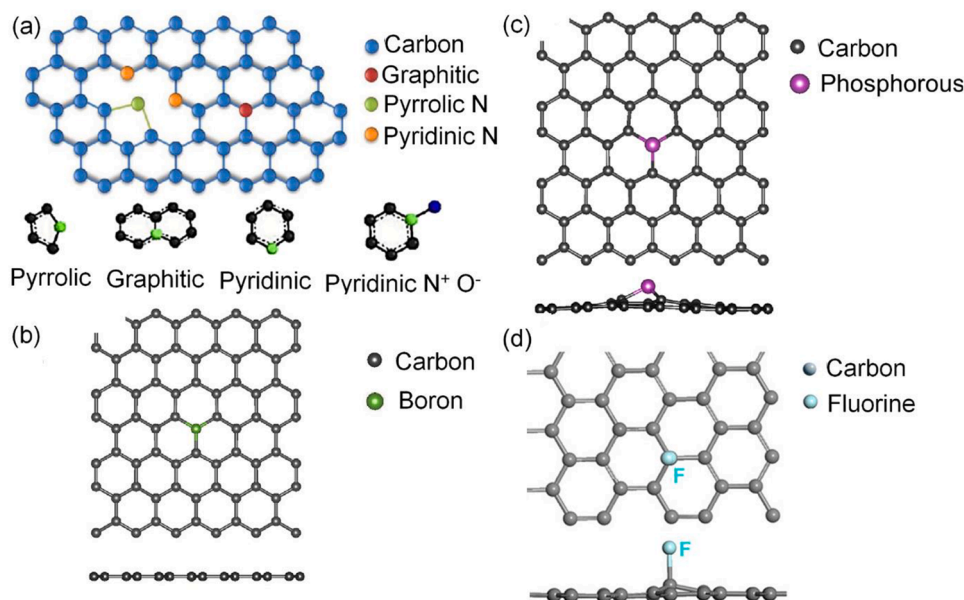
Fig. 11. A schematic of various types of bonding configurations of a) N [180],[344],[345], b) B [346], c) P [346], and d) F [347] atoms within the hexagonal lattice. Adopted from mentioned references after the required permission.

was milled in a zirconia vessel for 30 min, and the product was pyrolyzed in nitrogen at 800 °C for one hour.

The accurate control on nitrogen content and the ratios of different types of nitrogen species in some nitrogen-rich biomass are difficult. Enabling the desired nitrogen content and its homogeneous distribution in biomass-derived carbon, requires removal of nitrogen as gaseous nitrogen oxides (NO_x) during pyrolysis. This results in the formation of mesoporous and microporous structures. Then the carbon can be subsequently doped with a desirable level of nitrogen by means of post-treatments in the presence of various nitrogen sources such as ammonia (NH_3), urea, and nitrogen gas (N_2). These structures are beneficial to enhance the electronic conductivity of carbon [273].

3.2.2. Boron doping

Doping with boron improves graphitization by increasing the interlamellar spacing L_c and L_a. As shown in Fig. 11(b), B-C σ-bonds are considerably polarized owing to the larger electronegativity of carbon with respect to boron, which induces a positive charge of 0.56 e in the boron atom [300]. The larger bond distance of B-C (1.48 Å) than that of C-C (1.41 Å) increases L_a [301–304]. Indeed, boron, with a lower electronegativity (2) than carbon, removes π electron density in the graphene layers, which reduces the repulsion between the graphene layers. B substitution creates an electron-deficient lattice because of the formation of trigonal coordination with sp^2-hybridized bond character. The three bonds tend to increase the in-plane local defects in the carbon structure and therefore make it facile to accommodate for extra electrons [223]. Graphene doped by electron accepting dopants like B shows different electronic properties compared to graphene doped by electron donating dopants such as N as revealed by the higher conductivity of the N-doped graphene. With boron doping electron holes are generated acting as a trap for free electrons. In the consequence, a strong decrease of free carrier mobility and conductivity is recognized [271].

As boron is not an element typically involved in plant growth it needs to be added before the pyrolysis. Boron is blended by using boric acid [305], ammonium hydrogen borate [306], or triethyl borate [307], and substitutes carbon atoms in the graphene layers. The binding energy of B1s in XPS for boron substitution in the carbon lattice shows a peak ranging between 186.9 and 188.8 eV [308]. Additionally, the various boron oxides and carbides (BC_2O, BCO_2, B_2O_3, and BC_3) formed on the carbon surface have B1s peaks ranging from 189.0 to 193.2 eV [309].

Endo *et al.* [310] observed a B1s signal near 190 eV which is related to formation of boron nitride and BC_xN sites. They reported that the formation of these compounds is followed by a reduced Li insertion capacity compared to pure boron doping. Nevertheless, B can also stabilize Li^+ ions and, therefore, prevents the clustering of Li species. By easily transferring the Li 2s electrons to BC_3, with the electron density mainly concentrated on the B atom (due to *p*-type behavior), and filling the usually empty p_z state of the B atom, BC_3 binds stronger to Li in comparison with graphite. BC_3 sheets can provide a specific capacity of 857 mAh/g, which is 2.3 times higher than for graphite. However, due to presence of in-plane local defects, parallel diffusion of Li^+ ion to plane can be less efficiently [179,311]. Endo *et al.* [310] also reported an occupation of Li insertion active sites, such as edge-type sites, in the carbon layers with B that inhibited the Li insertion process and reduced the charge capacity of the boron-doped samples.

B-doped carbon is also a highly promising candidate as a sodium storage material. Owing to the electron acceptor effect of the boron in the carbon lattice, the Na and Li insertion starts at higher voltage of about 0.92 V and 1.2 V for B-doped graphene sheet. However, we should note that any oxygen in the hard carbon could increase the voltage up to even 2.52 V [223,312–314]. By doping B in the carbon structure, the positive binding energy between the graphene sheet of the hard carbon and Na changes to a negative value. B^{3+} transfers three electrons to the graphene sheet, which leads to strong interaction between the Na atoms and the graphene sheet in the vicinity of the B atoms. Another reason for this strong ionic interaction could be found in the *p*-type property of boron, which could easily accept an electron from the sodium atom while it is weaker at e.g. electron-abundant N-substitution sites. All these properties of boron direct the charging and discharging electro-chemistry to the slope capacity rather than the plateau capacity. The high binding energy between the B-sites and the Na^+ ions caused a reduction in Na^+ ions motion and trapped Na^+ ions in the carbon structure that led to an extremely low potential plateau and a high irreversible capacity in the first cycle [223]. However, the first-cycle Coulombic efficiency could increase by decreasing the specific surface area of the hard carbon to less than 8.0 m^2/g [223]. Another study subjected to potato starch, the boron-doped carbon was prepared in a two-step hydrothermal reaction and carbonization with a yield of about 2 at.%. The electrochemical performance showed the high reversible specific capacity of 964 mAh/g at a current density of 0.2 C. The carbon

also exhibited a good cycle ability with a specific capacity of 356 mAh/g after 79 cycles at a current density of 0.5 C vs. Li$^+$/Li [315].

3.2.3. Phosphorous doping

P–C bonds could enhance electrical conductivity by increasing the electron density around the Fermi level [316]. In contrast with boron, phosphorous atoms maintain their sp^3-configuration. Because of its large atomic size, phosphorous usually avoids substituting for carbon in the graphene layers and prefers edge sites instead [174]. Nonetheless, phosphorus forms a quasi-trigonal pyramidal coordination with carbon atoms with P-C σ-bond lengths of 1.76 Å. The higher length of P-C (1.54 Å) than that of C-C forces phosphorous atoms to locate out of the plane. TEM studies also confirm the short and curved graphene layers in P-doped hard carbon. This protrusion is driven by the rehybridization of p_z states of the vacant C sites toward the stabilization of the P-C system, which results in larger charge transfer between the P and C atoms as compared with e.g. the N-C system [199] (see Fig. 11(c)). Although P shows similar chemical properties as N, doping the carbon matrix with P shows a higher electron-donating ability and stronger *n*-type behavior compared to the N-doping [317]. Jeon *et al.* [318] reported doping of carbon with non-metal elements with an electronegativity <2.55 like P. Donating electrons to the C atoms and the low electronegativity, like in the case of P doping, causes stronger interaction of an intercalated metal ion compared to N-doped graphite. P-doping not only improved the capacitive performance, it also resulted in an enhanced energy density compared to the respective N-doped carbon.

The P$_2$O$_5$ content of biomass varies from 0.2–41 wt.% and its content is highest in animal waste and agricultural residues [266]. Phosphorous is usually doped into carbon with the help of phosphoric acid [319], triphenylphosphine [320], ammonium phosphate [321], monosodium phosphate [322], etc.

Lu *et al.* [323] succeeded in P doping into cotton-derived carbon that led to the weakening and breaking of C=O and partially C-O bonds as referred to the change in the XPS contributions at binding energies of 533.1 and 532.0 eV, respectively. The phosphorous atoms were inserted into the C-O bonds to form C-O-P groups. The doped material delivered a reversible capacity of up to 242 mAh/g at 0.05 A/g, excellent rate capabilities of 123 mAh/g at a high current of 1 A/g, and long-term cycle life with ~88% capacity retention after even 600 cycles. Electrochemical impedance spectroscopy (EIS) and galvanostatic intermittent titration technique suggested that P-doping caused the decrease of the charge-transfer resistance alongside drop in contact angle and improved of Na$^+$ ion migration kinetics as deduced from ref. [324].

Ji *et al.* annealed a mixture of H$_3$PO$_4$ and sucrose to obtain PO$_x$-doped hard carbon as an anode material, which improved the capacity of un-doped carbon from 283 to 359 mAh/g. The more intense signal of phosphorous oxides at 134.5 and 133.1 eV positions than that for the P-C bond at 131.0 eV points to the presence of oxygen atoms in most of the doped phosphorus species. Although PO$_x$ as a redox inactive agent could not contribute to the higher capacity, but caused an enlarged 002) d-spacing and domain defects, which finally resulted in plateau and slope regions that were shifted to higher potential profile values [325]. This larger d-spacing enables a vital Na-ion transfer, as indicated by an increased sodiation plateau capacity that is much more pronounced than the slope capacity [223]. A lower sodiation voltage of ≈0.32 V was observed in the potential profile, which can be attributed to *n*-type behavior of the P dopant that could not accept an electron from the sodium as easily as B [223]. Additionally, a P−O bond in carbon changes the morphology and composition of the solid electrolyte interface (SEI) layer and is beneficial to the formation of a thin and dense SEI layer [326].

The high-resolution P2p spectrum for P-doped carbon deconvoluted into three peaks at C$_3$PO (132.9 eV), C$_2$PO$_2$/CPO$_3$ (134eV), and C$_3$P (130.5eV). The spectrum showed that after co-doping with B, C$_3$P increases from 7.2 at. % to 22.8 at. %, which consequently results in a reduced irreversible capacity in SIBs [327]. Xing *et al.* [328] prepared

phosphorus-doped sunflower-activated carbon with simple hydrothermal and calcination methods. They reported a reversible capacity of 1000 mAh/g after 200 cycles at a current density of 0.5 A/g for LIB.

3.2.4. Fluorine doping

The crystal structure of graphite fluoride has gained great importance in improving the electrochemical performance of batteries [329]. Halogen atoms exhibit both the electron-withdrawing effect owing to the high electronegativity and the resonance-donating effect as a result of the existence of lone pair electrons [263]. Such influence causes the transformation of the sp^2-carbon bond to the sp^3-state. The high electronegativity induced by fluorine-doping enhances Na$^+$ ion transportation and storage by weakening the repulsive force for Na$^+$ ion insertion and removal. This phenomenon reduces the energy barrier for Na$^+$ ion insertion and offers more active sites for Na$^+$ ion storage.

Because of strong repulsion between the paired electrons of F and unpaired electrons of the unbonded adjacent carbon atoms, the F-C bond sticks out of the basal plane and stretches the C-C bond length to 1.57~1.58 Å (Fig. 11 (d)) [330,331]. Increasing D and D′, broadening of the G, and decreasing 2D bands in Raman spectra show the disorder in the graphene layers which is further intensified by F-doping [332,333]. XPS analysis of the carbon spectrum after fluorine saturation at 50 at. % shows that a majority of the bonds are C−F, C−F$_2$, and C−F$_3$. Covalent bonds of C−F$_2$ and C−F$_3$ appear at binding energy levels higher than 292 eV in the XPS spectrum, which confirms the formation of C−F$_n$ at defects such as vacancies, free edges, or domain boundaries [332]. In the graphite fluoride (CF$_x$) materials, the property of the C–F bond depends on the fluorine concentrations. For $x < 0.1$ the type of the bond between carbon and fluorine is ionic, located at 289.8 eV, which leads to an extremely high electrical conductivity of 2×10^5 S/cm. For higher fluorine concentrations the conductivity of the graphite fluoride decreases because of the formation of less ionic but more covalent C–F bonds, which were detected at 291.8 eV [334,335]. Indeed, the ionic bonding keeps the planar nature of the graphene planes, whereas the interaction of the p orbitals of F with the π orbitals and the introduction of a large strain into graphene planes pushes the carbon out of the graphene plane in covalent bonding [333,336]. Therefore, the covalent C–F bonds (bond length of 1.41 Å) consist mainly of sp^3-hybridized C atoms and F atoms with a binding energy of 114 kcal/mole, whereas ionic C–F bonds C$_x$F (bond length of 3 Å) with $x > 3$ mainly originate from sp^2-hybridized C atoms bound to F atoms with binding energy of 13 kcal/mole [333,337]. The semi-ionic C–F bond (bond length of 1.7 Å) is an intermediate state between covalent and ionic bond and has higher polarities than covalent C–F bonds, which result in higher positive charge on the respective carbon atoms, a larger graphite interlayer distance as well as a higher electrochemical activity than the covalently bonded ones [334]. In addition, semi-ionic C–F bonds with high (partial) electronegativity on the graphite surface accelerated the diffusion of Li$^+$ ions in the charge/discharge process. Although the ionic nature of the C–F bonds is known to induce even higher electrical conductivity. It also offers an active site for the formation of the SEI and consequently increases the irreversible capacity. C–F covalent bonds as strongest type among the C–F bonds, tend to irreversibly form LiF. High covalent C–F bond ratio might destroy the conductive network of conjugate double bonds and finally reduces the discharge capacity [338]. This bond type also deforms the graphite surface structure which allows for the storage of excess lithium [339]. However, the presence of a negative charge (oxygen functionalities) and also the disordered lattice structure can hinder the formation of the semi-ionic C–F bond and LiF formation [340]. As the surface doping is more relevant for LIB, intercalation of fluorine to form semi-ionic C–F bonds is beneficial in the case of KIB as the graphene interlayer distance increased and enabled an elevated electrochemical performance [341,342].

The fluorine-doped carbon particles derived from *lotus petioles* for SIB deliver an initial charge capacity of 230 mAh/g at a current density of 0.05 A/g. They also maintain a charge capacity of 228 mAh/g at 0.2 A/g

as well as a stable capacity of 126 mAh/g at a rate of 0.5 A/g for 300 cycles. This electrochemical performance may be related to the higher electronegativity of fluorine (4) compared to carbon (2.6), which increases the repulsive interaction between the carbon layer to interplanar spacing (0.41 nm), as well as the disordered structure [343]. F atoms have the highest electronegativity among all the elements, and, therefore, they induce the highest positive charge on carbon atoms.

3.2.5. Metal-ion doping

The low electronic conductivity of hard carbons and the slow transport of metal ions in the hard carbon electrodes during the discharge and charge processes originate from the different stacking orientations of few-layer graphene clusters. These two main obstacles hamper high rate capabilities in alkaline ion batteries. As intentional introduction of some metal elements into graphite as a dopant showed the doping metals can tune electronic properties, surface polarities and catalytic performances [348,349], hence a similar effect can be expected for hard carbons.

Large anisotropy of electronic conductivity of pristine graphite at room temperature ($\sigma_{a\ axis}$:σ_{caxis}>100) can be significantly modified with intercalation of electron donor species [350,351]. Introduction of alkali and alkaline-earth metals into graphite by increasing the in-plane and, especially, the c-axis conductivity, convert the two non-superconducting components to superconducting compounds. Alkaline and alkaline-earth metals are intercalated between the graphene layers based on their sizes [352]. Elements with smaller ionic radii like M = Li, Ca reach a stoichiometry of MC_6, and for those with larger ionic radii like M = K, Rb, Cs the compound MC_8 are expected to be formed as the final constituent. The classical synthesis method to intercalate the metals into interplanar graphite is the reaction of solid graphite with the vaporized metal at moderate temperatures in high vacuum. Due to high vapor pressure of K, Rb and Cs, these elements can easily intercalate into graphite at low temperatures to form crystallographically ordered compounds up to MC_8. For smaller metals like Na due to their low vapor pressure, the intercalation into graphite is more challenging [353]. However, Na^+ ions that are unable to intercalate into undoped and unexpanded graphite can intercalate into B-, P-, and Al-doped graphite. Transferring electrons from B, P, and Al dopants to graphite strengthens the ion-graphene electrostatic interaction and provides the thermodynamic driving force for Na^+ ion intercalation. The intercalation of Na^+ ions into graphite increases in the order of N < B < P < Al, which is associated with the electronegativity of the dopant [318].

However, in spite of the weak vapor pressure of Li and its lower electropositive character than Na, Li intercalates into graphite surprisingly easy. Li-graphite intercalation compounds (Li-GIC) showed less air stability compared to heavy alkali metal-GIC and rapidly decomposed. Electrical conductivity of Cs-GIC was estimated to around 5×10^4 S/cm after 10 years exposure to air [354].

In addition, less electropositive alkaline earth metals such as Ca, Sr and Ba with lower volatilities compared to alkaline metals incompletely intercalate into graphite and lead to the formation of mixtures of graphite and the intercalated product as these elements are usually carbide formers. However, Cahen et al. reported on the intercalation of Sr, Ba and Yb into graphite, using a LiCl–KCl molten salt as the reaction medium [355,356].

It was speculated that hard carbons with expanded graphite can be an effective alternative to the complex uncontrollable doping synthesis by metal vapors. However, due to cross-linking of the graphitic planes, alkaline metals cannot intercalate into non-graphitizable carbons sheets. Note, the enlarged interlayer spacing of alkaline intercalated graphite was observed in disordered carbon prepared from cellulose yarn and glassy carbon [357–361]. Shi et al. [362] also showed an accelerated rearrangement of the carbon during heating for amorphous carbon containing alkaline metals, during the penetration of molten alkaline metals into a porous carbon and by etching the O-containing surface groups. McNamara et al. [363] observed the important role of Cs on

carbon ordering of polyfurfuryl alcohol-derived carbon which was more significant compared to other alkaline metals. Coconut endocarp derived carbon with an expanded d_{002} spacing of 0.4 nm originating from natural K-doped graphitic layers with K-contents of 6654 mg/kg showed a high initial reversible capacity of 314 mAh/g and a good cycle stability of 289 mAh/g after 200 cycles [364].

The low electronic conductivity of hard carbons can also be tackled by introducing transition metals into the hard carbon matrix to some extent to partially graphitize its structure [365,366]. Nevertheless, the intercalation of the low volatility transition metals into graphite is difficult, and in most cases impossible as carbide formation is preferred [355,367]. Therefore, it is expected for hard carbons like for graphite that the insertion of transition metals takes place rather than an intercalation. In contrast to the ionic character of the graphite−alkali metal bonds, transition metal atoms are covalently bonded within the graphene layers. These strong covalent bonds cause large in-plane lattice distortions of the graphene layers [368,369].

An increase of the carbonization temperature and a faster activation process enhance the reorganization of disordered carbons and act as two main factors which favor a higher electrical conductivity of such a hard carbon [370]. However, transition metal dopants such as Cr, Fe, Co, and Ni can significantly decrease the graphitization temperature. Finding the transition metal with proper catalytic activity in carbon materials, mass ratio of hard carbon and transition metals and also selecting the optimum pyrolysis temperature of the metal-carbon composite plays an important role on the degree of carbon organization and on the resulting electronic conductivity. Additionally, introducing the first-row transition metal elements such as Co, Fe, Mn and Ni into carbon materials enhance capacitance and electrocatalytic properties of the respective carbon materials and can be selected as a promising alternative for the replacement of precious metals [371–374]. The ability of transition metals to act as a graphitization catalyst increases with its number of electron vacancies in the d-orbitals. Elements with fully occupied d-orbitals (e.g. Cu, Zn) are relatively inert in a reaction with carbon. Elements with partially occupied d-orbitals (e.g. Fe, Co) are effective carbon solvents. Elements with less occupied d-orbitals (e.g. Ti, V) are carbide formers [375,376].

Maldonado et al. [377] reported various degrees of hard carbon graphitization using different transition metals. The results showed that I_D/I_G ratio of 0.87, 0.99, 1.07 and 1.08 can be obtained when hard carbon is catalytically graphitized at 1000°C by Cr, Ni, Fe and Co, respectively. However, by increasing the pyrolysis temperature to 1800°C, the order of graphitization changed to Cr (0.71) ˃ Fe (0.78) ˃ Co (0.96) ˃ Ni (1.01). Using Cr as a catalyst resulted in a decrease in the graphite interlayer spacing from 0.382 to 0.337 nm at 500 and 1800°C, while, that of pristine hard carbon reduces to the minimum of 0.364 nm at 1800°C.

Araujo et al. [85] demonstrated among the transition metals of Fe, Ni and Cu, nickel acted more effective as the catalyst for graphitization of carbon derived from cotton and the degree of graphitization enhanced with increasing the temperature from 800 to 1200°C. The electrical conductivity of catalytically graphitized carbon was determined using a four-point probe showing that Ni catalyst can increase the conductivity of graphitized carbon to 27.96 S/m which provides the best performance among other metal catalysts. The negative ζ-potential value for graphitized carbon with Fe and Cu catalysts showed the insertion of oxygen and nitrogen atoms into the graphite during pyrolysis. However, the positive ζ-potential value for the carbon with the Ni catalyst contribution resulted in a low-defected carbon material with less electronegative atoms in the graphite.

A glucose-derived carbon, catalytically graphitized by Fe at 450°C for 6 hours in Ar/H_2, delivered a remarkable specific capacity of 167 mAh/g at 1 A/g, and a cycling stability of 201 mAh/g at 0.5 A/g vs. Na^+/Na after 100 cycles [366]. Carbon derived from glucose without an additional catalyst exhibited only 70 mAh/g compared to that of graphitized carbon with a specific capacity of 420 mAh/g at 0.05 A/g in

the first cycle, which demonstrates the importance of the Fe catalysis during the carbon synthesis. Besides the catalytic effect of Fe, a larger size of the Fe nanoparticles leads to a smaller graphite interlayer distance and an increased stacking of the layers. Obrovac *et al.* [365] also reported on the reversible capacity obtained by Fe-catalyzed graphitization of sugar carbon at 1200°C under a flow of argon. The high capacity of 366 mAh/g after 30 cycles at C/5 vs. Li$^+$/Li is indicative of a high degree of graphitization and low turbostratic disorder.

Hunter *et al.* showed a fast formation and growth of the Fe$_3$C catalyst results in quicker graphitization for cellulose and glucose compared to starch. The presence of a large yield of disordered graphene sheets in carbonized starch blocks the mass transport of iron and thus restricts the growth of the Fe$_3$C nanoparticles. Therefore, it takes longer for the Fe$_3$C nanoparticles to reach the critical size needed for a significant contribution to the graphitization [378].

3.2.6. Dual-doped carbon

As already discussed in the previous sections (3.2.1-3.2.4), the difference in electronegativity between carbon atoms and heteroatom doping induces the charge distribution over the carbon network that alters the electrochemical performance of graphite. Therefore, it could be expected that synergetic effects of co-doping elements with higher and lower electronegativities than that of carbon could be much more pronounced than singly-doped carbon [301,379].

With the pyrolysis of hydrolyzed chicken egg yolk and Fe(NO$_3$)$_3$ up to 1000°C in N$_2$ atmosphere nitrogen- and phosphorous dual-doped nano carbon capsules were obtained [128]. The yolk contains nitrogen- and phosphorous-based compounds, which were reduced and substituted carbon atoms in the carbon structure. Subsequently, capsule-like carbon structures were formed by precipitation and graphitization of C on iron particles. Finally, Fe was removed by an acid treatment and hollow-structured carbon was obtained. High resolution C1s spectra were fitted with four species at binding energies of 284.7, 285.5, 285.8, and 287.8 eV, which are attributed to sp^2 C–C, C–P, C–N, and C–O bonds, respectively. This result suggests that dual doping of N and P atoms into the carbon occurs. Galvanostatic discharge/charge cycles for this dual-doped hollow carbon showed that the contribution of the specific capacity below 0.5 V corresponds to the intercalation of Li cations into the layer of the carbon shells. The capacity above 0.5 V was ascribed to the capacitive contribution on the outer/inner surfaces and edge planes of the capsule structure. However, no obvious voltage plateau was observed during the cycle suggesting a disordered stacking of the dual-doped carbon. The reversible capacity as high as 770 mAh/g at 0.5 A/g, with a rate capacity of 380 mAh/g at 15 A/g, supported that heteroatom doping provides additional Li intercalation sites beneficial for the electrochemical properties [128].

Corn husk doped naturally by nitrogen and oxygen treated by KOH solution delivered a reversible capacity 231 mAh/g at 0.1 A/g vs. K$^+$/K. Moreover, at a high current density of 1 A/g, the reversible capacity still reached up to 135 mAh/g after 500 cycles. The results indicate that both capacitance and diffusion are responsible for the K-cation storage in battery [380]. Although oxygen may have a negative effect on the conductivity of the carbon network, it improves the wettability of carbon surface by the electrolyte to reduce the carbon inactive sites and offer more sites exposed for charge storage [381].

N and P have been successfully doped into carbon sheets derived from corn stalks via a hydrothermal reaction using (NH$_4$)$_2$HPO$_4$ as the source of nitrogen and phosphorus. Since sp^2 C–N and C–P may overlap with C–O contribution in C1s XP spectrum, and the sp^3 C–N with C=O, information about successful doping of nitrogen and phosphorous into carbon sheets was obtained by fitting the high-resolution P2p XP spectrum. Three contributions were assigned to the intense parts of the signal at binding energies of 132.1, 133.1, and 133.6 eV. These energies were assigned to P–C, P–O, and P–N bonding, respectively. N and P as doping elements have been reported to improve electron conductivity and enable a higher electrolyte-surface-wetting ability of the carbon. This

carbon delivered a specific capacity of 277 mAh/g after 100 cycles at 0.25C and a specific capacity of 202 mAh/g after 200 cycles at 1C, as well as a stable specific capacity of 105 mAh/g at a high rate of 5C after 2000 cycles. These results point to the excellent cycle stability and superior rate capability of dual-doped carbon sheets derived from corn stalks [382].

Zhao *et al.* [383] used density functional theory (DFT) calculations to predict the behavior of N doping in a P-doped carbon. P bonded to carbon in two modes, outside the carbon surface or inside (means doped into the carbon surface) (Fig. 12 (a-b)). The inside mode caused a distortion of the 2D carbon framework. P bonded to carbon according to these two modes decreased the formation energy E$_f$ of graphitic N to 0.14 eV for the outside mode and 0.32 eV for the inside mode, as compared with un-doped carbon with an E$_f$ of up to 0.40 eV. However, in substitution mode the calculated adsorption energy (E$_{ads}$) of nitrogen (5.68 eV) directly on the doped phosphorous site showed that nitrogen is easily adsorbed on the un-doped carbon with an adsorption energy of 3.68 eV. In this way, the new N–C bonds are formed and replace the former P–C bonds which are elongated and significantly weakened after N adsorption (Fig. 12 (c)).

Zhang *et al.* [384] evaluated the electrochemical behavior of K-storage and Na-storage for high-N-content carbon nanosheets after introducing P to their structure by annealing with NaH$_2$PO$_4$. When used as an anode in KIBs without P doping, the nanosheets showed a higher specific capacity of 238 mAh/g at 0.1 A/g than the nanosheets that were doped with P, which had a specific capacity of 207 mAh/g at 0.1 A/g after 250 cycles. However, a higher Na-storage capacity of 246 mAh/g after 100 cycles at 0.1 A/g was obtained for P-doped nanosheets. Un-doped nanosheets delivered 175 mAh/g sodiation capacity under the same conditions. The Na$^+$ and K$^+$ ion diffusion coefficients measured by GITT demonstrated that the introduction of P to N-rich carbon nanosheets improves the Na$^+$ ion diffusion coefficient and lowers the K$^+$ ion diffusion coefficient [384].

Shanmugam *et al.* [385] described the interaction between the alkali-metal ions and doped graphene sheets to be mainly influenced of an ionic character. The adsorption energies of Li, Na, and K cations on B/N co-doped graphite sheets were found to be -2.66 eV, -1.88 eV, and -1.49 eV, respectively, and the adsorption of the metal ions increased by introducing defects into the graphite sheet [385]. It is notable that the doping and divacancy (DV) defect created by removing two carbon atoms was able to better adsorb alkali metals as compared with the defects that arose from structural arrangement of carbon atoms (stone-Wales (SW) defects) [386]. However, it has been reported that N-doping sites, not C defects, are the source of improved capacities in KIBs, whereas Na$^+$ ion storage is mediated by defects [387].

3.3. Biomass-derived carbon composites

As compared to graphite [388], hard carbon has severe voltage hysteresis proportional to the hydrogen content [121] and lower electronic conductivity arising from inhomogeneous potential/current distribution, which restricts its commercialization for application in batteries. Surface functional groups and/or heteroatoms (such as O, N, P and B) are one solution to by-pass these drawbacks, as described in Section 3.2. Here, we propose another solution to address the challenges of hard carbons for battery applications. To meet high-performance hard carbon anodes, conductive materials such as graphite and soft carbon or high-capacity materials such as metals and alloy nanoparticles are coated on the defective hard carbon to improve the connectivity between carbon atoms and enhance charge carrier transport, especially for the electrons. While direct mixing of higher conductive material and hard carbon can cause phase separation due to different densities, the partial embedment of metal and alloy nanoparticles, nitrides, oxides, and carbides, or ceramic composites, in the pores of hard carbons can be efficient. This process leads to extra space on the hard carbon surface, thereby buffering the volume expansion of the metals upon cation
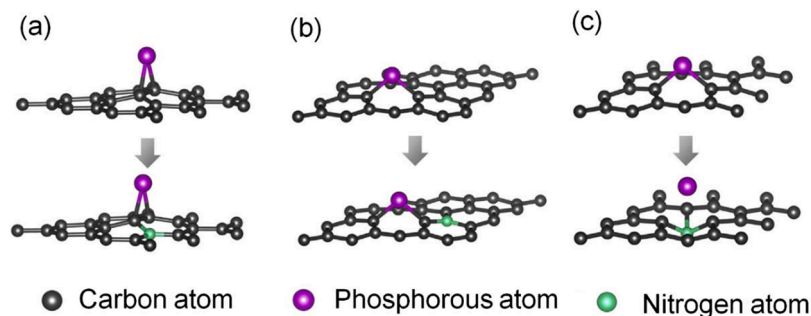
Fig. 12. Schematic illustrations of the orientation effect of the initially doped phosphorous on the later doped nitrogen; a) Outside mode, b) Inside mode, and c) Substitution mode [383]. Adopted from the mentioned reference after the required permission.

insertion and effectively hinders the aggregation of alloy particles. For example, Lian *et al.* [389] reported that the embedment of 26.7 wt.% Ni-doped CoS$_2$ nanoparticles (Ni$_{0.5}$Co$_{0.5}$)S$_2$ in a yeast-derived hard carbon improved the conductivity and led to a capacity of 600 mAh/g vs. Li$^+$/Li at 0.5 A/g after 450 cycles.

Pinning of Sn-Sb onto the surface of a hard carbon can help improve the carbon properties and allow it for an application as an anode material [390]. After Li insertion and the formation of multiple phases like Li$_3$Sb and Li$_x$Sn ($x < 4.4$), the separated phases can be restored to the original Sn-Sb alloys after Li removal. Filling the carbon micropores with Sn-Sb alloys may act as the "root" for outer, larger alloy particles that help to firmly root the nanoalloy particles on the surface of the hard carbon particles. Li *et al.* [390] pinned 29.8 wt.% nanosized Sn-Sb alloys onto a hard carbon surface. They reported that the surface areas of both alloy and carbon exposed to the electrolyte decreased. The specific surface area of hard carbon after Sn-Sb pinning reduced from 400 to 159 m^2/g, which could explain the improvement of the Coulombic efficiency after the first cycle. In the voltage profile, the Li-storage behavior showed four regions during the Li insertion process: (1) a slope ranging from 1.1 to 0.8 V, attributed to the decomposition reaction caused by a small amount of surface oxide on the nano-SnSb; (2) the plateau at 0.8 V related to the alloy reaction of Li with Sb; (3) the smooth slope from 0.7 to 0.2 V corresponding to multistep Li-Sn alloy reactions and the insertion reaction of Li into the non-graphitic carbon; and (4) a plateau from 0.1 to 0.0 V related mainly to the insertion of Li into the micropores of the hard carbon.

Yang *et al.* [391] reported a minimal agglomeration of Co$_3$O$_4$ nanoparticles during Li insertion by embedding as well as pinning them into the porous sugar-derived hard carbon. They recognized that the desquamating possibility of Co$_3$O$_4$ during cycling increased by pinning 29.7 wt.% Co$_3$O$_4$ into superficial pores without embedding them into deeper pores. Combining the advantages of a high lithium storage capacity of Co$_3$O$_4$ and the structural stability of a hard carbon enabled a composite anode material with specific capacity of 403 mAh/g after 35 cycles vs. Li$^+$/Li. The nanosized Co$_3$O$_4$ particles embedded in a hard carbon during Li insertion reduced first to the intermediate product α-CoO and subsequently to Co. The researchers suggested that the addition of nanosized Co$_3$O$_4$ particles encouraged the reversible Li$^+$ $\rightleftarrows$ LiO$_x$ reaction, which finally led to a higher initial Coulombic efficiency. Therefore, a simple combination of Co$_3$O$_4$ and a hard carbon was able to deliver a reversible capacity of 157 mAh/g after 10 cycles.

Guo *et al.* [392] suggest that a soft-carbon coating protects nano-sized Sn particles embedded in the mesopores of sugar-derived hard carbons against oxygen and improves the electrical conductivity of the final composite. They reported that the good cycling performance with a specific capacity of 400 mAh/g vs. Li$^+$/Li after 30 cycles resulted from the embedding of nano-Sn particles in the mesopores of carbon, which prevented its agglomeration during Li insertion. In addition, Sn nanoparticles significantly contribute to the high specific capacity by inducing the SEI film decomposition, and here especially of the Li

carbonates, at a voltage lower than 3 V which reduces ineffective side reactions and improves the Coulombic efficiency [392].

Fig. 13 illustrates the synthesis of TiN and TiC coated on hard carbon as undertaken by Cheng *et al.* [393]. In this study, nanocrystalline composites of TiN and TiC coated on the surface of hard carbon were synthesized by the reaction of cotton wool with TiCl$_4$, followed by firing at 1400°C in nitrogen and argon. The hard carbon (HC)-TiN composites with 15.15 wt.% TiN showed better performance than that of HC and the TiC-HC composite with 8.65 wt.% TiC. After 50 cycles, HC, TiN/HC, and TiC/HC composites had reversible capacities of 216 mAh/g, 242 mAh/g, and 187 mAh/g vs. Na$^+$/Na, respectively. According EIS measurements after 50 cycles, HC became more resistive (R$_{ct}$ = 296 Ω) than the TiN/HC composite (R$_{ct}$ = 105 Ω). The authors concluded that the higher electrochemical performance of the TiN/HC was related to an enhanced charge transfer kinetics imparted by the highly conductive TiN coated on the surface of the hard carbon. The weak cycling behavior of the TiC/HC composite originated from its low ability to participate in surface conversion reactions because of its larger crystallite size of 314 Å than that of TiN/hard carbon composite [393].

Jian *et al.* [394] reported mixing the hard carbon with 20 wt.% soft carbon could improve the hard carbon electrochemical performance as anode in KIBs. A ball-milled mixture of a hard carbon and a pyrolyzed soft carbon delivered higher rate capability and long-term cycling of ~200 mAh/g at 1C after 200 cycle compared to 160 mAh/g for pure hard carbon. The soft carbon with superior rate capability and electronic conductivity compared to the hard carbon was responsible for this improvement. Integrating a hard carbon with high long-term cycling performance and a soft carbon with great rate capability could provide an anode material with highly amenable performance in KIBs.

On the other hand, the volume expansion of active metals and alloys during electrochemical processes need to be reduced to improve the rate capability of a metal/graphite composite. Therefore, the preparation of a hard carbon-coated metal/graphite composite becomes necessary. The outside layer protects the electrolyte from the highly reactive inside particle e.g. of an oxide or an alloy. The electrolyte would be continuously decomposed in case the core particle allocatesfreshly formed surfaces to the electrolyte, as often recognized for materials undergoing large volume changes during cycling. For instance, hollow graphene-encapsulated Si particles of Nie *et al.* [395] delivered a remarkable rate capability of 890 mAh/g at 5 A/g and a good capacity retention over 200 cycles. Indeed, empty spaces in such a yolk–shell structure are capable to accommodate the volume expansion of Si during lithiation, reducing disintegration of Si particles and capacity fading.

Fig. 14 schematically illustrates the synthesis of the hard carbon-coated nano-Si/graphite composite [396] consisting of silicon nanoparticles (14.6 wt.%) coated with a hard carbon (39.6 wt.%) and graphite (45.8 wt.%) composite showed a reversible specific capacity of 879 mAh/g with an excellent stability of 738 mAh/g after 150 cycles at 0.12 A/g vs. Li$^+$/Li. The Si nanoparticles were closely connected to the graphite matrix owing to the hard carbon, which had considerable
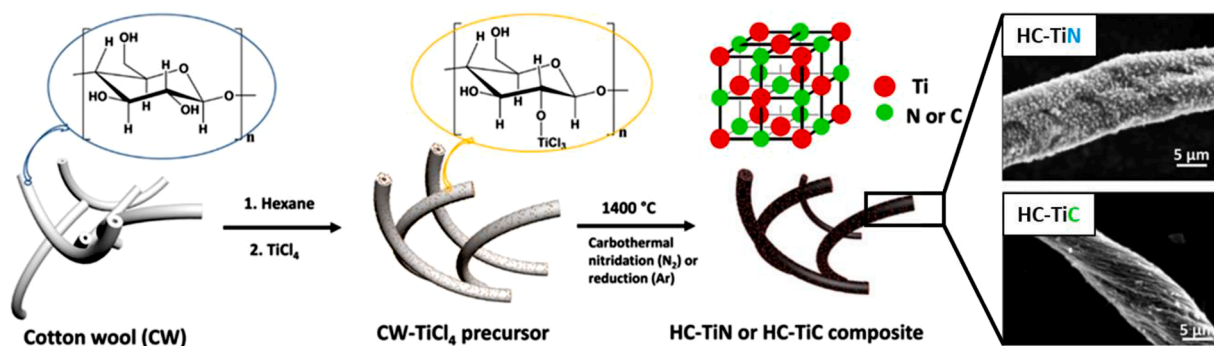
Fig. 13. Schematic illustration of the synthesis process to fabricate hard carbon (HC)-TiN and HC-TiC composites and the morphology of the preparation-related composites. Adapted from ref. [393] with permission.
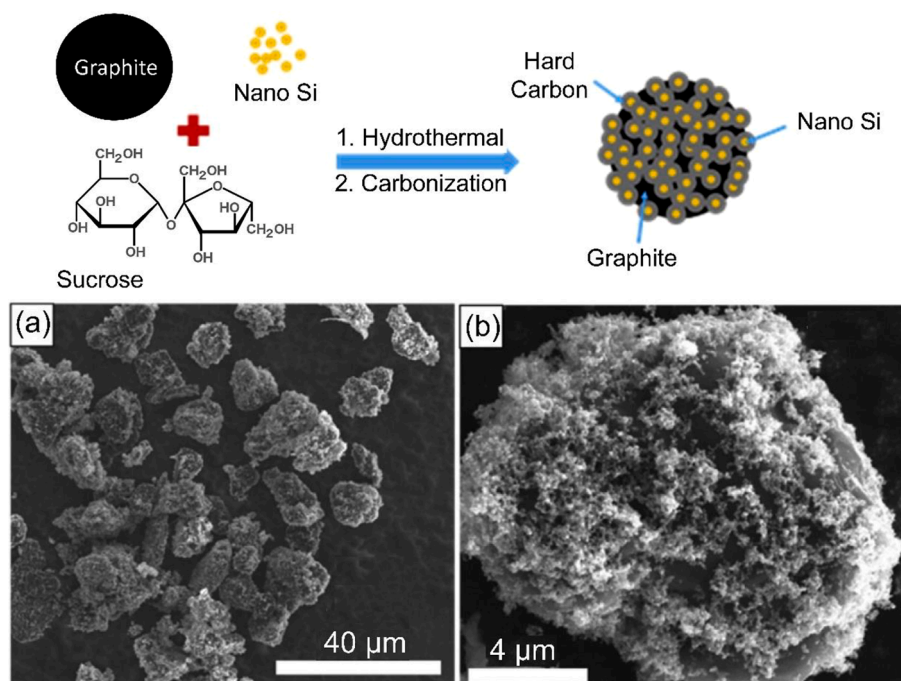
Fig. 14. Illustration of the synthesis of the interconnected hard carbon-coated nano-Si/graphite (HC-nSi/G), a and b) Low and high magnification SEM images showing the hierarchical structure of the HC-nSi/G composite. Adopted from [396] after the required permission.

influence on fast electron transport during charging and discharging. In addition, the hard carbon layer played a significant role in buffering the silicon volume changes, which can reach up to 400% during electrochemical reactions with Li [396].

Fig. 15 displays the voltage profiles of uncoated and amorphous-carbon-coated Sn nanoparticles. The uncoated Sn nanoparticles delivered a higher charge capacity of 950 mAh/g, but only for one cycle. Following this, the capacity faded rapidly to reach values below 100 mAh/g after 30 cycles. The carbon-coated Sn nanoparticles reached almost 800 mAh/g in the initial discharge cycle, but the specific capacity decreased between 600 to 700 mAh/g for the interval between the 5 and 50th cycles [397], related to Li^+/Li. These results indicated that the hard carbon acted as a proper "buffer- zone" for the volume change of Li_xSn.

To improve the rate capability and reversibility of Li intercalation/de-intercalation on the graphite surface, hard carbon materials were coated onto the graphite [398]. The porous and disordered hard carbon, with a different weight ratio to graphite, contributed most to the electrochemical performance of the final composite. The nitrogen physisorption results showed that the specific surface area of the obtained composites decreased gradually with increasing hard carbon content. It reported, the composite with 30 wt.% hard carbon exhibited a higher initial capacity of 374 mAh/g at 0.1 C than that of the composite with 10 wt.% hard carbon, which had a capacity of 365 mAh/g at the same current rate. However, after 100 cycles the specific capacity reversed, and the lower hard carbon content of the composite became advantageous, with a specific capacity of 349 mAh/g as compared with that of the composite with high hard carbon content, which was 340 mAh/g. At higher current rates, from 0.5 to 2C, the specific capacity of the composite with 10 wt.% hard carbon also exceeded that of the composite with higher hard carbon content. This improved capacity was probably due to superior conductivity of composite with lower hard carbon content. GITT experiments revealed an undesirably slow Li^+ ion diffusion in composite with 30 wt.% hard carbon because of the enhanced interface distance and reduced electrical conductivity. D_{Li}^+ values of 1.47 $\times 10^{-7}$ cm^2/s and 1.71 $\times 10^{-7}$ cm^2/s were calculated for carbon content of 30 wt.% and the 10 wt.%, respectively. By increasing the current rate to 3C, the charging capacities of the composite with higher hard carbon content improved, which confirms that high content is critical for reaching high-rate performance [398].
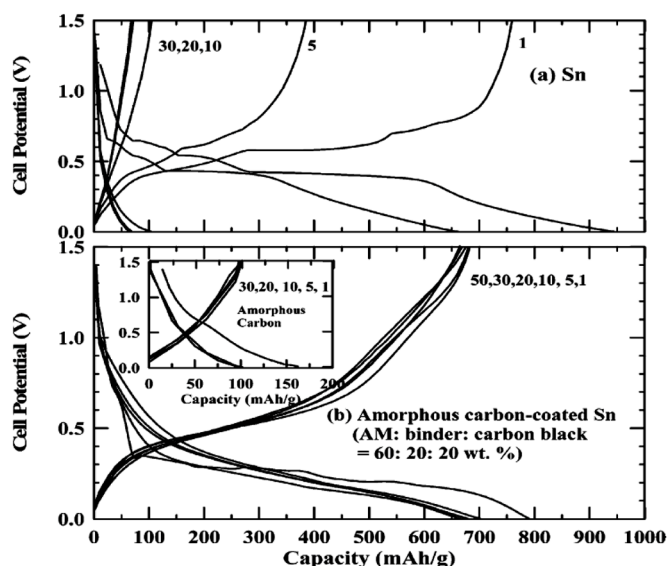
Fig. 15. Plots of a) the voltage profiles of the Sn nanoparticles, and b) with an amorphous carbon coating. Adopted from [397] after the required permission.

4. Electrochemical performance of biomass-derived carbon compared to graphite in lithium-, sodium-, and potassium-ion batteries

4.1. Cation intercalation into graphite and hard carbon

In LIBs, the intercalation of Li$^+$ into graphite involves one Li per six C atoms with the theoretical capacity of 372 mAh/g. However, in SIBs Na$^+$, because of its larger ionic radius of 102 vs. 76 pm of Li$^+$ and its high

ionization potential of 5.14 eV, only allows for the reversible formation of NaC$_{64}$ with a theoretical capacity of 35 mAh/g [399,400]. Li–C bonds, because of their non-negligible covalent portion, result in a more stable intercalation of Li into the graphite layers than that of Na into graphite [401]. The bonds between Na and graphite are weak. In addition, there are large changes of the stretched C–C bonds after Na insertion [402] into the graphite layer and the enthalpy of the formation of NaC$_8$ is positive [403]. As a result, the intercalation of Na$^+$ ions into the graphene layer is more difficult than for of Li$^+$ ions [404]. The intercalation of K$^+$ ions is even more difficult, given that their ionic radius is even larger than that of Na$^+$. Nevertheless, KC$_8$ is formed during potassiation by an exothermic process with a formation enthalpy of -27.5 kJ/mol [405], which is lower than even that associated with the formation of LiC$_6$, and causes a higher average intercalation voltage (See. Fig. 16 (a)).

For an efficient intercalation of Na$^+$ ions into the graphite structure, the interlayer distance must be modified. Two main strategies have been reported for applying graphite as the intercalation anode material in combination with the sodium battery chemistry. The first strategy involves a modified Hummers method typically used for graphene preparation. Here, the purified graphite was oxidized and was then treated with heat to obtain partially reduced graphite. As a result, the interlayer distance was enlarged to 4.3 Å and the final half-cell battery delivered the reversible capacity of 284 mAh/g at a current density of 0.02 A/g [409]. The second strategy is to co-intercalate a solvation shell along with the Na$^+$ ion. This strategy leads to the formation of a ternary graphite intercalation compound (t-GIC) with the general formula Na(solv)$_n$C$_x$ [15] (Fig. 16 (b I)). Thus, graphite undergoes a reversible Na-storage through the intercalation of solvated-Na$^+$, which results in a high amount of intercalated Na reaching the stoichiometry of about NaC$_{18–20}$ [410]. In the case of Li$^+$ ions, the intercalation of solvated Li$^+$ occurs for highly concentered propylene carbonate (PC), dimethyl sulfoxide (DMSO), and ether electrolytes. However, the t-GIC – especially in propylene carbonate-based electrolytes with low concentrations
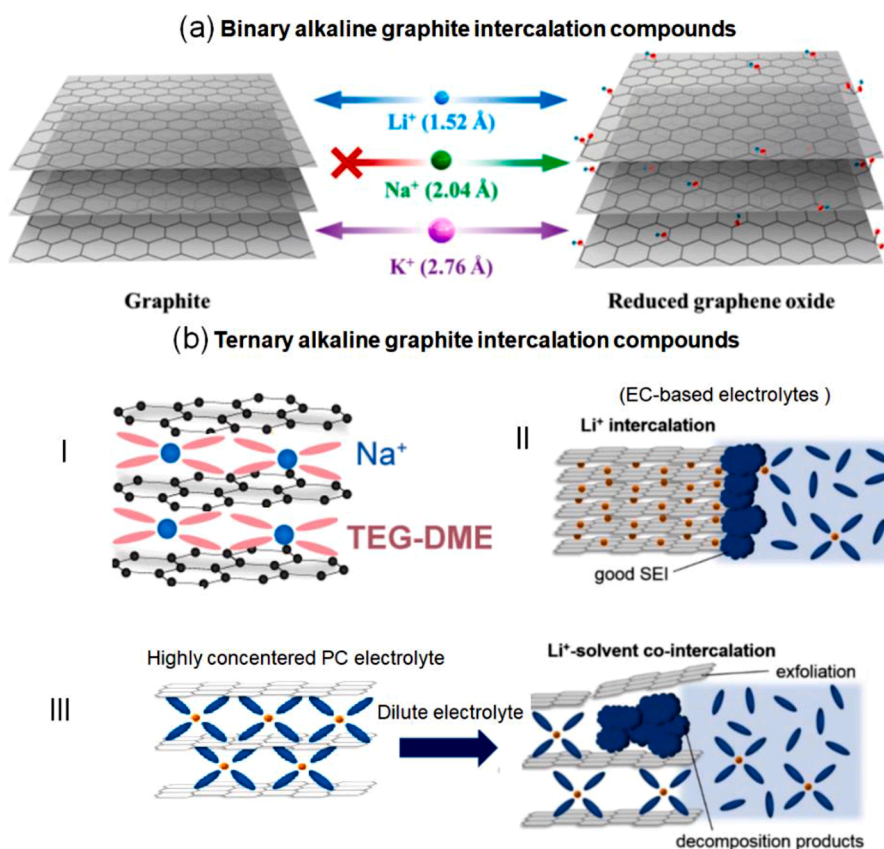
Fig. 16. a) Schematic of binary intercalation of Li, Na, and K ions into graphite and reduced graphene oxide (RGO). Li and K cations can intercalate into both graphite and RGO, while Na cations can only intercalate into RGO [406], b) Schematic of ternary intercalation of solvated Li and Na cations into graphite: (I) Intercalation of solvated Na$^+$ ions in Na half-cells with 1 M NaFSI/tetraglyme (TEGDME) electrolyte [407], (II) Li$^+$ ions intercalate reversible in EC-based electrolytes, whereas the intercalation of solvated Li$^+$ ions occurs for highly concentered PC, DMSO, and ether electrolytes. (III) Sometimes, in dilute electrolytes, the intercalation of solvated Li$^+$ ions is accompanied by the exfoliation of the graphene layers [408]. Adopted from mentioned references after the required permission.

of the conducting salt LiPF$_6$ – is instable against the oxidation and decomposition of co-intercalated solvent molecules. This instability eventually leads to the exfoliation of the graphite, with a negative effect on the cycling performance of LIBs (Fig. 16 (b II)) [408,411–413].

Organic solvents only poorly dissolve Na$^+$ ions compared with Li$^+$ ions, which leads to different amounts of solvent-Na$^+$ co-intercalated into graphite in various electrolytes [410,414]. Flexible linear ethers exhibit the most satisfactory electrochemical performance as electrolyte solvents for graphite [410]. Ethers with longer chain lengths trigger a higher Na-storage potential. In the case of well-solvated and, thereby, efficiently shielded Na$^+$ ions, longer ether chains weaken the unfavorable interaction between the Na intercalant and the graphite. As the Na intercalant is positively charged, longer chains of the ether solvate molecules attenuate the repulsion force among these positively charged intercalants. In addition, since the interlayer distance in graphite increases owing to the co-intercalation, the repulsive interaction between the negatively charged graphene decreases as well. Therefore, as the thermodynamic stability of the t-GICs increases by longer ether chains, the average co-intercalation voltage increases proportionally [415–417].

In addition to the formation of thermodynamically more stable discharging products, ether-based solvents with increasing chain length, such as diethylene glycol dimethyl ether (DEGDME), dimethoxyethane (DME), and tetraethylene glycol dimethyl ether (TEGDME) present another advantage. According to the this specified properties, a reversible capacity of ~150 mAh/g at a Na$^+$ ion storage potential of 0.6 V were reached for DEGDME as compared with the potential of 0.78 V for longer chain molecules of TEGDME [417]. Moreover, as the long chain ethers were inert against a reaction, only a thin SEI film of 3-7 nm was formed on the graphite surface as a result of minimal electrolyte component decomposition [407]. This layer only negligibly affected the Na$^+$-DEGDME diffusion to the graphite lattice. By contrast, carbonate-based electrolytes, in combination with sodium battery chemistry, were able to produce relatively thick SEI layers. Here, the high electrolyte decomposition acted more as an insulator and impeded the Na$^+$-solvent transport [15]. However, the oxidation of ether-based electrolytes at ~1 V restricts their application in hard carbon anodes. To optimize liquid electrolyte Na batteries, balance the anode charge/discharge to the cathode, and increase the usable voltage window, the co-intercalation voltage can be tuned up to 0.38 V by the conducting salt concentration [418]. Increasing salt concentration of the electrolytes leads to a substantial decrease in the free solvent activity, which shifts the co-intercalation voltage to lower values. Adjustment of the co-intercalation potential of SIB anodes enables high output voltages and allows the development of high-energy and high-power-density SIBs. In the work of Kim *et al.* [417], a SIB with a graphite anode delivered a reversible capacity of ≈150 mAh/g for 2500 cycles, and more than 75 mAh/g at 10 A/g, with ether-based electrolytes. The researchers showed that the choice of the conducting salt anions, such as NaPF$_6$, NaClO$_4$, and NaCF$_3$SO$_3$ dissolved in the ether-based electrolytes affect the electrochemical reactions only marginally [417].

Although non-modified graphite can hardly be used as an efficient electrode material for SIBs, the intercalation of K$^+$ ions into the graphite layers in ethylene carbonate (EC)/diethyl carbonate (DEC)-based electrolytes leads to a high theoretical capacity of 279 mAh/g, in spite of the larger ionic size of 138 pm of K$^+$ as compared with Na$^+$ [406]. The intercalated K$^+$ ions enlarge the interlayer distance of fresh graphite from 3.35 Å to 5.35 Å, and the volume expansion after full K intercalation is calculated to be almost six times larger in contrast to the Li intercalation. This K-induced volume expansion/contraction of graphite during intercalation/de-intercalation is reversible and without a negative effect on the cycling stability [405]. K$^+$ ion intercalation into graphite contrasts with that of the intercalation of alloys and conversion electrode materials, which normally leads to fast electrode deactivation and an irreversible capacity drop [419,420]. In addition, some studies have proposed the intercalation of various K(solv)$_y$C species into

graphite with DEGDME and TEGDME-based electrolytes to form t-GIC [421,422]. Solvated K$^+$ ions are smaller than solvated-Na$^+$ and -Li$^+$ owing to the weaker Lewis acidity of K$^+$ ions in common solvents. This property, in addition to the lower desolvation energy of K$^+$ ions, provides higher transport numbers of solvated K$^+$ ions and fast diffusion kinetics across the electrolyte/electrode interface [423].

In summary, the alkali cation-solvent molecule complex in the graphite host should be chemically stable and should have a high LUMO level to ensure the reversible co-intercalation. When the complex is instable, it can decompose, and gas evolution can trigger the exfoliation of graphite upon co-intercalation (Fig. 16 (b III)). A straightforward strategy to enhance the intercalation efficiency of Na$^+$ ions is to use a hard carbon in the anode composite. Hard carbons have a non-ordered and defective structure with interlayer distances of about 3.8 Å, large enough to form intercalation compounds. NaC$_8$ was reported to deliver a theoretical capacity of 279 mAh/ g at low voltages of about 0 V [424]. NaC$_6$ was reached when the equilibrium interplanar distance was increased to about 4.5 Å [425]. No co-intercalation plateau was detected in the voltage range of 0.6-0.8 V in the voltage profile of hard carbon. This observation shows that Na intercalates into graphite to form a binary graphite intercalation compound regardless of the type of electrolyte [426]. To evaluate the effect of the electrolyte on the reversible Na$^+$ ion storage capacity of hard carbon electrodes, electrochemical cycling was performed in carbonate-based electrolyte (EC, PC, and butylene carbonate (BC)) solutions containing NaClO$_4$ (see Fig. 17). In the potentiogram, a slope from 1.2 to 0.1 V and a plateau region between 0.1 and 0 V were observed during the initial sodiation. During de-sodiation, the presence of plateau and slope regions in this voltage range suggesting that hard carbons reversibly insert sodium when organic carbonates as electrolytes are used. As seen in Fig. 17 (b), the hard carbon electrode in the BC electrolyte showed a reversible capacity of ≥230 mAh/g in the early cycles. However, serious degradation began after the 20th cycle. In contrast with the BC solution, the hard carbon electrode retained a steady capacity in the EC and PC solutions [427]. By considering the high melting point of EC (~37°C), a PC-containing electrolyte is the better choice for SIBs. The SEI formed on the hard carbon after cycling represents a rough and non-uniform layer with a thickness of approximately 30 nm. As commonly accepted, carbonate-based electrolytes are thermodynamically instable at the standard potential of Na, and some decomposition of the solvents occur. For long-term cycling an interfacial passivation is required. After one month, the discharge capacity still reached approximately 80% which also implied a low self-discharge. The surface film worked as a passivation film and protected the Na-intercalated hard carbon anode from chemical reaction with the electrolyte [427].

Ponrouch *et al.* [428] reported that an additive-free and EC:PC-based electrolyte with both NaClO$_4$ and NaPF$_6$ as conducting salts was able to improve the reversible capacity of hard carbons to ≥300 mAh/g at C/10 after 120 cycles. Gebrekidan *et al.* [429] described the solubility of NaPF$_6$ in various single solvents decreased in order of EC (1.4m) > PC (1.0 m) > DEC (0.8m) > DMC (0.6m), which implies that NaPF$_6$ is coordinated more strongly by EC followed by PC in the electrolytes. In addition, the lower rate of exothermic heat of NaPF$_6$, NaClO$_4$, and NaTFSI released for the electrolytes contain EC/PC compared to EC/DEC and EC/DMC in contact with sodiated hard carbon, indicated that this mixture is suitable as a safer solvent for SIBs.

Galvanostatic discharge/charge cycles for graphite and hard carbon show different voltage profiles consistent with their different structures. Sites that Li can access easily, which are either electronically or geometrically favored, generally contribute to a sloping profile with large hysteresis for the hard carbon. By contrast, graphite is characterized by many equivalent sites for the lithiation. Their contributions yield the potential plateau. The sloping discharge profile of a disordered carbon with many inequivalent Li coordination sites shows that most of the capacity was accumulated at a higher voltage range than that for a commercial, ordered carbon. Indeed, randomly aligned graphitic layers
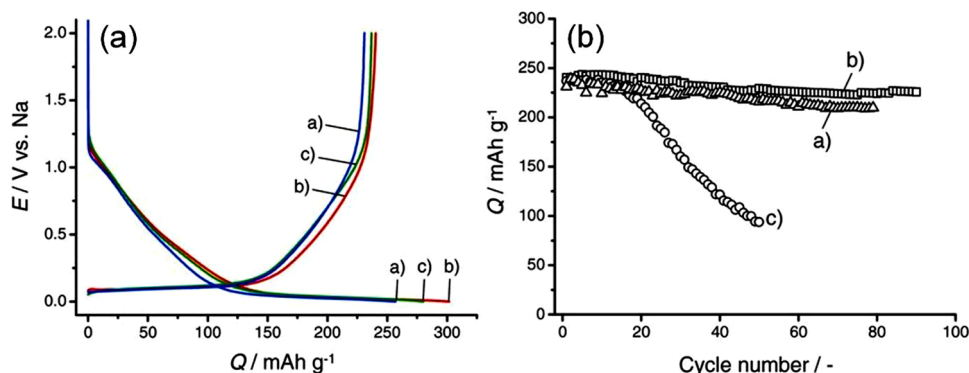
Fig. 17. Initial cycle and variation in reversible capacities for hard carbon electrodes in a) EC, b) PC, and c) BC solution containing 1 mol/l $NaClO_4$ tested at 0.025 A/g in beaker-type cells. Adopted from [427] with permission.

facilitated faster metal intercalation as compared with the ordered graphitic layers in commercial graphite [207]. Because of this structural feature, hard carbons in KIBs perform well acording to the rate capability experiments [430]. However, to optimize the battery performance, the metal intercalation corresponding to the flat voltage plateau needs to be extended, while the sloping region should be shortened [431].

A voltage-capacity curve of a graphite electrode in the voltage range below 0.3 V showed several transition stages during the first lithiation. The potentials for potassiation and lithiation into graphite layer were reported to be around 0.24 V and 0.1 V vs. Li^+/Li, respectively [432, 433]. The intercalation of Li into the graphite structure can be classified into the intercalation stages LiC_{72}, LiC_{36}, LiC_{27}, LiC_{18}, LiC_{12}, and LiC_6 [434–436]. The optical spectrum changes from black for graphite via blue for LiC_{18} to brown for LiC_{12} to finally reach a golden color for LiC_6 that points to significant changes in the electronic structure according to the lithiation [437]. Such influence manifests in the partial filling of the π^* states, which are unoccupied in untreated graphite. The intercalation products LiC_{12} and LiC_6 show a metallic character owing to the partially filled π^* states which is reflected in increasing contributions to the respective density of states the more Li intercalates [437]. Additionally, phonon dispersion and electronic band structure calculations suggest a fast kinetics of K^+ at the expense of a lower capacity [438] .

In contrast with graphite, neither staging nor color changes were reported for hard carbon electrodes during K^+ or Li^+ intercalation. In this case, hard carbons have shown to benefit from the larger interplanar spacing compared to graphite, which resulted in a relatively constant distance during the potassiation or lithiation process [436].

Transition stages were also observed during the potassiation process of graphite as displayed in Fig. 18 (a) [406,433,439]. To elucidate the electrochemical potassium-storage mechanism in graphite at room temperature, *ex situ* XRD was carried out for selected states of charge in

the first-cycle at C/10 (Fig. 18 (b)). By dropping the voltage from 0.3 V to 0.01 V, the sequential formation of KC_{36}, KC_{24}, and KC_8 was described [433]. However, Luo *et al.* [406] calculated a staging scenario for the electrochemical intercalation of K^+ ions following the reaction path $KC_{24} \rightarrow KC_{16} \rightarrow KC_8$ via DFT. The color of graphite changed from black in the initial stage to gold after intercalation of K^+ ions at least until KC_8 (Fig. 18 (c) related to the gradual expansion of the graphitic interlayers and the changes in the electronic structure due to electron doping. The calculated electronic density of states (DOS) for graphite and KC_8 indicated an upshift of the Fermi level which may cause the change in the optical spectrum.

The golden colored KC_8 as the final product of potassiation exhibited a plateau above the plating potential of K metal [433]. This property is important as it may avoid or at least relieve dendrite formation and increases the safety of an application. In spite of providing large specific capacities at low current rates, graphite in KIB compared to LIB anodes suffered from fast fading of capacity because of its dramatic volume expansion, especially at high rates. Like other compounds with large volume changes, graphite shows partial structure decomposition during potassiation and depotassiation. Further, the specific capacity dropped significantly from 263 mAh/g at C/10 to 80 mAh/g at 1C [433], suggesting slower K^+ ion intercalation kinetics compared to the Li^+ ions [406]. The large voltage hysteresis of 0.14 V between the charge and discharge curves justified the poor rate capability [433]. However, selecting appropriate binders to ensure a uniform coating layer and a reduced formation of a SEI film could help to decrease the stress induced by the large volume expansion of graphite during potassiation. These modifications can then repel the rapid capacity drop. According to Zhao *et al.* [440], the use of EC:PC as electrolyte and Na alginate as a binder increased the efficiency of the electrochemical performance of graphite as a KIB anode inferred from higher Coulombic efficiency and better cycling stability.
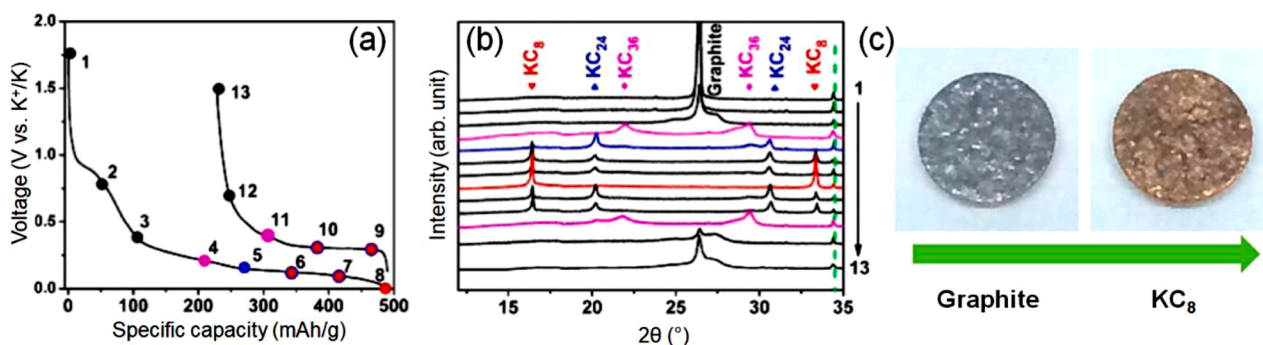
Fig. 18. a) Galvanostatic potassiation/depotassiation at C/10 with the points 1-13, where b) Reaction-representative ex situ XRD measurements were performed. Adapted from ref. [433] with permission. c) Black-grayish polycrystalline graphite platelet in the initial state and after reaching the final potassiation state KC_8. Adapted from ref. [406] with permission.

In situ Raman spectroscopy has provided detailed insights into the K$^+$ ion insertion mechanism into few layered graphene [441]. As illustrated in Fig. 19 (a-c), the G peaks for the charged (G$_c$) and the discharged (G$_{uc}$) state appeared in a voltage window between 0.37 to 0.2 V. The G$_c$ peak shifted to lower wave numbers as the voltage decreased from 0.22 V to 0.01 V (Fig. 19 (b,c)). This shift can be inferred to be the result of charge density on layers close to the intercalants. From 0.24 V to 0.15 V, the intensity of the G$_c$ peak increased as the G$_{uc}$ and 2D peaks decreased, whereas all peaks become red-shifted. From 0.15 V to 0.01 V, the G peak in the Raman spectra changed from being symmetrical to being asymmetrical (Fig. 19 (b)). However, the G$_{uc}$ peak was assigned to the graphene layers that were not adjacent to the K$^+$ ions or where K$^+$ ions are homogeneously distributed without localized charges, as related to the increase of the G$_{uc}$ peak in the depotassiated state (e.g. at 2 V) in the absence of the G$_c$ signal [441]. It should be noted, that even more potassiation stages are observed with few layered graphene compared to graphite. Raman spectroscopy enables much deeper understanding as shown for the results on the alkali intercalation into hard carbons. Here, differences between Li on the one side and Na and K on the other side were demonstrated and limitations uncovered. These investigations supported by respective band structure and phonon dispersion calculations allow for recommendations towards the design of the hard carbon pores. This procedure was identified to be crucial to minimize diffusion barriers and to improve the performance of KIBs [438].

4.2. SEI formation on graphite and hard carbon in LIBs, SIBs and KIBs

The onset potential for the decomposition of electrolytes and the formation of a passive layer composed of inorganic and organic constituents on carbons are different. However, no standard starting potential for the formation of the SEI on graphite and disordered carbons exists. It varies and depends on the composition of electrolyte, the additives used in the electrolyte, the sweep rates, physical properties of the carbon anode such as particle size, pore size, and surface chemical composition (adsorbed species, heteroatoms) [442]. The formation, thickness and, in general, chemical and physical properties of the SEI formed on graphite depend on the ratio of basal planes to edge planes. The edge planes provide more susceptible sites for the decomposition of the electrolyte, but also more access points for metal intercalation than the basal planes [436,443,444].

The SEI formation on graphite in KIBs commences at 0.6 V and its formation is expected to be more significant at 0.15 V [445]. While various voltages, including 2 V [446], 1.7 V [447], and 1 V [448], have been reported for SEI formation on graphite and related Li consumption. The most widely accepted and proven SEI formation voltage for graphite is 0.8 V in the first cycle [449]. However, the formation of thick protective SEI on graphite usually prevents further electrolyte degradation at voltages <0.8V vs. Li$^+$/Li. It is favorable to stop the SEI formation before the start of the Li$^+$ ion intercalation at about <0.3 V. Unfortunately, this demand is often out of reach for disordered (hard) carbons because of its earlier intercalation at about 1.5 V vs. Li$^+$/Li [443,446]. The reduction peak appearing at ~1.1 V was ascribed to the irreversible reaction of the electrolyte with surface functional groups [450]. In general, at higher voltages (~0.8 V vs. Li$^+$/Li) the formed SEI was mainly composed of organic polymeric compounds with low inorganic content. At low voltages the SEI was transformed into a more compact structure with inorganic salts as the main constituents neighboring the active material arranged in the form of an inner layer [451], however, this layer on sodiated hard carbon is nonhomogeneous and less compact in nature compared to that in LIBs. In addition, the electrolyte
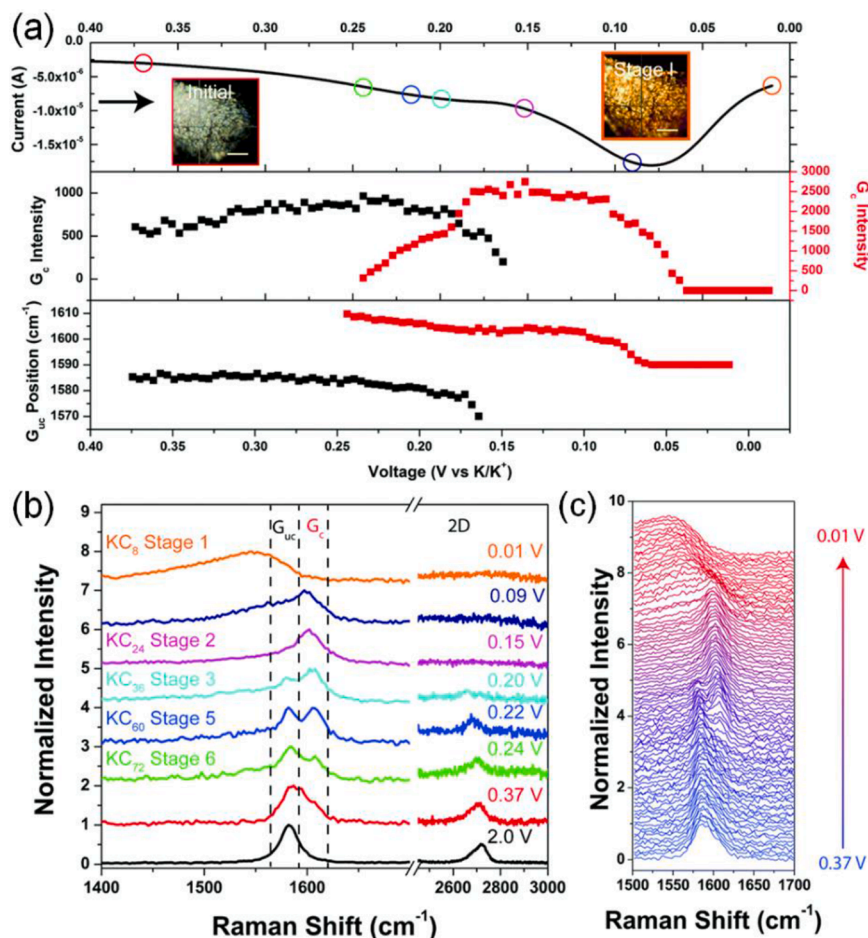
Fig. 19. a) Linear sweep voltammogram of few layered graphene during Raman spectroscopy experiments with optical microscope images of initial, non-potassiated state and the final stage 1 corresponding to KC$_8$ (top), intensity development according to partially localized charge due to K$^+$ ion intercalation (G$_c$, middle) and the shift of the position of the G band where charges are equally distributed (G$_{uc}$, bottom). b) Raman spectra for selected states of charge with the respective K$^+$ ion intercalation stages. c) Waterfall plot of all Raman spectra taken between 0.37 V and 0.01 V. Adapted from ref. [441] with permission of the Royal Society of Chemistry.

decomposed further and established an outer SEI layer of mainly organic components [451,452].

The mainly organic part of the SEI on hard carbons in LIB is constituted by lithium organic compounds and others [443,444]. The main inorganic compounds (A_2CO_3 and A_2O) of SEI are Li_2CO_3 and Li_2O which are more enriched in the presence of EC [453]. The composition of the SEI can be also modified by surface functionalization. Ganesh *et al.* [454] reported on a H-terminated surface that postponed the reduction of the electrolytes such as EC or DMC, while an O/OH terminated surface EC reduced quickly. Oxygen-terminated sites allow for a better charge transfer than H-terminated sites and hence led to electrolyte reduction. Organic SEI compounds in KIBs are similar to LIB systems [445]. Wang *et al.* [455] revealed that $(CH_2OCO_2K)_2$, $C_2H_5OCO_2K$, KF and K_2CO_3 are the dominant components of the SEI layers in KFSI- and KPF_6-based electrolytes. They observed a higher amount of K_2CO_3 is formed in KPF_6-based electrolytes compared to KFSI-based electrolytes. However, the SEI in the KFSI-based electrolyte is much more stable, compact and thinner than in the KPF_6-based electrolyte. All these features, together, ensure good stability and high reversibility in the KFSI-based electrolyte. A study of the SEI on carbon in Na half-cells showed a lower dissolution energy of Na with respect to Li and the higher redox potential of Na^+ vs. Li^+ (~ 0.33V). A reduction of the electrolyte degradation at the surface of the sodiated anodes, affect SEI behavior [456]. Organic SEI components in SIBs, are mainly composed of sodium alkyl carbonates ($ROCO_3Na$), sodium alkoxides (RONa), ethylene oxide oligomers (such as polyethylene oxide, PEO, $(CH_2\text{-}CH_2\text{-}O)_n$), semi-carbonates and sodium double alkyl carbonates ($NaO_2CO\text{-}C_2H_4\text{-}OCO_2Na$). The SEI in SIBs incorporates higher amounts of C=O or C-O containing species than C-C/C-H as found in LIBs [457].

The higher solubility of the organic compounds formed on sodiated hard carbons compared to lithiated hard carbons, caused a conversion of $(CH_2OCO_2Na)_2$ into Na_2CO_3 [457]. The use of fluoroethylene carbonate (FEC) together with NaTFSI conducts the formation of Na_2CO_3 and NaF, with poor electrochemical performances. However, the formation of $NaO_2CO\text{-}C_2H_4\text{-}OCO_2Na$ and NaF in the mixture of $NaPF_6$ and FEC, showed better electrochemical performances. The presence of a rather insoluble species such as NaF can play an important role in stabilizing the SEI and in limiting solubility issues related to other compounds (such as $NaO_2CO\text{-}C_2H_4\text{-}OCO_2Na$ here) and eventually improve the capacity retention upon cycling [456]. The organic content of the SEI on sodiated hard carbons decreases based on the Na salts in the order: $NaPF_6 >$ $NaClO_4 > NaTFSI > NaFTFSI > NaFSI$ [457]. However, the SEI formed during sodiation was composed mainly of inorganic compounds such as Na_2O, Na_2OH, Na_2F, Na_2Cl, Na_3O, Na_3F_2, and Na_2CO_3 [427]. Na^+ ion diffusion through the hard carbon SEI is dominated by inorganic constituents, such as Na_2CO_3 and NaF. iIn the case of the SIB a higher diffusion energy is required e.g. compared to Li^+ ions which just diffuse through an mainly organic layer with some Li_2CO_3 and LiF [458]. Higher amount of NaF was observed for NaFSI and NaFTFSI compared to $NaPF_6$- and NaTFSI-containing electrolytes [457].

The composition of the SEI layer can be varied based on the used electrolyte. Xiao *et al.* [459] reported about the intercalation of Na^+ ions into hard carbons with TEGDME and a carbonate electrolyte. The charge–discharge curves were recorded with an almost similar profile for both electrolytes. However, hard carbons showed better cycling stability in TEGDME than in the carbonate electrolyte, particularly at high current densities. This difference was attributed to the different SEI layer composition on the hard carbon surface, which affected the Na^+ ions transfer kinetics. Because of the weak decomposition of TEGDME on hard carbons, a thin SEI layer composed of organic compounds with C-O and O=C-O bonds was formed, which quickly stabilized around at 0.5 V. However, after cycling in the carbonate electrolyte the surface ofthe hard carbon was covered by a thick SEI layer (mainly composed of inorganic compounds like Na_2CO_3) and did not stabilize until or even below 0.2 V.

To compare the electrochemical performance of a sucrose-derived

hard carbon in EC:DEC and DEGDME electrolytes, it was tested in 0.8 M $NaPF_6$/EC:DEC (1:1 v/v) and 0.8 M $NaPF_6$/DEGDME. A higher irreversible capacity was observed for the EC:DEC solvent during the first cycle that supported a higher decomposition of the electrolyte components to form the SEI on the hard carbon surface. Additionally, a larger voltage gap between cathodic and anodic peaks of 0.14 V for EC:DEC compared to 0.06 V for DEGDME indicated a slower Na^+ ion transport for the EC:DEC system. With SEM, a thin SEI layer on a smooth and dense hard carbon surface was recognized for DEGDME. This observation once again verified the efficiency of the SEI layer to protect DEGDME against further decomposition or the hard carbon anode from reactions with the electrolyte. As the main contribution of the SEI was identified in a high rate capability due to a fast Na^+ ion transport across the layer [460]. The same results were observed by Kim *et al.* for a natural graphite anode [461]. They showed that ether-based electrolytes with suppressed electrolyte decomposition only form a negligible SEI film on the graphite surface. This thin SEI was beneficial for the transport of Na^+-solvent complexes which were found to co-intercalate into the graphite lattice. Besides DEGDME, TEGDME and DME also showed a similar behavior. The chemical compositions of the SEI formed with EC:DEC and DEGDME electrolytes were analyzed by XPS. The O 1s spectra showed the existence of Na alkoxide and Na_2CO_3/Na_2CO_2R, corresponding to the mono-, bi- and tri-oxygenated environments of carbon at 533.3 eV, 531.8 eV and 536.5 eV, respectively, for hard carbons cycled in DEGDME and EC:DEC. The F1s spectra displayed two signal contributions at 684.4 eV (Na-F) and 688.4 eV (P-F) related to the decomposition of residual $NaPF_6$. Depth profiling of the sample with Ar^+ ion sputtering led to a decrease in the O1s spectrum intensity, which was referred to C-O here, and an increase of the intensity in F1s spectrum, according to Na–F contributions. After sputtering times of >1 min., no distinct change was recorded in the spectra. The DEGDME electrolyte-formed SEI was therefore quite thin and mainly consisted of NaF in the interior. However, sputtering of the SEI formed with the EC:DEC electrolyte showed a similar change in the spectra. At longer sputtering, a gradual change in the O1s spectrum intensity (referring to O-C(=O)O here) and a quick decrease in the Na–F contributions were found. This observation pointed to a thick SEI with inhomogeneously distributed organic and inorganic constituents [462].

Fondard *et al.* [399] showed the best electrochemical performances on hard carbon electrodes with an electrolyte of $NaPF_6$ dissolved in an EC:DMC electrolyte at addition of 3% FEC. The enhanced performance was attributed to the formation of a SEI composed of $NaO_2CO\text{-}C_2H_4\text{-}O\text{-}CO_2Na$ and NaF. On the other hand, a low NaF or a high Na_2CO_3 content result in poorer electrochemical performances. Komaba *et al.* [463] suggested that the reversible capacity and the retention for the hard carbon anodes could be improved by adding a small amount of FEC to the PC solvent. Although, the FEC additive enables a reduction at higher potential (~0.7 V) and a formation of a crack-free SEI on hard carbons to suppress the continuous reduction of the electrolyte on anode surface in SIBs. Nevertheless, the specific capacity and cyclability of the graphite become worse by FEC addition to the electrolyte for KIBs [464]. FEC stimulates the electrolyte decomposition at potentials below 2 V vs. K^+/K and results in larger electrode polarization and fast capacity fading. When vinylene carbonate (VC) is added instead, the potential reduction of the electrolyte shifts to lower values and subsequently the chemistry of the SEI layer changes. Katorova *et al.* [465] showed that the SEI is mainly composed of inorganic components in carbonate-based electrolytes, whereas the VC additive changed the composition of the SEI to more organic compounds. These organic compounds improved the mechanical properties of the SEI and made it more resistant toward fracturing during the hard carbon volume changes in potassiation and depotassiation. On the other hand, the VC additive negatively affected the performance of SIBs as recognized by a decreasing discharge capacity [466]. Yverick *et al.* [467] also improved the hard carbon anode performance in Na half-cells by manipulating the SEI formation at high charging rate. The hard carbon with thin SEI formed by ether-based

electrolytes at 100 A/g exhibited the lowest impedance and delivered almost twice the capacity of the electrode with the SEI formed at 1 A/g.

4.3. Role of texture and surface groups in biomass-derived anodes in LIBs

Various voltage profiles for different types of carbonaceous materials have been reported, which represent individual mechanisms that depend on the preparation temperature. Carbon synthesized at low temperatures <1000°C contains a large number of micropores that interestingly can contribute marginally to the low voltage plateau capacity [104,250]. Higher first lithiation capacity, in addition to irreversible capacity loss as compared with carbon synthesized at higher temperature, is commonly observed in the charge/discharge curve. However, by increasing the carbonization temperature and decreasing the micropore volume, and with less Li uptake in the pores, the specific capacity as well as irreversible capacity loss decrease but exceed longer capacity retention [468].

The reported specific capacities for graphite were lower compared to the hard carbons. By contrast, the capacity of the hard carbon faded faster than that of graphite in the lithiation process. This additional capacity is related to occupation of a second Li covalently bond to the nearest neighbor sites of a Li in the intercalated carbon and also the existence of different Li-storage sites that enable the plating of non-dendritic Li metal on the external surface of graphite. Finally, the accommodation of Li in the vicinity of defects and micropores out of reach of the electrolyte is also a potential reason [469]. However, based on the treatment temperature, various pore shapes such as open, partially closed, and closed nanopores can be formed, which affect the adsorption and desorption kinetic of Li.

It is understood that the smaller particles with higher surface area cause larger SEI formation, higher irreversible Li loss during SEI formation, and higher exfoliation of the graphite as well. Therefore, using a low specific surface area of less than 40 m²/g, or even less than 10 m²/g to suppress side reactions at charging and discharging is preferable [461]. The high number of micropores in biomass-derived hard carbon inhibits an optimized transport pathway for the electrolyte and eventually causes the reported dramatic drops in capacity, already after a few cycles [470]. The slow electrolyte transport in a microporous system is the reason why micropores in carbon materials are unable to yield good rate performance, especially at high current density. By contrast, the existence of macropores is favorable for high rate performance. Zhang et al. [249] compared porous hard carbons derived from pine needles, with a high specific surface area of 3000 m²/g but few macroporous channels with rice straws that had almost the same surface area but more macroporous channels. They found that the porous carbon derived from rice straws had distinctly higher reversible capacity at high rates. This behavior can be explained by the fact that macropores quickly drain the electrolyte reservoir and enable fast spread throughout the pore system to reach not only the mesopores but even the micropores. Cheng

et al. [471] showed for air oxidized biomass, that the defects or micropores on the basal plane of the carbon material were converted to large multi-channel pores and holes which helped to increase the lithiation capacity over 500 mAh/g of capacity.

Fig. 20 (a) displays the first five cyclic voltammogram (CV) curves for porous carbon fibers, with a large pore size distribution from 0.3 nm to 40 nm. The electrolyte decomposition was recognized at 0.72 V vs. Li⁺/Li as an additional cathodic current peak in the first cycle at a scan rate of 0.1 mV/s in a voltage window of 0.01–3.0 V vs. Li⁺/Li. In addition, the reduction current in the first cycle below 1.8 V vs. Li⁺/Li reaches a higher value as compared with further cycles. This extra current was inferred to represent the formation of the SEI film, which finally resulted in the higher discharge capacity of the first cycle than that of the second cycle [203]. Here, the anode suffered from an irreversible capacity of about 39%. This behavior was attributed to the presence of ~7 % oxygen-containing surface groups. High-resolution XPS revealed hydroxyl, carbonyl (or ether), as well as carboxyl (or ester) groups with binding energies of 286.2, 287.2, and 288.9 eV respectively in the C1s spectrum. The capacitance of the sample was also calculated based on the integral area of the redox processes and for different scan rates ranging from 0.1 to 10 mV/s (see Fig. 20 (b)). Almost 90% of the charge storage at all scan rates resulted in a surface-related capacitance owing to the non-faradaic double layer. These results underline that the synthesized porous samples could be promising anode materials for high-power energy storage devices [203].

According to Mabuchi et al. [473], micropores formed between graphene layers in disordered carbons caused an excess capacity. They inhibited Li insertion, and induced an extensive passivation layer on the surface of the pores. This effect resulted in a pore-size reduction or even clogging of the pores. A decrease of diffusion coefficients were determined, and eventually Li was captured in the pores and was unavailable for further cycling [474]. Stephan et al. [19] reported that a high surface area can adversely affect the reversible capacity. Electrochemical measurements on ZnCl₂-activated hard carbon from banana fibers with a specific surface area of 1285 m²/g revealed a significant specific capacity of 3123 mAh/g vs. Li⁺/Li in the first cycle. However, it exhibited high irreversible capacities of up to 88% for the subsequent cycle. These researchers attributed these Coulombic inefficiencies to huge surface passivation and the clogging of pores and cavities.

Beyond the influence of porosity, surface functional groups can significantly influence the intercalation reversibility of hard carbon, if is not treated at inert or at least dry conditions after finishing the pyrolysis [436,444,475]. To decrease irreversible capacity, a surface-modified hard carbon was prepared by reducing the water content at temperatures between 50°C to 180°C before pyrolysis. Kikuchi et al. [476] also confirmed an improved cyclability of a hard carbon once the surface hydroxyl groups and the adsorbed water on the surface were removed during heating at 980°C in vacuum. However, Xie et al. [477] claimed that introduction of oxygen functional groups on sucrose-derived carbon
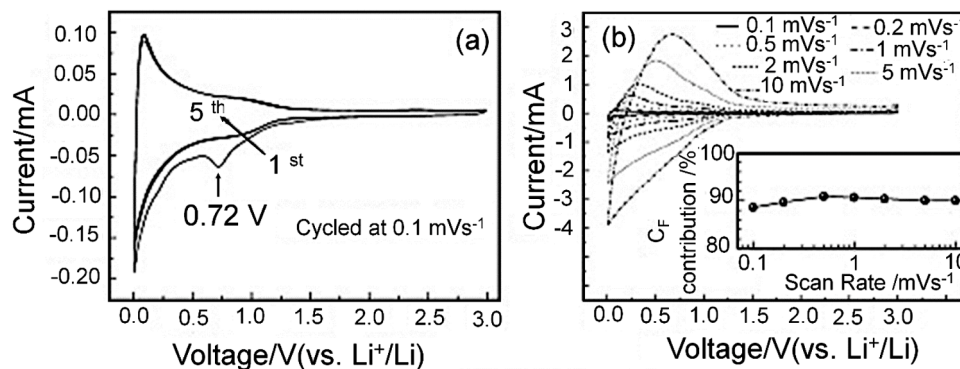
Fig. 20. a) The first five CV curves cycled at 0.1 mV/s, b) stable CV curves cycled at various scan rates from 0.1 to 10 mV/s. Adopted from [472] after the required permission.

via oxygen-plasma treatment stabilized the solid electrolyte interface. The oxygen plasma could decrease active carbon sites due to its strong oxidizing ability.

Another alternative to a post-pyrolysis treatment was established with a thin carbonaceous layer prepared by chemical vapor deposition from ethylene after the carbonization but before any exposure to ambient conditions. Electrochemical tests showed a decrease in the irreversible capacity with >150 mAh/g before the layer deposition to less than 70 mAh/g afterwards [478]. With the chemical vapor deposition of a carbon layer from propene on a carbon cloth surface, Béguin et al. [479] initialized an 1.5-fold drop in the irreversible capacity attributed to a decrease in the amount of active sites involved in parasitic reactions or SEI formation. Additionally, the active surface area was reduced by such treatment, and the pyrolytic carbon layer offered a significantly more homogeneous surface with lower defect concentration. Indeed, a protected pyrolytic carbon layer on hard carbons avoided the diffusion of Li^+ ions into the active sites of the hard carbon in a similar way [480].

Slow heating rate, high gas flow rate and the continuous removal of the released gases are further effective ways to decrease the specific and active surface area of hard carbons. A longer residence time of the hard carbon with the pyrolysis gas products, especially CO_2 but others like O_2 as well, causes an extensive carbon burnout resulting in a larger specific surface area and the formation of micropores, which all contribute to irreversible capacity losses due to the high amount of generated active sites [62,481].

Some other good examples are shown for the hydrogen-to-carbon ratio with typical values of 0.05-0.30 in pyrolytic carbons. The reversible capacities of hydrogen-containing carbons, heated at T < 800°C were directly correlated with their hydrogen contents [17]. Papanek et al. [482] reported a large reversible Li capacity due to Li intercalation and binding to these hydrogen-saturated sites at similar potentials. However, they showed that the binding of Li to a carbon atom in addition to a hydrogen atom changed the hybridization of the carbon-carbon bond from sp^2 to sp^3. This change in the carbon host resulted in a voltage profile hysteresis. Note, coating of hard carbons with a thin Al_2O_3 layer (~2 nm) as an artificial solid electrolyte interphase with the ability to conduct Li^+ ions upon lithiation also improved the average Coulombic efficiency of a hard carbon from 99.0 to 99.6% [483–485].

To date, it is assumed that Li insertion into graphene layers and nanopores of hard carbons occurs in the sloping and plateau regions [486–490]. Lotfabad et al. [104] and Kubota et al. [491] showed three distinct regions in the potential profile for the lithiation and delithiation of a hard carbon. Region I contains a sloping potential curve at $2.0-0.25$ V vs. Li^+/Li associated with the Li^+ ion insertion into the large interlayer spacings close to defects in the ionic state. In region II at an intermediate potential of $0.25-0.05$ V, the signal corresponds to the intercalation of Li^+ ions into the narrow interlayer spacings. The third region represents the low-potential region of $0.05-0.002$ V usually displayed as a plateau-like curve, and the capacity is mainly dominated by Li insertion into micropores with pseudometallic clustering. The same concept was identified for the sodium case [104]. Nevertheless, the contribution of each potential region to the final specific capacity can vary by the selected synthesis temperature. For sucrose-derived hard carbons treated at 700°C, the high potential region maximally contributes to the specific capacity while for samples treated at 2000°C the middle potential region becomes important as well. A large potential hysteresis for the lithiation and de-lithiation was observed for samples treated between 700 and 1300°C due to their higher dangling bonds or hydrogen terminated edges. This influence is smaller in samples treated at 1300°C $\leq$ T $\leq$ 2000°C. With increasing carbonization temperature, the potential of the anodic peaks shifted to lower voltages than the Li intercalation potential in graphite (~0.09 V vs. Li^+/Li) [491].

However, Qui et al. [424] reported on disadvantageous d-spacings for inserting Li according to the intercalation mechanism. They found that metal interactions with graphitic layers depend on the interlayer spacing and therefore determines if metal intercalation could occur or adsorption is the main step. Intercalation of Li hardly proceeded, given that the size of Li^+ ions is very small as compared with the d_{002} spacing of the hard carbon. The researchers inferred that the Li^+ ions were rarely intercalated into graphite with d-spacings >0.37 nm and an adsorption mechanism is preferred. The absence of a low-potential plateau in the CV curves indicated the correlation of the electrochemical behavior of Li^+ with an adsorption mechanism.

Notably, Alvin et al. [313] claimed that Li^+ intercalates in the graphitic layers at 0 V with very low current density of 0.003 A/g, and that metal plating occurred by further decreasing the potentials below 0 V (at -0.03 V). Su et al. [492] discussed a more smooth and homogeneous lithium deposition at the inside of nanopores of hard carbons during lithiation at -0.05 V compared to inhomogeneous Li dendrite formation on graphite during lithiation at -0.03 V. Alvin's group reported on extremely low insertion rates which help to unblock inaccessible Li^+ ion intercalation sites but only at voltages near 0 V, resulting in a low--voltage plateau capacity. To support this claim, they pointed to: 1) emerging broad peak at 4 ppm in solid-state ^7Li nuclear magnetic resonance (NMR) at the voltage between 0.1 and 0.0 V, indicating a strong interaction between Li and graphitic layers or micropore surfaces of the hard carbon; 2) the existence of the sharp and high-frequency peak at 9 ppm attributed to the Li^+ intercalation into the graphitic layers at potential near to 0 V; and 3) a chemical shift of 250 ppm corresponding to metallic Li at potential -0.03 V. To understand the behavior of the Li^+ ion insertion into the graphene layers of hard carbons, DFT calculations were performed and showed a constant d-spacing during the Li insertion. For further information, the average charges of the carbon atoms during the carrier-ion insertion were also calculated. Normally, after cation insertion, the edge carbon atoms become partially negatively charged, which induces an electric repulsion force between the carbon atoms. This repulsive force becomes stronger as the cation size and its intercalacted amount increases. However, it was observed during Li insertion, that the charge transfer to carbon was not sufficient to increase this repulsive force even after the insertion of a higher number of Li. On other hand, the high interactions between carrier atoms by increasing the amount of inserted atoms caused the carrier atoms became less ionic and subsequently decreased the charge transfer to the hard carbon. In a GITT profile at 0.05 A/g, the researchers observed that D_{Li}^+ values decreased as the voltage decreased. This result was attributed to the repulsive forces between absorbed Li^+ ions at high and low voltages. However, this behavior was completely different for the graphite anode. Two minimum D_{Li}^+ values between 0.1 and 0.05 V demonstrated that Li^+ gradually intercalated into the graphite layer.

4.4. Mechanism of sodium storage during electrochemical reactions

Different Na^+ ion storage mechanisms in hard carbons have been proposed in the high and low voltage regions [104,250,425,493]. A first proposed mechanism that applies to the high voltage region involves the adsorption of Na in the pores, between the domains and on the defect sites of hard carbons as these materials offer a wide adsorption energy distribution. A sloping voltage profile is caused by the adsorption sites. In the low voltage region, the intercalation of Na^+ ions between the graphene layers results in a plateau-like profile (Fig. 21 (a)). Avin et al. [313] showed the incomplete filling of the micropores present in highly porous carbons with low carbonization temperature while all the micropores present in the hard carbons synthesized at 1200-1500°C were filled with Na^+ ions. The remaining micropores could be filled later near the cutoff potential.

Pyrolysis of polyaniline (PANI) forms hard carbons with a low potential plateau between 0.0 and 0.2 V during Na^+ ion storage. In this voltage region, the intercalation of Na^+ ions into the spacing between the graphene layers appeared already. In this example, the high-voltage sloping region is related to Na^+ ion adsorption on storage-active surface sites [425]. Ding et al. [250] reported similar results for carbonized peat
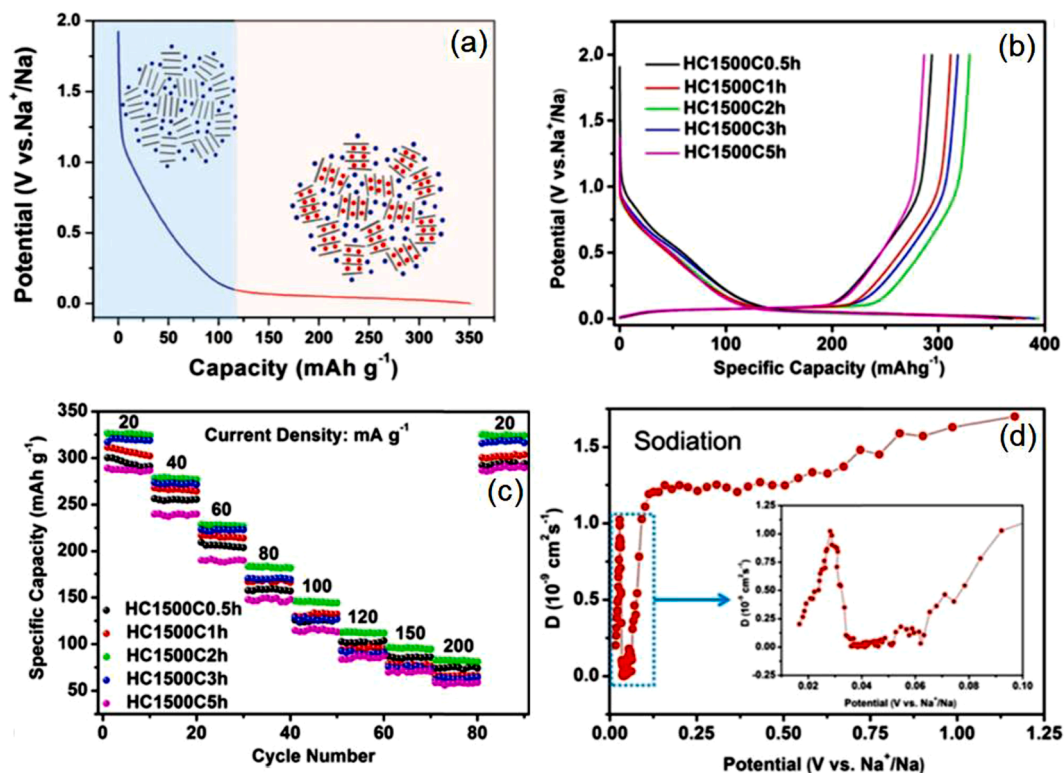
Fig. 21. a) Schematic illustration of the adsorption–intercalation mechanism for Na$^+$ ion storage in hard carbon [424]. b) Galvanostatic charge/discharge profiles of carbon derived from mangosteen shells carbonized at 1500°C for 0.5 h $\leq$ t $\leq$ 5h obtained at 0.02 A/g in the voltage range of 0−2 V. c) Cycling performance of hard carbons at various current densities from 0.02 to 0.2 A/g [494], and d) Na$^+$ ion diffusion coefficient determined from GITT experiments during the sodiation in the second cycle for HC1500C2h at 0.02 A/g [494]. Adopted from mentioned references after the required permission.

moss and attributed the low voltage region to the intercalation of Na$^+$ ions into a highly ordered pseudo-graphitic structure with dilated graphene interlayers. In their experiments, the interlayer spacing expanded from 3.96 to 4.16 Å and was inversely proportional to the voltage region with 0.1 V $\geq U \geq$ 0.001 V.

The contribution of the plateau capacity increased proportionately with the carbonization temperature [102,491]. For example carbons extracted from pine cone [102], sucrose [493], lotus stem [495], kelp [496], rice husk [497], pine nut shell [498], and corn cob [499] at 1600°C showed an initial low voltage plateau capacity two to three times larger than the capacity contributions from the high voltage sloping region. Fig. 21 (b) shows the charge/discharge profiles of hard carbon derived from mangosteen shell at a current density of 0.02 A/g in the voltage range of 0−2 V [494]. Hard carbon prepared at 1500°C (HC15002h) for 2 hours deliver the highest initial specific capacity of ∼330 mAh/g with a CE ≈ 83%. The rate performance of HC15002h at various current densities ranging from 0.02 to 0.2 A/g demonstrated a high specific capacity at a low-current density of 0.02 A/g, but also an excellent rate performance among other hard carbons derived from biomass (Fig. 21 (c)). For insights into sodium-ion storage mechanisms of hard carbons, galvanostatic intermittent titration (GITT) was used to measure the Na$^+$ ion diffusion coefficient. Fig. 21 (d) displays the Na$^+$ ion diffusion coefficient of carbonized carbon at 1500°C during the sodiation processes [494]. During the sodiation process at a decreasing voltage, Na$^+$ ion diffusion slowed down and, finally, at ∼0.06 V a sharp decrease in the diffusion coefficient was observed. At voltages <0.03 V, a large increase in the diffusion coefficient was again registered, which decreased until the cutoff voltage was reached. The low diffusion coefficient of Na$^+$ ions at low voltages and the high diffusion coefficient at high voltages corresponded with the plateau and sloping voltage regions of the discharging profile, respectively. The researchers related the higher diffusion coefficient in the sloping region to an easier adsorption

of Na$^+$ ions at the edges and surface defects of the graphene layers. The sharp decrease in the diffusion coefficient at ∼0.1 V represented kinetic barriers due to electrostatic repulsion during the intercalation of Na$^+$ ions into the graphene interlayers. This repulsive force explained the severe capacity fading in the plateau voltage region at high current densities. The sudden increase in the diffusion coefficient at voltages <0.04 V corresponded to sodium metal-nanovoid filling [494]. In the voltage range of 0-1.0 V, the Na$^+$ ion diffusion coefficient was two orders of magnitude lower than the diffusion coefficient of Li$^+$ ions into graphite [500].

Another mechanistic consideration focused on the storage characteristic of Na inside mesoporous hard carbon. The voltage sloping region was related to Na$^+$ ion insertion into the spacing between the graphene layers and the low voltage plateau region was attributed to Na filling/plating into nanopores [185,501,502] (Fig. 22 (a)). Therefore, a large number of available mesopores indicates an extended low-voltage plateau upon sodiation [253]. A decrease in the electron-density contrast between the carbon matrix and the nanopores was detected by *ex situ* small-angle X-ray scattering (SAXS) at voltages of 0, 0.2, and 2 V, and indicated that Na$^+$ ions filled the nanopores. As seen in Fig. 22 (b), the scattering intensity around 0.03–0.07 Å^{-1} (14-33 Å), which was attributed to the nanopores in this hard carbon, decreased reversibly, pointing to a decrease in the electron-density contrast between the carbon matrix and the nanopores [503].

The interlayer spacing in glucose-derived hard carbons was enlarged by shifting the broad Bragg 002 reflection to lower diffraction angles at 0.2 V as compared with the pristine electrode. This observation was accompanied by a complementary red shift of the Raman G-band at the same sloping voltage. Collectively, these observations confirm that the voltage-sloping region resulted from Na$^+$ ion insertion into the graphene interlayers [427]. The red shift of the G-band towards lower frequencies or wavenumbers resulted from the intercalation of the Na$^+$ ion between
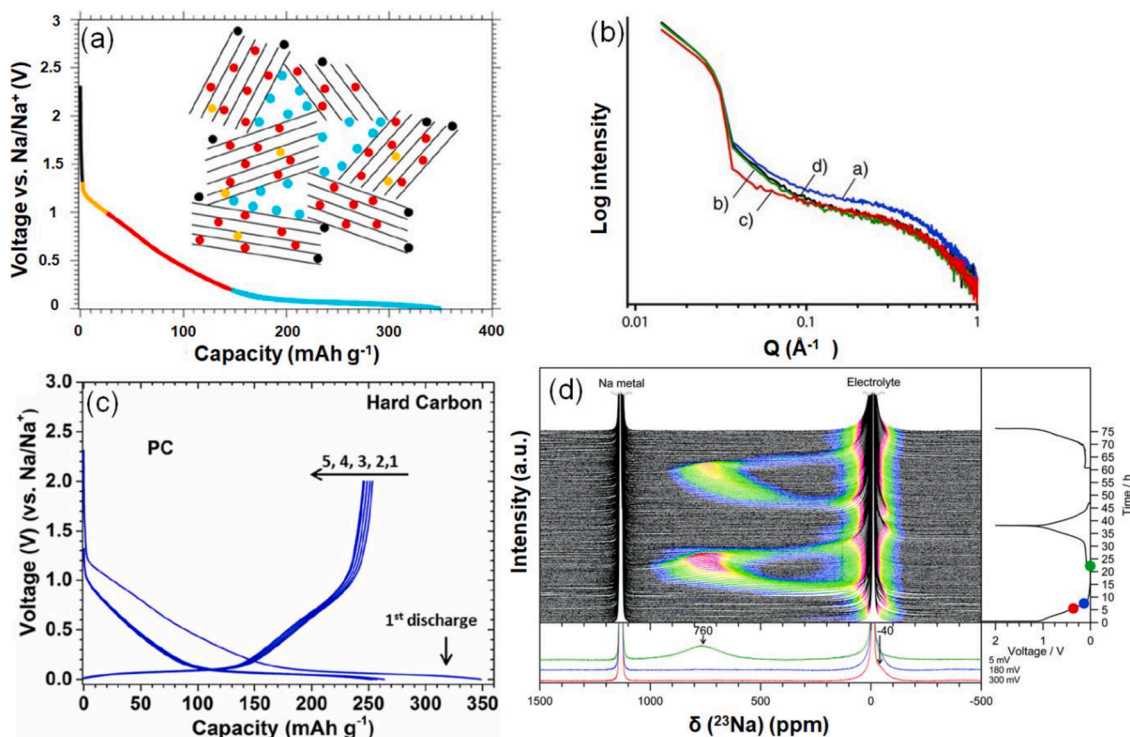
Fig. 22. a) Schematic illustration of the intercalation–adsorption mechanism for Na$^+$ ion storage in hard carbons mechanism [502]. b) *Ex situ* SAXS patterns for hard carbon electrodes: (a) pristine, galvanostatically reduced to (b) 0.20 V, (c) 0.00 V, and d) reoxidized to 2.00 V in 1 mol/dm^3 NaClO$_4$ PC [503]. c) Discharge-charge profiles of a carbonized coconut shell electrode for the first few cycles obtained in 1.0 M NaClO$_4$ in PC as the electrolyte [502], and d) *operando* ^{23}Na ssNMR spectra with selected spectra for hard carbon/Na with NaPF$_6$ as a electrolyte. The cell was cycled at a rate of C/20 (to achieve a capacity of 300 mA h/g in 20 hours) between 2 and 0.05 V, and held at the end of each discharge until the current dropped to below C/100 [504]. Adopted from mentioned references after the required permission.

the graphene layers, which was visualized by electron-density changes on the layer and led to a weakening of the interlayer C-C bonds [505]. This electron density was accordingly transferred into an antibonding π band of graphene layers [506]. During the intercalation of Na$^+$ ions into graphene interlayers, the I_G/I_D ratio decreased as the discharge voltage was lowered. The intensity of the G-band dropped dramatically when the voltage reached 0.1 V, whereas the D-band intensity remained constant until the final discharge voltage of 0 V [427]. However, in the voltage region of 0.1 V $\geq U \geq$ 0 V, the width of the D-band increased significantly and was blue-shifted towards higher wavenumbers [506].

Reddy *et al.* [502] reported similar results for carbonized coconut shells. Fig. 22 (c) displays the discharge-charge profiles of such a hard carbon electrode. They suggested that the sloping stage at higher voltages between 1.2 and 0.1 V vs. Na$^+$/Na corresponded with Na$^+$ ion adsorption on reactive surface sites and Na$^+$ ion insertion at defect sites and between layers up to NaC$_{24}$. Further, the accommodation of metallic Na in the nanopores occurred in the plateau region at 0.1-0.0 V vs. Na$^+$/Na. However, the defect concentration should not be too high, because the activation barriers for the Na$^+$ ion diffusion increase considerably close to defect sites, and these increased barriers could be an explanation for part of the irreversible capacity. The initial charge capacity was 254 mAh/g, with an irreversible capacity loss of 95 mAh/g. Stratford *et al.* [504] also proposed a two-stage mechanism for insertion of Na$^+$ ions into hard carbons. These researchers found that *operando* ^{23}Na ssNMR spectra were dominated by two peaks at -10 ppm and 1135 ppm for the pristine electrochemical cell corresponding to the NaPF$_6$ in the electrolyte and the Na metal counter electrode, respectively. In the electrochemical process at voltages ~0.8 V, a single resonance initially appeared close to 0 ppm. The observed peak at ~0 ppm was related to the formation of the SEI layer related to electrolyte decomposition. At the sloping region close to a voltage of 0.8 V, the signal shifted to a negative frequency of -40 ppm. However, a small negative shift at -4

ppm was detected by *ex situ* ^{23}Na MAS NMR. These observations indicated the transfer of charge from inserted Na to carbon sheets at higher voltages associated with a localized charge near the carbon defects and not throughout the whole graphene sheets. The researchers therefore suggested that at higher voltages Na is largely deposited on pore walls and in larger interlayer regions, most likely near defects. Finally, by reaching a voltage below 0.18 V, an additional signal at a positive frequency of 760 ppm emerged (Fig. 22 (d)) which implied that the sodium species became metallic during the electrochemical process. They concluded regarding the strong ionic binding energy between the Na$^+$ ions and the defects (mono- and divacancies), and the weakened van der Waals interaction, that Na$^+$ ion intercalation was enhanced greatly at higher voltages. At lower voltages, the Na$^+$−C interaction gradually became less ionic and the charge transfer to the Na$^+$ ions increased, which finally resulted in the extension of Na clusters as more metallic into the pore structure. However, at lower voltages the Na$^+$ iintercalation between disordered graphene layers continued.

Yet another scenario is discussed in a mechanistic sense to understand the underlying process in the sloping and plateau regions. The sloping region in the voltage range of 1 V $\geq$ U $\geq$ 0.1 V is considered to belong to Na$^+$ ion adsorption at disordered graphene layers of the hard carbon material and the plateau region at ≈0.1 V is related to nanopore filling. Zhang *et al.* [507] investigated a polyacrylonitrile (PAN) carbonized at temperatures higher than 1000°C. Here, the sloping region was related to Na$^+$ ion storage on isolated or randomly oriented graphene layers and defect sites created by heteroatoms. The high specific charging capacity obtained at voltages $\geq$1 V was most likely reached by the high content of heteroatoms. The constancy of the *d*-spacing of the carbonized PAN during Na$^+$ ion storage showed a relationship of the development of the plateau region and the nanopore filling. By increasing the temperature above 2000°C, the sloping region diminished because of the improved ordering of graphene layers and the

removal of the heteroatoms. A single plateau at almost 0.1 V with a capacity of ≈200 mAh/g remained. In the study of Kano *et al.* [508], hard carbons prepared at 2600°C with a high volume of closed pores of 0.37 cm^3/g yielded a high reversible capacity of up to 413 mAh/g in the voltage range of 0.2 to 0.0 V vs. Na$^+$/Na [509]. Kamiyama *et al.* [510] confirmed the participation of the large total volume of the closed pores produced at high temperatures to a high specific capacity at U < 0.15 V.

Zhang *et al.* [495] demonstrated that the presence of closed pores rather than open pores in hard carbons were responsible for Na-metal cluster formation. Here, hard carbons derived from lotus stems treated at 1400°C compared to other carbonization temperatures showed the highest closed nanopore volume which contributed to the largest plateau capacity at low voltage. The researchers assumed that at high temperatures open pores due to the internal structure shrinkage were sealed and thus, the closed pore ratio reached a maximum for the sample treated at 1400°C. Comparatively, the sample treated at 1400°C exhibited a distinct plateau capacity at -0.01 V, which further proved that Na metal deposition was linearly related to the closed pore ratio. Kubota *et al.* [491] suggested that small internal micropores formed at low temperatures between the carbon planes are preferable for Li to form small and planar clusters, whereas large micropores formed at high temperatures support the Na clustering. Additionally, the reversible specific sodiation capacities of hard carbons independent of the synthesis temperature are mainly dominated by the formation of pseudo-metallic Na clusters in micropores.

4.5. Aspects of the potassium-storage mechanism

Although the electrochemical properties of Na- and Li-cation storage in hard carbons have been discussed in depth, the detailed K-cation storage mechanism in hard carbon materials remains unclear. A broadly accepted K-storage mechanism in hard carbons is the adsorption-intercalation mechanism [313,483,511,512].

Alvin *et al.* [313] suggested that Na and K voltage profiles, besides showing the sloping at higher voltages, also displayed plateau regions at lower voltages. This observation was in contrast with the voltage profile of Li with only a sloping region. The plateau capacities of SIB and KIB originate from the ion insertion into the graphitic layers, whereas ion adsorption on the defect sites is responsible for the sloping capacities. However, the contribution of the capacity in SIB usually attributed to the plateau region was more distinct compared to KIBs. As the carbonization temperature increased from 1000 to 1500°C, the sloping capacity in the LIB, SIB and KIB gradually decreased, while the low-voltage plateau capacity in SIB and KIB increased. They demonstrated that Li$^+$, Na$^+$, and K$^+$ ions intercalated into the graphitic domains of lignin derived-hard carbons at low voltages of 0, 0.1, and 0.25 V, respectively [313]. Chen *et al.* [511] also confirmed the K$^+$ ion insertion mechanism proposed by Alvin *et al.* [313] but showed a poor rate capability with increasing carbonization temperature related to a higher degree of graphitization. Along with these observations, Qian *et al.* [513] were able to follow the influence of mesopores on the adsorption and the later intercalation of K$^+$ ions into a disordered carbon. According to their results, such pores are able to accommodate up to six K$^+$ ions which enhances the transport kinetics significantly. Additionally, the I_G/I_D ratio as a measure of the defect concentration in the carbon matrix obtained from Raman spectroscopy measurements seem to play a more important role than other properties like interlayer distance, adsorption capacity or specific surface area in KIBs.

Recently, Kubota *et al.* [491] demonstrated another mechanistic consideration focused on the storage of potassium into the spacing between the graphene layers at a higher voltage, and K$^+$ ion insertion into micropores at a low voltage. Within the three sloping potential regions of 0.002-0.2, 0.2-0.7, and 0.7-2.0 V vs. K$^+$/K, K$^+$ ions insert first into the large graphene interlayer spacing accessible in the high-potential region of 0.7-2.0 V vs. K$^+$/K. In a second step, the K$^+$ ions occupy the narrow interlayer at the intermediate potential region of 0.2-0.7 V vs. K$^+$/K. The

third insertion into the micropores takes place in the low potential region of 0.002-0.2 V vs. K$^+$/K. The carbonization temperature was identified as the main influence on the insertion mechanism. For samples treated at low temperatures the dominant mechanism is the insertion of K$^+$ ions into the larger spacings between the graphene layers while higher temperatures support the intercalation of K$^+$ ions into the interlayer with small distances.

Fig. 23 (a-b) present the dQ/dV curves in which intercalation and de-intercalation of K$^+$ ions into and out of the hard carbon was started at 0.2 V and 0.33 V respectively, versus K$^+$/K, whereas both intercalation and de-intercalation of Na$^+$ ions were detected at voltages lower than 0.1 V versus Na$^+$/Na. This higher intercalation voltage of K$^+$ ions into hard carbons enabled them to tolerate the larger potential polarizations at higher current densities. Thus, a better rate capability was expected that would enable KIBs to perform better than SIBs, especially with respect to high-power energy storage applications. Fig. 23 (c-d) display voltage-capacity curves during the potassiation/depotassiation and sodium/desodiation of hard carbon electrodes with two sloping and two plateau potential regions. At a slow rate of C/10, a reversible capacity of 262 mAh/g was obtained for the depotassiation process, which is lower than 322 mAh/g associated with the desodiation process. At C-rates ≥ C/2, the capacities of the KIB outperformed those of SIB (Fig. 23 (e)). GITT experiments were conducted at C/10 to investigate the cause (Fig. 23 (f)). Surprisingly, the diffusion coefficient of the K$^+$ ions was determined to be slightly higher compared to Na$^+$ ions in both insertion and removal. This unexpected difference in the diffusion coefficients was explained by different binding energies between K and carbon and Na and carbon. A lower charge density of the larger K$^+$ ion, the different levels of ionicity of Na$^+$ and K$^+$ ions, and their varying ability to form covalent bonds with carbon structural sites were identified as the main influences [514].

For improving the specific capacity of a KIB at high rates, utilization of N-doped hard carbons with a porous surface as anode materials were proposed. However, to avoid the low initial CE attributed to the high specific surface area of hard carbons, some researchers revealed sodium carboxymethylcellulose (CMCNa) as binder which had a significant effect on the electrochemical performance [515–517]. CMCNa increased mechanical strength and stability of the formed SEI and improved the initial CE by 10% as compared with polyvinylidene fluoride [518].

Hierarchical porous hard carbons with a specific surface area of 1030 m^2/g were subjected to dual-heteroatom doping (N and O). This procedure led to specific capacities of 365 and 118 mAh/g at 0.025 and 3 A/g, respectively. The quasi-rectangular shape of the CV suggests that the total K charge storage results from a faradaic insertion/extraction of K$^+$ ions and a reversible non-faradaic adsorption, whereas the contribution of the non-faradaic adsorption becomes more significant at higher rates [515]. Chen *et al.* [430] reported the synthesis of shrimp shell-derived hierarchically porous nitrogen-doped carbon microspheres. The specific capacity of 154 mAh/g at a high rate of 72 C and great cyclic capacity of 180 mAh/g at 1.8 C over 4000 cycles demonstrated a promising performance of this porous carbon as anode material in KIBs. The investigated hierarchically porous and additionally nitrogen-doped microstructure of the obtained carbon caused a capacitive (surface-driven) process that dominated the charge-storage behavior. In the voltage profile, no obvious plateau at ~0.2 V corresponding to K$^+$ intercalation was detected, which underlined that the majority of the capacity resulted from the surface-driven reaction in the sloping region. The valence-electron density of the K atom was totally transferred to the bonding carbon in this example and was accumulated around the N-doping site. In addition, DFT calculations revealed that pyridinic N, which was identified as the dominating N species in the obtained porous carbon, increased the amount of ionic K−C bonds around itself and thus led to stronger K$^+$ ion adsorption. These results clearly point to the contribution of N doping to improve the performance of potassium-ion batteries.
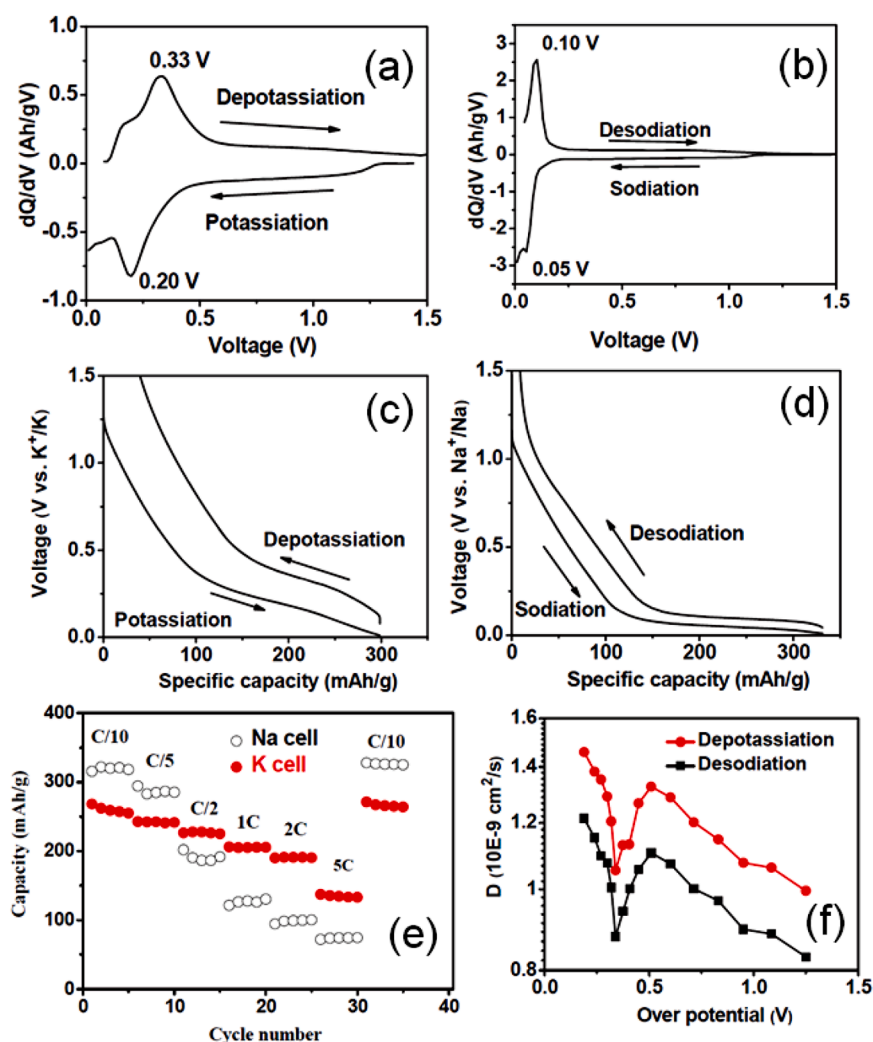
Fig. 23. dQ /dV profiles of a) potassiation and depotassiation, b) sodiation and desodiation of hard carbons. Discharge/charge profiles at C/10 in the second cycle of c) hard carbon/K half-cell, and d) hard carbon/Na half-cell. e) Rate capability performance of hard carbon/K and hard carbon/Na half cells, and f) diffusion coefficients calculated from the GITT experiments for hard carbon/K and hard carbon/Na half cells during the second charging cycle. Adopted from [514] after the required permission.

4.6. Summary of the biomass-derived carbons and their respective battery performances

Table 2 presents a comprehensive comparison of all affecting aspects of the biomass-derived carbons synthesized by various methods. To date, many groups tried to modify the carbon structure using various methods to improve the performance of these materials as potential anodes in batteries. However, a systematical understanding of the overall functioning of hard carbons in batteries is challenging and still a subject of controversy. Mainly the uncontrolled heterogeneity of the carbon materials obtained from different biomass sources by distinct synthesis approaches is the most important reason. Generally, some carbon materials inherit their biomass structure, while others are modified by more complex methods to obtain the desired structure, such as particles, nanofibers and nanotubes. Significant results were achieved to control the final carbon porosity content, size and shape in order to improve its performance in the final battery. In addition, doping the carbon, with elements such as B, N, F, P or metals with electron acceptor or donor capability in order to modify crystallite domains, interlayer distances and the number of point defects, is another way to increase the efficiency of these materials for battery operation. However, if the defect concentration generated around the elements is too high, it will act as an obstacle to the free movement of metal ions and electrons or can simply trap the adsorbed ions leading to irreversible capacities.

In all biomass-derived hard carbons, different characteristics like inherent porosity and defects, a wide range of interlayer spacings, the presence of (natural) doping elements such as N and P, exist simultaneously. These synergetic effects make it difficult to understand which factor plays a decisive role in increasing battery capacity or long-term stability. Nevertheless, the first principle to reach a relatively high and stable performance of hard carbon materials is to provide a structure facilitating ion movement during charging and discharging. As the second, a sufficient electrical conductivity is needed which directly impacts the charge transfer.

Pores can irreversibly trap metal ions, therefore, a low specific surface area of less than 40 m^2/g with a low micropore volume is desirable. For potassium, even mesopores can be beneficial. A low specific surface area can suppress parasitic side reactions, thus reducing irreversible capacity losses during the charging and discharging processes. Considering that, lignin hard carbons with the lowest specific surface area exhibit the highest Coulombic efficiency. Moreover, the presence of meso- and macropores in lignin-derived hard carbons supports ionic diffusion. This effect becomes more pronounced when these pores are interconnected. However, the low-potential Na^+ ion storage and amount of close, non-interconnected pores increase with temperature of the heat treatment. Heat treatments of carbons at $T > 1500°C$ lead to a transformation of open to closed pores. From the other side, increasing the distance between carbon layers as well as enhancing the crystallinity can support metal ion accommodation, especially in case of Na and K. Doping of carbons with some electronegative elements can also help to accelerate alkaline ion diffusion and fast charge transfer.

The electrical conductivity of carbon is the other important factor for

Table 2
Biomass-derived hard carbons and their performances as anodes in LIBs, SIBs and KIBs

Biomass resources	Salt/electrolyte/binder	Mass loading	Voltage range (V)	Reversible capacity (mAh/g)/ Current density (A/g)/ Cycles	Morphology/ interlayer distance	BET(m^2/g)/pore volume (cm^3/g)/pore diameter(nm)
				LIBs		
Corn cob [519]	1 M LiPF$_6$ EC:DEC (1:1, v/v)/ PVDF	5-8 mg	0.01-3	660/0.1/180	Nanosheet /-	719/0.46/2.6
Indian prawn shell [520]	1 M LiPF$_6$ EC:DEC (1:1, v/v)/ PVDF	—-	0.01-3	730/0.1/150	N-doped spherical particles / 0.35 nm	336/–/2-50
Coffee grounds [521]	1 M LiPF$_6$ EC:DEC (1:1, v/v)/ PVDF	25 μm	0-3	285/0.1/100	Irregular shape /–	<10/non-porous
Coir pith [522]	1 M LiPF$_6$ EC:DEC (1:1, v/v)/ PVDF	~12 g/m^2	0.01-3	837/0.1/50	Carbon sheet	2500/–/1.4-1.7
Sugarcane bagasse [523]	1 M LiPF$_6$ EC:DEC (1:1, v/v)/ PTFE	30 g/m^2	0.01–3	1052/0.1/80	N-doped interconnected frameworks structure	1940/1.3/3.2
Mangrove charcoal [524]	1 M LiPF$_6$ EC:DEC (1:1, v/v)/ PVDF	—-	0-1.5	350/0.03/50	Quasi-spherical structural including disoriented graphene layer	—
Rice straw [525]	1 M LiPF$_6$ EC:DMC (1:1, v/v) and FEC/ PVDF	—-	0-3	137/3.75/10	Fibers	243/0.41/0-25
Pinecone [526]	1 M LiPF$_6$ EC:DMC:EMC (1:1:1, v/v/v)/ PVDF	—-	0.02- 2	394/0.007/8	microporous	380/0.2/1-2
Peanut shell [527]	1 M LiPF$_6$ EC:DEC (1:1, v/v)/ PVDF	1.4 mg	0.01-3	474/1/400	3D connected porous structure	706/–/<2
Banana peel [104]	1 M LiPF$_6$ EC:DMC:DEC (1:1:1, v/v/v)/ PVDF	10 g/m^2	0.001-2.8	221/0.5/600	Irregular shape /0.39	130/0.19/~3
Bamboo [528]	1 M LiPF$_6$ EC:DEC (1:1, v/v)/ PVDF	—-	0-2	116/0.5/500	Microtubular carbon fibers / 0.39-0.4	29/0.04/<10
Orange peel [529]	1 M LiPF$_6$ EC:DEC (1:1, v/v)/ PVDF	—-	0.01-3	301/1/100	Irregular shape	638/–/<2
Fish scale [530]	1 M LiPF$_6$ EC:DEC (1:1, v/v)/ PVDF	3.5-4 g/m^2	0.01-2.5	390/0.4/75	N- doped interconnected porous structure / 0.38	1980/0.93/4-30
Cattle bone [531]	1 M LiPF$_6$ EC:DEC (1:1, v/v)/ PVDF	8-10 g/m^2	0.01-3	1488/1/250	Fiber bundle-like structure	2096/1.83/4
Ramie fiber [519]	1 M LiPF$_6$ EC:DEC (1:1, v/v)/ PVDF	5-8 mg	0.01-3	523/0.1/180	3D rod-like micro-structure /–	344/0.22/2.53
Tea leaves [532]	1 M LiPF$_6$ EC:DMC:EMC (1:1:1, v/v/v)/ PVDF	50 μm	0.005-3	471/0.037/50	Irregular microporous structure	146/0.05/5
Cherry stone [533]	1 M LiPF$_6$ EC:DEC (1:1, v/v)/ PVDF	—-	0-3	270/0.37/100	Irregular microporous structure	549/0.31/–
Olive stone [533]	1 M LiPF$_6$ EC:DEC (1:1, v/v)/ PVDF	—-	0-3	180/0.074/100	Irregular microporous structure	587/0.33/–
Human hair [534]	1 M LiPF$_6$ EC:DMC (1:1, v/v)/ PVDF	13 g/m^2	0-3	1331/0.1/50	3D connected porous structure	1250/ –/1-4
Coconut oil [405]	1 M LiPF$_6$ EC:DEC (1:1, v/v)/ PVDF	1.5 mg	0.005-3	577/0.1/20	Quasi-porous spherical morphology	133/–/–
Mushrooms [535]	1 M LiPF$_6$ EC:DMC (1:1, v/v)/ no binder	0.5 mg	0.01-3	260/0.1/700	Hierarchically porous carbon nanoribbons	19.6/–/6-26
Cashew nut sheath [536]	——	—-	0.01-3	620/0.1/100	Porous particle	1967/0.876/2-8
Walnut shell [537]	1 M LiPF6 EC:DMC (1:1, v/v)/PVDF	—-	0.01-3	150/0.1/100	Nano fibers	408/0.25/0.8-1
				SIBs		
Corn cob [499]	0.6 M NaPF$_6$ in EC:DMC (1:1 V)/ Sodium alginate	20-30 g/m^2	0-2	275/0.06/100	Irregular non-porous particles /0.398	3.7/–/–
Shaddock peel [538]	1M NaClO$_4$ EC:DEC (1:1, v/v)/ PVDF	—-	0-3	350/0.05/250	Honeycomb-like morphology/0.38	82/0.049/0.6-15
Indian prawn shell [520]	1M NaPF$_6$ EC:DEC (1:1, v/v)/ PVDF	—-	0.01-3	325/0.1/200	N-doped spherical particles/ 0.35 nm	336/–/2-50
Coffee grounds [523]	1 M NaClO$_4$/ TEGDME/ PVDF	—-	0.01-3	154/0.2/50	Irregular porous particles /–	94/–/10-30
Coir pith [539]	1 M NaClO$_4$ EC: PC (1:1 v/v)/ PVDF	20 g/m^2	0.01-3	220/0.05/300	Microporous graphene sheet	2500/–/–
Sugarcane bagasse [540]	1 M NaClO$_4$ EC:DEC (1:1, v/v)/ PVDF	15 g/m^2	0.01-2	220/0.1/300	Flake-like morphology /0.374	2/–/–
Switchgrass [541]	1 M NaClO$_4$ EC:DEC (1:1 v/v)/ PVDF	50 g/m^2	0.01-2	200/0.025/400	3D structure with linked macropores	620/–/1.7-110
Mangrove charcoal [542]	1 M NaPF$_6$ PC/ SBR-CMC	—-	0-2	278/0.03/5	Irregular shape/0.37	6.8/–/~0.52

Table 2 (*continued*)

Biomass resources	Salt/electrolyte/binder	Mass loading	Voltage range (V)	Reversible capacity (mAh/g)/ Current density (A/g)/ Cycles	Morphology/ interlayer distance	BET(m^2/g)/pore volume (cm^3/g)/pore diameter(nm)
Rice straw [543]	1 M NaClO$_4$ EC:DEC (1:1, v/v)/ PVDF	10-15 g/m^2	0.01-2	346/0.025/100	Irregular granular shape /0.395	~0/~0/undetectable
Pinecone [102]	1 M NaClO$_4$ EC:DEC (1:1, v/v)/ CMC	15-25 g/m^2	0.001-2	334/0.03/120	Irregular shape /0.381	40/0.03/3
Argan shell [544]	1 M NaPF$_6$ EC: DEC (1:1, v/v)/ PVDF	12-20 g/m^2	0-2	300/0.025/70	Irregularly shape /0.385	24/0.018/3
Peanut shell [527]	1 M NaClO$_4$ EC:DEC (1:1, v/v)/ PVDF	1.4 mg	0.01-3	190/0.25/400	3D connected porous structure	706/– /<2
Banana peel [104]	1 M NaClO$_4$ EC:DEC (1:1, v/v)/ PVDF	----	0.001-2.8	210/0.5/600	Irregular shape /0.39	130/0.19/ ~3
Orange peel [529]	1 M NaClO$_4$ EC:DEC (1:1, v/v)/ PVDF	----	0.01-3	156/0.5/100	Irregular shape	638/–/<2
Apple [545]	1 M NaClO$_4$ EC/PC (1:1, v/v)/ CMC	22-25 g/m^2	0.02-3	245/0.02/80	Irregular shape /0.385	196/–/–
Ramie fiber [519]	1 M NaClO$_4$ EC: DEC(1:1, v/v)/ PVDF	----	0.01-3	122/0.1/100	Nano-sheet/-	719/0.46/2.6
Bamboo [528]	1 M NaClO$_4$ EC:DMC (1:1, v/v) and FEC/ PVDF	----	0-2	200/0.1/160	Microtubular carbon fibers/0.39-0.4	29/0.04/<10
Blue-green algae [546]	1 M NaClO$_4$ EC:DEC (1:1, v/v)/ PVDF	----	0.01-2.5	230/0.02/60	Carbon filament/0.36	–
Wheat straw [547]	1 M NaClO$_4$ EC:DEC (1:1, v/v)/ PVDF	----	0.01-3	221/0.05/200	Linked tubular macropores/ 0.383	111/0.09/3.8
Coconut oil [405]	1 M NaClO$_4$ EC:PC (1:1, v/v) and FEC/ PVDF	1.5 mg	0.005-3	203/0.1/50	Quasi-spherical morphology	133/–/–
Cashew nut sheath [536]	------	----	0.01-3.0	200/0.1/100	Porous particle	1967/0.876/2-8
Cotton [184]	0.8 M NaPF$_6$ EC: DMC (1:1, v/v)/ Sodium alginate	25-35 g/m^2	0-2	305/0.03/100	Hollow fibers with diameters around 10-20 μm/0.41	38/–/1-1.5
Egg shell [548]	1 M NaClO$_4$ PC/PVDF	10-15 g/m^2	0.001-3	246/0.05/200	Carbon fibers	28/–/–
Walnut shell [549]	1 M NaClO$_4$ EC:DMC (1:1, v/v) and FEC/ PVDF	2-3 mg	0.01-3	170/0.1/300	Continuous pore channel shape /0.37	59/–/–
Pistachio shell [550]	1 M NaClO$_4$ EC:PC (1:1, v/v)/ PVDF	----	0.001-2	185/0.6/500	Irregular shape/0.36	137/0.06/0.74
Holly leaf [551]	1 M NaClO$_4$ EC:DEC (1:1, v/v)/ PVDF	----	0.01-3	253/0.02/100	Lamellar structure/–	–/–/1
Pomelo peels [450]	1 M NaClO$_4$ EC:PC (1:1, v/v)/ PVDF	----	0-3	181/0.2/220	Carbon sheets with 3D connected porous structure /	1272/–/4-23
Peat moss [250]	1 M NaClO$_4$ EC: DEC (1:1, v/v)/ PVDF	10 g/m^2	0.001-2.8	255/0.1/200	Nanosheets with hollow macroporous architecture /0.388	197/0.18/<4
Wood cellulose [552]	1 M NaClO$_4$ EC:DEC (1:1, v/v)/ no binder	25 g/m^2	0.01-2.5	196/0.1/200	Ribbon-like structure	126/–/–
Okara [127]	1 M NaClO$_4$ EC: DMC (1:1, v/v) and FEC/ PTFE	14 g/m^2	0.01 -2	247/0.11/50	N-doped- loosely packed graphitic sheets /0.39	–
Lotus petiole [343]	1 M NaClO$_4$ EC:DEC (1:1, v/v)/ PVDF	10-15 g/m^2	0.001-2.8	228/0.2/200	F doped-Irregulat shape/0.4	46/–/–
Apricot shell [144]	1 M NaClO$_4$ EC:DEC (1:1, v/v)/ PVDF	12 g/m^2	0-2.5	338/0.1/300	3D connected porous structure /0.38	13/–
Dandelions [103]	1 M NaClO$_4$ EC:DEC (1:1, v/v)/ PVDF	10-20 g/m^2	0.001-3	364/0.05/10	Smooth hollow tube/0.37	5/–
Coconut shell [502]	1 M NaClO$_4$ PC and FEC/ PVDF	15-20 g/m^2	0-2	250/0.01/40	Irregular shape/–	–
KIBs						
Potato [553]	3M KFSI DME/PVDF	8-12 g/m^2	0.01-2.7	196/0.5/400	Irregular shape/–	531/–/9.2
Ganoderma lucidum spore [554]	1.0 M KPF$_6$ EC:DEC (1:1, v/v)/ PVDF	----	0.02–3	195/0.1/100	Caged porous carbon/–	104/–/–
Walnut septum [555]	0.8 M KPF$_6$ EC:DEC (1:1, v/v)/ PVDF	----	0.005- 3	120/1/1000	N-doped porous tubular structures/0.376	100/–/20
Loofah [489]	1.0 M KPF$_6$ EC:DEC (1:1, v/v)/ PVDF	10-20 g/m^2	0.01-3	150/0.1/200	honeycomb-like micro-tubular structure	270/0.17/3.6
Cotton [556]	1.0 M KPF$_6$ DME/ PVDF	----	0-2	120/2/500	Hollow fiber structure	427/–/1.88
Soybeans [483]	0.8 M KPF$_6$ EC:DEC (1:1, v/v)/ PVDF	15 g/m^2	0.01-3	196/0.05/900	Irregular shape/0.38	380/0.19/2
Hard-wood (oak) [557]	0.4 M KPF$_6$ EC:DEC (1:1, v/v)/ PVDF	2.4 mg	0.01-2.5	150/0.1/150	Interwoven nanoporous channels/ 0.4	156/–/3-20
Sucrose [557]	0.4 M KPF$_6$ EC:DEC (1:1, v/v)/ PVDF	20 g/m^2	0.01-2.5	50/0.1/150	Porous spherical particle /0.4	65/–
		----	0.01-3	180/0.5/4000	N-doped porous microspheres	563/–/10

Table 2 (*continued*)

Biomass resources	Salt/electrolyte/binder	Mass loading	Voltage range (V)	Reversible capacity (mAh/g)/ Current density (A/g)/ Cycles	Morphology/ interlayer distance	BET(m²/g)/pore volume (cm³/g)/pore diameter(nm)
Sea food waste [430]	0.8 M KPF$_6$ EC:DEC (1:1, v/v)/ PVDF					
Rice husk [512]	0.8 M KPF$_6$ EC:DEC (1:1, v/v)/ PVDF	15 g/m²	0.01–3	103/0.5/300	Irregular shape/0.39	115/0.13/<3

battery performance. Hard carbons with a low density of less than 1.5 g/cm^3 hamper a preparation of thin conductive electrodes, having less contact to the current collector. To decrease the thickness of the electrode, hard carbons with a low specific surface area and random morphologies including broad particle size distribution for dense compacting are desired.

Furthermore, low intrinsic electrical conductivity and unsatisfactory rate performance of the biomass-derived hard carbon carbon are mainly linked to its disordered structure. The graphitization of a non-ordered carbon structure using transition metals as catalysts to have a non-graphitic/graphitic composite matrix, or modification of the graphene layer structure with elements such as nitrogen, can increase the electrical conductivity. Among biomass waste materials, those with high cellulose content showed higher degrees of graphitization compared to that of materials enriched with lignin even at high temperatures (>2000°C). However, cellulose has a low carbon content that makes it economically unsuitable for extensive use. Therefore, specific modification of lignin with its higher carbon content, e.g. by iron-catalyzed processes, can yield larger amounts of an electrically higher conductive material.

5. Summary and outlook

Rechargeable alkali metal-ion batteries are already well established for many devices that require cordless power supply. These applications are realized primarily by batteries with lithium-based chemistries because lithium enables high energy power (e.g. for tools) or high energy density needed for vehicles in versatile battery architectures. Despite the advantages of lithium-based batteries, the limited availability of lithium may help to support the breakthrough of rechargeable sodium and potassium batteries. Indeed, the last 10 years have witnessed great effort toward making such batteries into promising candidates for next-generation energy storage devices. However, these devices still need materials with even higher electrode performance, especially to improve power and energy density.

Graphite is to date the most used anode material in LIBs, which also promises for suitable electrochemical storage performance properties for sodium- and potassium-ion batteries. However, the large Coulombic repulsion between lithium cations in the nearest-neighbor sites and the ineffectiveness of graphite to accommodate noteworthy concentrations of sodium cations between the graphene layers restricts the storage of large amount of heavier alkali metal ions in graphite.

Nevertheless, in the process of purifying natural graphite, hydrofluoric acid must be used to remove silicate impurities. Intensive use of this toxic acid can pose detrimental impact on the environment. Synthetic graphite produced from coking natural pitches or residues of crude-oil distillation at 2500–3000°C with better performance and reliability compared to natural graphite still suffers from the long production process and high energy consumption. The use of fossil fuels to support its production process results in additional CO_2 emission (7.5–9.9 kg CO_2 per kWh) [558]. Thus, it is mandatory to progressively introduce domestic, sustainable, and non-toxic sources to synthesize graphite anodes at relatively low temperatures and without the use of hydrofluoric acid.

Hard carbon is typically produced from fossil sources and biomass. It represents a non-graphitizable, amorphous carbon with randomly distributed clusters of partially oriented graphene sheets, and can offer more active storage sites and show better electrochemical performance than the highly ordered graphite.

However, the cost of carbon from fossil sources is unpredictable as it is related to, e.g. the price of crude oil in stock exchanges or nowadays to climate taxes, as such a carbon is not sustainable. By contrast, biomass from different sources, including wastes, offers versatile carbon structures and an easy and generally cost-effective carbonization strategy, with an increasing economic value by the finishing to a high-value product. Biomass-derived carbon products of different structure dimensionality have received an increasing level of interest for the fabrication of electrodes for energy storage devices. The focus has initially been set on applications as anodes in alkali metal-ion batteries. Nevertheless, the application of biomass-derived hard carbons in a cathode composite may also be valuable for improving the performance of alkali-metal batteries, especially SIBs and KIBs [439].

However, some barriers need to be overcome to industrially produce carbon from most biomass sources for application as anodes. Sources of biomass are quite diffuse and may not be available in sufficient quantities. Many sources also suffer from a low carbon yield and substantial efforts for purification are required. In view of the typically non-uniform structure of biomass, it may remain challenging to reproduce the carbonization process on an industrial scale, in particular, to safely control the morphology and structure of the biomass-derived carbon to guarantee a product with constant properties. This aspect can be considered as the skeleton key to its use as anode materials in a battery. Indeed, the chemical composition of the same type of biomass can vary based on soil feeding type, age of the plants, fertilizer and pesticide dose, harvesting time, and the climate and geographical conditions [49,559, 560]. Although this composition variation of biomass growing at different conditions are not significant. It can change between 38-44% for cellulose, 20-23% for hemicellulose and 18-22 % for lignin [561]. Therefore, it is crucial that future work provides deeper insights into understanding of the composition of biomass precursors and the mechanisms underlying the biomass-related effects and properties of the final carbon.

As a further subject, the broad use of biomass resources to create sustainable and eco-friendly batteries should be scrutinized. One important milestone for battery use is the zero CO_2 emission electric vehicle (EV). Beside the aspect of non-fossil fuel power generation for the climate neutral EV, producing carbons from phytomass as plants or utilizing waste biomass can actively store larger amounts of CO_2 and can be one important part in the mission to keep the CO_2 value at least constant. Biomass sources themselves reduce our dependence on fossil fuels can decrease greenhouse gas emissions. However, this idea is working for fast growing plants and that as fast as the biomass is burned, new trees or plants take up CO_2 produced by the combustion. Thus, the CO_2 cycle theoretically remains in balance, and no extra carbon is added to the environment. Some possible solutions and outlooks can be found elsewhere [562–565]. In addition, when the battery electrodesreach their end-of-life, they could be decomposed biologically or incinerated, and its compounds can be recycled to the environment.

Beside all positive aspects, negative sides are identified as well and need to be solved to avoid environmental and social discrepancies or worse. Disturbing the balance of an ecological or a social system can be disastrous that may comprise economic reasons like land speculation,

concurring crops like food vs. energy production, monocultures, extended land or water consumption to name just a few [566–568]. Even continuously removing "waste" biomass from the natural life cycle, that would otherwise become mixed manure at natural conditions, may have long-term negative effects on soil fertility and wildlife habitat [569].

Declaration of Competing Interest

The authors declare that they have no known competing financial interests or personal relationships that could have appeared to influence the work reported in this paper.

Acknowledgment

References

[1] Goodenough JB, Park K-S. The Li-ion rechargeable battery: a perspective. J Am Chem Soc 2013;135:1167–76.

[2] Høyer KG. The history of alternative fuels in transportation: the case of electric and hybrid cars. Utilities Policy 2008;16:63–71.

[3] Bahrami A, Schierning G, Nielsch K. Waste recycling in thermoelectric materials. Adv Energy Mater 2020;10:1904159.

[4] Xie X-C, Huang K-J, Wu X. Metal–organic framework derived hollow materials for electrochemical energy storage. J Mater Chem A 2018;6:6754–71.

[5] Wang F-T, Wang Y-H, Xu J, Huang K-J, Liu Z-h, Lu Y-f, et al. Boosting performance of self-powered biosensing device with high-energy enzyme biofuel cells and cruciform DNA. Nano Energy 2020;68:104310.

[6] Shuai H, Li J, Jiang F, Zhang X, Xu L, Hu J, et al. Electrochemically intercalated intermediate induced exfoliation of few-layer MoS$_2$ from molybdenite for long-life sodium storage. Sci China Mater 2021;64:115–27.

[7] Wang C, Li X, Zhao Y, Banis MN, Liang J, Li X, et al. Manipulating interfacial nanostructure to achieve high-performance all-solid-state lithium-ion batteries. Small Methods 2019;3:1900261.

[8] Shuai H, Ge P, Hong W, Li S, Hu J, Hou H, et al. Electrochemically Exfoliated Phosphorene–Graphene Hybrid for Sodium-Ion Batteries. Small Methods 2019;3: 1800328.

[9] Bahrami A, Soltani N, Pech-Canul MI, Gutiérrez CA. Development of metal-matrix composites from industrial/agricultural waste materials and their derivatives. Crit Rev Environ Sci Technol 2016;46:143–208. https://doi.org/10.1080/10643389.2015.1077067.

[10] Lu L, Han X, Li J, Hua J, Ouyang M. A review on the key issues for lithium-ion battery management in electric vehicles. J Power Sources 2013;226:272–88.

[11] Daniel C. Lithium ion batteries and their manufacturing challenges. The Bridge (Washington, DC) 2015;45:21–4.

[12] Slater MD, Kim D, Lee E, Johnson CS. Sodium-ion batteries. Adv Funct Mater 2013;23:947–58.

[13] Inagaki M. Applications of graphite intercalation compounds. J Mater Res 1989;4: 1560–8.

[14] Li J, Rui B, Wei W, Nie P, Chang L, Le Z, et al. Nanosheets assembled layered MoS$_2$/MXene as high performance anode materials for potassium ion batteries. J Power Sources 2020;449:227481.

[15] Li Y, Lu Y, Adelhelm P, Titirici M-M, Hu Y-S. Intercalation chemistry of graphite: alkali metal ions and beyond. Chem Soc Rev 2019;48:4655–87.

[16] Zhang W, Liu Y, Guo Z. Approaching high-performance potassium-ion batteries via advanced design strategies and engineering. Sci Adv 2019;5:eaav7412.

[17] Dahn JR, Zheng T, Liu Y, Xue J. Mechanisms for lithium insertion in carbonaceous materials. Science 1995;270:590–3.

[18] Zheng T, Liu Y, Fuller E, Tseng S, Von Sacken U, Dahn J. Lithium insertion in high capacity carbonaceous materials. J Electrochem Soc 1995;142:2581–90.

[19] Stephan AM, Kumar TP, Ramesh R, Thomas S, Jeong SK, Nahm KS. Pyrolitic carbon from biomass precursors as anode materials for lithium batteries. Mater Sci Eng: A 2006;430:132–7.

[20] Peng Y-T, Lo C-T. Effect of microstructure and morphology of electrospun ultra-small carbon nanofibers on anode performances for lithium ion batteries. J Electrochem Soc 2015;162:A1085–1A93.

[21] Deng J, Xiong T, Wang H, Zheng A, Wang Y. Effects of cellulose, hemicellulose, and lignin on the structure and morphology of porous carbons. ACS Sustain Chem Eng 2016;4:3750–6.

[22] Yang H, Yan R, Chen H, Lee DH, Zheng C. Characteristics of hemicellulose, cellulose and lignin pyrolysis. Fuel 2007;86:1781–8.

[23] Cagnon B, Py X, Guillot A, Stoeckli F, Chambat G. Contributions of hemicellulose, cellulose and lignin to the mass and the porous properties of chars and steam activated carbons from various lignocellulosic precursors. Bioresour Technol 2009;100:292–8.

[24] Wang F, Song R, Song H, Chen X, Zhou J, Ma Z, et al. Simple synthesis of novel hierarchical porous carbon microspheres and their application to rechargeable lithium-ion batteries. Carbon 2015;81:314–21.

[25] Robertson J. Amorphous carbon. Adv Phys 1986;35:317–74.

[26] Robertson J. Diamond-like amorphous carbon. Mater Sci Eng: R: Reports 2002; 37:129–281.

[27] Seifert G, Kuc A, Heine T. Hexagon preserving carbon nanofoams.Colombo L, Fasolino A, editors. . Computer-based modeling of novel carbon systems and their properties - beyond nanotubes. Dordrecht: Springer; 2010. p. 57–77.

[28] Dennison J, Holtz M, Swain G. Raman spectroscopy of carbon materials. Spectroscopy 1996;11:38–45.

[29] Zhao M-Q, Zhang Q, Huang J-Q, Tian G-L, Nie J-Q, Peng H-J, et al. Unstacked double-layer templated graphene for high-rate lithium–sulphur batteries. Nat Commun 2014;5:3410.

[30] Wu Z-S, Zhou G, Yin L-C, Ren W, Li F, Cheng H-M. Graphene/metal oxide composite electrode materials for energy storage. Nano Energy 2012;1:107–31.

[31] Zhang K, Zhang LL, Zhao X, Wu J. Graphene/polyaniline nanofiber composites as supercapacitor electrodes. Chem Mater 2010;22:1392–401.

[32] Yan J, Wei T, Shao B, Ma F, Fan Z, Zhang M, et al. Electrochemical properties of graphene nanosheet/carbon black composites as electrodes for supercapacitors. Carbon 2010;48:1731–7.

[33] Fan Z, Yan J, Zhi L, Zhang Q, Wei T, Feng J, et al. A three-dimensional carbon nanotube/graphene sandwich and its application as electrode in supercapacitors. Adv Mater 2010;22:3723–8.

[34] Perner A, Vetter J. Lithium-ion batteries for hybrid electric vehicles and battery electric vehiclesScrosati B, Garche J, Tillmetz W, editors. . Advances in Battery Technologies for Electric Vehicles. 1st. Cambridge (UK): Woodhead Publishing; 2015. p. 173–90.

[35] Sagues WJ, Yang J, Monroe N, Han S-D, Vinzant T, Yung M, et al. A simple method for producing bio-based anode materials for lithium-ion batteries. Green Chem 2020;22:7093–108.

[36] Wollbrink A, Volgmann K, Koch J, Kanthasamy K, Tegenkamp C, Li Y, et al. Amorphous, turbostratic and crystalline carbon membranes with hydrogen selectivity. Carbon 2016;106:93–105.

[37] Harris PJ. Structure of non-graphitising carbons. Int Mater Rev 1997;42:206–18.

[38] Randin J-P, Yeager E. Differential capacitance study on the edge orientation of pyrolytic graphite and glassy carbon electrodes. J Electroanal Chem Interfacial Electrochem 1975;58:313–22.

[39] Wang D, Chen J-F, Dai L. Recent Advances in Graphene Quantum Dots for Fluorescence Bioimaging from Cells through Tissues to Animals. Part Part Syst Character 2015;32:515–23.

[40] Sun Y-P, Zhou B, Lin Y, Wang W, Fernando KAS, Pathak P, et al. Quantum-sized carbon dots for bright and colorful photoluminescence. J Am Chem Soc 2006;128: 7756–7.

[41] Huang Z, Shen Y, Li Y, Zheng W, Xue Y, Qin C, et al. Facile synthesis of analogous graphene quantum dots with sp^2 hybridized carbon atom dominant structures and their photovoltaic application. Nanoscale 2014;6:13043–52.

[42] Lim SY, Shen W, Gao Z. Carbon quantum dots and their applications. Chem Soc Rev 2015;44:362–81.

[43] Ort DR, Yocum CF, Heichel IF. Oxygenic photosynthesis: the light reactions. Oxygenic photosynthesis: the light reactions. Dordrecht: Kluwer Academic Publishers; 1996.

[44] Song S, Ma F, Wu G, Ma D, Geng W, Wan J. Facile self-templating large scale preparation of biomass-derived 3D hierarchical porous carbon for advanced supercapacitors. J Mater Chem A 2015;3:18154–62.

[45] Natarajan S, Lee Y-S, Aravindan V. Biomass-derived carbon materials as prospective electrodes for high-energy lithium- and sodium-ion capacitors. Chem – Asian J 2019;14:936–51.

[46] Blaschek HP, Ezeji TC. Science of alternative feedstocks. Corn-based Ethanol in Illinois and the US: University of Illinois 2007:112–28.

[47] Lee S, Speight JG, Loyalka SK. Handbook of alternative fuel technologies. Handbook of alternative fuel technologies. 2nd. Boca Raton: CRC Press; 2018.

[48] Alonso DM, Wettstein SG, Dumesic JA. Bimetallic catalysts for upgrading of biomass to fuels and chemicals. Chem Soc Rev 2012;41:8075–98.

[49] Ma S, He F, Tian D, Zou D, Yan Z, Yang Y, et al. Variations and determinants of carbon content in plants: a global synthesis. Biogeosciences 2018;15:693.

[50] de Neergaard A, Porter JR, Gorissen A. Distribution of assimilated carbon in plants and rhizosphere soil of basket willow (Salix viminalis L.). Plant Soil 2002; 245:307–14.

[51] Daud WMAW, Ali WSW. Comparison on pore development of activated carbon produced from palm shell and coconut shell. Bioresour Technol 2004;93:63–9.

[52] Jahirul MI, Rasul MG, Chowdhury AA, Ashwath N. Biofuels production through biomass pyrolysis—a technological review. Energies 2012;5:4952–5001.

[53] Darmawan S, Wistara NJ, Pari G, Maddu A, Syafii W. Characterization of lignocellulosic biomass as raw material for the production of porous carbon-based materials. BioResources 2016;11:3561–74.

[54] Chen H. Chemical composition and Structure of natural lignocellulose. Biotechnol Lignocellulose: Theory Pract Dordrecht: Springer Netherlands; 2014:25–71.

[55] Domínguez-Robles J, Tamminen T, Liitiä T, Peresin MS, Rodríguez A, Jääskeläinen A-S. Aqueous acetone fractionation of kraft, organosolv and soda lignins. Int J Biol Macromol 2018;106:979–87.

[56] Petrov N, Budinova T, Razvigorova M, Zanzi R, Björnbom E, Minkova V. Preparation of activated carbons from cherry stones, apricot stones and grape seeds for removal of metal ions from water. 2nd Olle Lindstroem symposium on renewable energy - Bioenergy. Stockholm, Sweden 1999. p. 9-11.

[57] Jiang Y, Zhang Z, Zhang Y, Zhou X, Wang L, Yasin A, et al. Bioresource derived porous carbon from cottonseed hull for removal of triclosan and electrochemical application. RSC Adv 2018;8:42405–14.

[58] Xie A, Dai J, Chen X, He J, Chang Z, Yan Y, et al. Hierarchical porous carbon materials derived from a waste paper towel with ultrafast and ultrahigh performance for adsorption of tetracycline. RSC Adv 2016;6:72985–98.

[59] Ma S, He F, Tian D, Zou D, Yan Z, Yang Y, et al. Variations and determinants of carbon content in plants: a global synthesis. Biogeosciences 2018;15:693.

[60] Brebu M, Vasile C. Thermal degradation of lignin—a review. Cellul Chem Technol 2010;44:353.

[61] Mahadevan R, Adhikari S, Shakya R, Wang K, Dayton D, Lehrich M, et al. Effect of alkali and alkaline earth metals on in-situ catalytic fast pyrolysis of lignocellulosic biomass: a microreactor study. Energy Fuels 2016;30:3045–56.

[62] Xing W, Xue JS, Dahn JR. Optimizing pyrolysis of sugar carbons for use as anode materials in lithium-ion batteries. J Electrochem Soc 1996;143:3046–52.

[63] Leth-Espensen A, Glarborg P, Jensen PA. Predicting biomass char yield from high heating rate devolatilization using chemometrics. Energy Fuels 2018;32: 9572–80.

[64] Tao L, Huang Y, Zheng Y, Yang X, Liu C, Di M, et al. Porous carbon nanofiber derived from a waste biomass as anode material in lithium-ion batteries. J Taiwan Inst Chem Eng 2019;95:217–26.

[65] Wang J, Nie P, Ding B, Dong S, Hao X, Dou H, et al. Biomass derived carbon for energy storage devices. J Mater Chem A 2017;5:2411–28.

[66] Nygård HS, Olsen E. Review of thermal processing of biomass and waste in molten salts for production of renewable fuels and chemicals. Int J Low-Carbon Technol 2012;7:318–24.

[67] Yin H, Lu B, Xu Y, Tang D, Mao X, Xiao W, et al. Harvesting capacitive carbon by carbonization of waste biomass in molten salts. Environ Sci Technol 2014;48: 8101–8.

[68] Kleen M, Gellerstedt G. Influence of inorganic species on the formation of polysaccharide and lignin degradation products in the analytical pyrolysis of pulps. J Anal Appl Pyrolysis 1995;35:15–41.

[69] Shang H, Lu Y, Zhao F, Chao C, Zhang B, Zhang H. Preparing high surface area porous carbon from biomass by carbonization in a molten salt medium. RSC Adv 2015;5:75728–34.

[70] Jiang H, Ai N, Wang M, Ji D, Ji J. Experimental study on thermal pyrolysis of biomass in molten salt media. Electrochemistry 2009;77:730–5.

[71] He X, Zeng K, Xie Y, Flamant G, Yang H, Yang X, et al. The effects of temperature and molten salt on solar pyrolysis of lignite. Energy 2019;181:407–16.

[72] Lu B, Hu L, Yin H, Mao X, Xiao W, Wang D. Preparation and application of capacitive carbon from bamboo shells by one step molten carbonates carbonization. Int J Hydrogen Energy 2016;41:18713–20.

[73] Kwapinski W, Byrne CM, Kryachko E, Wolfram P, Adley C, Leahy JJ, et al. Biochar from biomass and waste. Waste Biomass Valorization 2010;1:177–89.

[74] Chowdhury ZZ, Hamid SBA, Das R, Hasan MR, Zain SM, Khalid K, et al. Preparation of carbonaceous adsorbents from lignocellulosic biomass and their use in removal of contaminants from aqueous solution. BioResources 2013;8: 6523–55.

[75] Chen C, Song J, Zhu S, Li Y, Kuang Y, Wan J, et al. Scalable and sustainable approach toward highly compressible, anisotropic, lamellar carbon sponge. Chem 2018;4:544–54.

[76] Zhao Y, Wang L, Huang L, Maximov MY, Jin M, Zhang Y, et al. Biomass-derived oxygen and nitrogen co-doped porous carbon with hierarchical architecture as sulfur hosts for high-performance lithium/sulfur batteries. Nanomaterials 2017;7: 402.

[77] Li X, Sun C, Cai Z, Ge F. High-performance all-solid-state supercapacitor derived from PPy coated carbonized silk fabric. Appl Surf Sci 2019;473:967–75.

[78] Li J, Liu K, Gao X, Yao B, Huo K, Cheng Y, et al. Oxygen-and nitrogen-enriched 3D porous carbon for supercapacitors of high volumetric capacity. ACS Appl Mater Interfaces 2015;7:24622–8.

[79] Gogotsi Y, Presser V. Carbon nanomaterials. Carbon nanomaterials. Boca Raton: CRC Press; 2013.

[80] Zhang F, Ma H, Chen J, Li G-D, Zhang Y, Chen J-S. Preparation and gas storage of high surface area microporous carbon derived from biomass source cornstalks. Bioresour Technol 2008;99:4803–8.

[81] Mauricio MR, da Costa PG, Haraguchi SK, Guilherme MR, Muniz EC, Rubira AF. Synthesis of a microhydrogel composite from cellulose nanowhiskers and starch for drug delivery. Carbohydr Polym 2015;115:715–22.

[82] Sasikala M, Umapathy MJ. Preparation and characterization of pineapple leaf cellulose nanocrystal reinforced gelatin bio-nanocomposite with antibacterial banana leaf extract for application in food packaging. New J Chem 2018;42: 19979–86. https://doi.org/10.1039/C8NJ02973C.

[83] Sheltami RM, Abdullah I, Ahmad I, Dufresne A, Kargarzadeh H. Extraction of cellulose nanocrystals from mengkuang leaves (Pandanus tectorius). Carbohydr Polym 2012;88:772–9. https://doi.org/10.1016/j.carbpol.2012.01.062.

[84] Danial WH, Abdul Majid Z, Mohd Muhid MN, Triwahyono S, Bakar MB, Ramli Z. The reuse of wastepaper for the extraction of cellulose nanocrystals. Carbohydr Polym 2015;118:165–9.

[85] Araujo RA, Rubira AF, Asefa T, Silva R. Metal doped carbon nanoneedles and effect of carbon organization with activity for hydrogen evolution reaction (HER). Carbohydr Polym 2016;137:719–25.

[86] Rouzaud J-N. The multiscale organization as a fingerprint of the formation conditions of carbons; a TEM study. Carbon 2004 : International Conference on Carbon at Brown University, RI, American Carbon Society 2004;4.

[87] McDonald-Wharry JS, Manley-Harris M, Pickering KL. Reviewing, combining, and updating the models for the nanostructure of non-graphitizing carbons produced from oxygen-containing precursors. Energy Fuels 2016;30:7811–26.

[88] Rodríguez-Mirasol J, Cordero T, Rodríguez J. High-temperature carbons from kraft lignin. Carbon 1996;34:43–52.

[89] Sagues WJ, Jain A, Brown D, Aggarwal S, Suarez A, Kollman M, et al. Are lignin-derived carbon fibers graphitic enough? Green Chem 2019;21:4253–65.

[90] Gomez-Martin A, Martinez-Fernandez J, Ruttert M, Heckmann A, Winter M, Placke T, et al. Iron-catalyzed graphitic carbon materials from biomass resources as anodes for lithium-ion batteries. ChemSusChem 2018;11:2776–87.

[91] Yuan J, Giordano C, Antonietti M. Ionic liquid monomers and polymers as precursors of highly conductive, mesoporous, graphitic carbon nanostructures. Chem Mater 2010;22:5003–12.

[92] Xu G, Han J, Ding B, Nie P, Pan J, Dou H, et al. Biomass-derived porous carbon materials with sulfur and nitrogen dual-doping for energy storage. Green Chem 2015;17:1668–74.

[93] Derbyshire F, Presland A, Trimm D. Graphite formation by the dissolution—precipitation of carbon in cobalt, nickel and iron. Carbon 1975;13: 111–3.

[94] Edwards IA, Menendez R, Marsh H. Introduction to carbon science. Butterworth-Heinemann; 2013.

[95] Franklin RE. Crystallite growth in graphitizing and non-graphitizing carbons. Proceed R Soc Lond Ser A Math Phys Eng Sci 1951;209:196–218.

[96] Krishna R, Wade J, Jones AN, Lasithiotakis M, Mummery PM, Marsden BJ. An understanding of lattice strain, defects and disorder in nuclear graphite. Carbon 2017;124:314–33.

[97] Al-Qasir II. Thermal neutron scattering in graphite. Raleigh, North Carolina: North Carolina State University; 2007.

[98] Berl E, Andreas K, Reinhardt L, Herbert W. Über die Natur der aktiven Kohlen. Z Phys Chem 1932;158A:273–89. https://doi.org/10.1515/zpch-1932-15817.

[99] Biscoe J, Warren BE. An X-Ray Study of Carbon Black. J Appl Phys 1942;13: 364–71.

[100] Peng W-G, Strauss M, Pieper T, Kilian H-G. X-ray diffraction and model calculation on carbon blacks. Mol Phys 1993;80:419–29.

[101] Hoerni J, Weigle J. Structure of graphite. Nature 1949;164:1088.

[102] Zhang T, Mao J, Liu X, Xuan M, Bi K, Zhang XL, et al. Pinecone biomass-derived hard carbon anodes for high-performance sodium-ion batteries. RSC Adv 2017;7: 41504–11.

[103] Wang C, Huang J, Qi H, Cao L, Xu Z, Cheng Y, et al. Controlling pseudographtic domain dimension of dandelion derived biomass carbon for excellent sodium-ion storage. J Power Sources 2017;358:85–92.

[104] Lotfabad EM, Ding J, Cui K, Kohandehghan A, Kalisvaart WP, Hazelton M, et al. High-density sodium and lithium ion battery anodes from banana peels. ACS Nano 2014;8:7115–29.

[105] Tuinstra F, Koenig J. Raman spectrum of graphite. J Chem Phys 1970;53: 1126–30. https://doi.org/10.1063/1.1674108.

[106] Eckmann A, Felten A, Mischchenko A, Britnell L, Krupke R, Novoselov KS, et al. Probing the nature of defects in graphene by raman spectroscopy. Nano Lett 2012; 12:3925–30.

[107] Mallet-Ladeira P, Puech P, Toulouse C, Cazayous M, Ratel-Ramond N, Weisbecker P, et al. A Raman study to obtain crystallite size of carbon materials: a better alternative to the Tuinstra–Koenig law. Carbon 2014;80:629–39.

[108] Pan D, Wang S, Zhao B, Wu M, Zhang H, Wang Y, et al. Li storage properties of disordered graphene nanosheets. Chem Mater 2009;21:3136–42.

[109] Pisana S, Lazzeri M, Casiraghi C, Novoselov KS, Geim AK, Ferrari AC, et al. Breakdown of the adiabatic Born–Oppenheimer approximation in graphene. Nat Mater 2007;6:198–201.

[110] Basavalingu B, Moreno JMC, Byrappa K, Gogotsi YG, Yoshimura M. Decomposition of silicon carbide in the presence of organic compounds under hydrothermal conditions. Carbon 2001;39:1763–6.

[111] Maslova O, Ammar M, Guimbretière G, Rouzaud J-N, Simon P. Determination of crystallite size in polished graphitized carbon by Raman spectroscopy. Phys Rev B 2012;86:134205.

[112] Reiche S, Blume R, Zhao XC, Su D, Kunkes E, Behrens M, et al. Reactivity of mesoporous carbon against water – an *in-situ* XPS study. Carbon 2014;77:175–83.

[113] Susi T, Pichler T, Ayala P. X-ray photoelectron spectroscopy of graphitic carbon nanomaterials doped with heteroatoms. Beilstein J Nanotechnol 2015;6:177–92.

[114] Yu Z-L, Xin S, You Y, Yu L, Lin Y, Xu D-W, et al. Ion-catalyzed synthesis of microporous hard carbon embedded with expanded nanographite for enhanced lithium/sodium storage. J Am Chem Soc 2016;138:14915–22.

[115] Leiro J, Heinonen M, Laiho T, Batirev I. Core-level XPS spectra of fullerene, highly oriented pyrolitic graphite, and glassy carbon. J Electron Spectrosc Relat Phenom 2003;128:205–13.

[116] Dwivedi N, Yeo RJ, Satyanarayana N, Kundu S, Tripathy S, Bhatia C. Understanding the role of nitrogen in plasma-assisted surface modification of magnetic recording media with and without ultrathin carbon overcoats. Sci Rep 2015;5:7772.

[117] Blume R, Rosenthal D, Tessonnier J-P, Li H, Knop-Gericke A, Schlögl R. Characterizing graphitic carbon with X-ray photoelectron spectroscopy: A step-by-step approach. ChemCatChem 2015;7:2871–81.

[118] Díaz J, Paolicelli G, Ferrer S, Comin F. Separation of the sp^3 and sp^2 components in the C1s photoemission spectra of amorphous carbon films. Phys Rev B 1996;54: 8064–9. https://doi.org/10.1103/PhysRevB.54.8064.

[119] Kelemen SR, Rose KD, Kwiatek PJ. Carbon aromaticity based on XPS II to II* signal intensity. Appl Surf Sci 1993;64:167–74.

[120] Chen XC, Zhang Y, Merrill LC, Soulen C, Lehmann ML, Schaefer JL, et al. Gel composite electrolyte – an effective way to utilize ceramic fillers in lithium batteries. J Mater Chem A 2021.

[121] Winter M, Besenhard JO, Spahr ME, Novak P. Insertion electrode materials for rechargeable lithium batteries. Adv Mater 1998;10:725–63.

[122] Roberts AD, Li X, Zhang H. Porous carbon spheres and monoliths: morphology control, pore size tuning and their applications as Li-ion battery anode materials. Chem Soc Rev 2014;43:4341–56.

[123] Liang Y, Yang C, Dong H, Li W, Hu H, Xiao Y, et al. Facile synthesis of highly porous carbon from rice husk. ACS Sustain Chem Eng 2017;5:7111–7.

[124] Jain A, Aravindan V, Jayaraman S, Kumar PS, Balasubramanian R, Ramakrishna S, et al. Activated carbons derived from coconut shells as high energy density cathode material for Li-ion capacitors. Sci Rep 2013;3:3002.

[125] Subramanian V, Luo C, Stephan AM, Nahm K, Thomas S, Wei B. Supercapacitors from activated carbon derived from banana fibers. J Phys Chemistry C 2007;111: 7527–31.

[126] Liu D, Yu S, Shen Y, Chen H, Shen Z, Zhao S, et al. Polyaniline coated boron doped biomass derived porous carbon composites for supercapacitor electrode materials. Ind Eng Chem Res 2015;54:12570–9.

[127] Yang T, Qian T, Wang M, Shen X, Xu N, Sun Z, et al. A sustainable route from biomass byproduct okara to high content nitrogen-doped carbon sheets for efficient sodium ion batteries. Adv Mater 2016;28:539–45.

[128] Zhao H, Gao Y, Wang J, Chen C, Chen D, Wang C, et al. Egg yolk-derived phosphorus and nitrogen dual doped nano carbon capsules for high-performance lithium ion batteries. Mater Lett 2016;167:93–7.

[129] Wu J, Zuo L, Song Y, Chen Y, Zhou R, Chen S, et al. Preparation of biomass-derived hierarchically porous carbon/Co$_3$O$_4$ nanocomposites as anode materials for lithium-ion batteries. J Alloys Compd 2016;656:745–52.

[130] Yan L, Yu J, Houston J, Flores N, Luo H. Biomass derived porous nitrogen doped carbon for electrochemical devices. Green Energy Environ 2017;2:84–99.

[131] Duan M, Tian C, Hu Y, Mei A, Rong Y, Xiong Y, et al. Boron-doped graphite for high work function carbon electrode in printable hole-conductor-free mesoscopic perovskite solar cells. ACS Appl Mater Interfaces 2017;9:31721–7.

[132] Qie L, Chen WM, Wang ZH, Shao QG, Li X, Yuan LX, et al. Nitrogen-doped porous carbon nanofiber webs as anodes for lithium ion batteries with a superhigh capacity and rate capability. Adv Mater 2012;24:2047–50.

[133] Chen Y, Li X, Park K, Song J, Hong J, Zhou L, et al. Hollow carbon-nanotube/carbon-nanofiber hybrid anodes for Li-ion batteries. J Am Chem Soc 2013;135: 16280–3.

[134] Li Y, Li Z, Shen PK. Simultaneous formation of ultrahigh surface area and three-dimensional hierarchical porous graphene-like networks for fast and highly stable supercapacitors. Adv Mater 2013;25:2474–80.

[135] Chen Y, Lu Z, Zhou L, Mai Y-W, Huang H. Triple-coaxial electrospun amorphous carbon nanotubes with hollow graphitic carbon nanospheres for high-performance Li ion batteries. Energy Environ Sci 2012;5:7898–902.

[136] Hu C, Wang L, Zhao Y, Ye M, Chen Q, Feng Z, et al. Designing nitrogen-enriched echinus-like carbon capsules for highly efficient oxygen reduction reaction and lithium ion storage. Nanoscale 2014;6:8002–9. https://doi.org/10.1039/C4NR01184H.

[137] Li Z, Xu Z, Tan X, Wang H, Holt CM, Stephenson T, et al. Mesoporous nitrogen-rich carbons derived from protein for ultra-high capacity battery anodes and supercapacitors. Energy Environ Sci 2013;6:871–8.

[138] Qie L, Chen W, Xu H, Xiong X, Jiang Y, Zou F, et al. Synthesis of functionalized 3D hierarchical porous carbon for high-performance supercapacitors. Energy Environ Sci 2013;6:2497–504.

[139] Liang Y, Wu D, Fu R. Carbon microfibers with hierarchical porous structure from electrospun fiber-like natural biopolymer. Sci Rep 2013;3:1119.

[140] Fang B, Kim JH, Kim M-S, Yu J-S. Hierarchical nanostructured carbons with meso–macroporosity: design, characterization, and applications. Acc Chem Res 2013;46:1397–406.

[141] Jayaraman S, Madhavi S, Aravindan V. High energy Li-ion capacitor and battery using graphitic carbon spheres as an insertion host from cooking oil. J Mater Chem A 2018;6:3242–8.

[142] Tao L, Huang Y, Yang X, Zheng Y, Liu C, Di M, et al. Flexible anode materials for lithium-ion batteries derived from waste biomass-based carbon nanofibers: I. Effect of carbonization temperature. RSC Adv 2018;8:7102–9.

[143] Wang H, Yu W, Shi J, Mao N, Chen S, Liu W. Biomass derived hierarchical porous carbons as high-performance anodes for sodium-ion batteries. Electrochim Acta 2016;188:103–10.

[144] Zhu Y, Chen M, Li Q, Yuan C, Wang C. A porous biomass-derived anode for high-performance sodium-ion batteries. Carbon 2018;129:695–701.

[145] Cao L, Wang X, Meziani MJ, Lu F, Wang H, Luo PG, et al. Carbon dots for multiphoton bioimaging. J Am Chem Soc 2007;129:11318–9.

[146] Yang S-T, Cao L, Luo PG, Lu F, Wang X, Wang H, et al. Carbon dots for optical imaging in vivo. J Am Chem Soc 2009;131:11308–9.

[147] Feng J, Wang W-J, Hai X, Yu Y-L, Wang J-H. Green preparation of nitrogen-doped carbon dots derived from silkworm chrysalis for cell imaging. J Mater Chem B 2016;4:387–93.

[148] Wang Z, Liu J, Wang W, Wei Z, Wang F, Gong P, et al. Photoluminescent carbon quantum dot grafted silica nanoparticles directly synthesized from rice husk biomass. J Mater Chem B 2017;5:4679–89.

[149] Chunduri LAA, Kurdekar A, Patnaik S, Dev BV, Rattan TM, Kamisetti V. Carbon quantum dots from coconut husk: evaluation for antioxidant and cytotoxic activity. Mater Focus 2016;5:55–61.

[150] Zhao S, Lan M, Zhu X, Xue H, Ng T-W, Meng X, et al. Green synthesis of bifunctional fluorescent carbon dots from garlic for cellular imaging and free radical scavenging. ACS Appl Mater Interfaces 2015;7:17054–60.

[151] Yu J, Song N, Zhang Y-K, Zhong S-X, Wang A-J, Chen J. Green preparation of carbon dots by Jinhua bergamot for sensitive and selective fluorescent detection of Hg^{2+} and Fe^{3+}. Sens Actuators, B 2015;214:29–35.

[152] Sahu S, Behera B, Maiti TK, Mohapatra S. Simple one-step synthesis of highly luminescent carbon dots from orange juice: application as excellent bio-imaging agents. Chem Commun 2012;48:8835–7.

[153] Du F, Zhang M, Li X, Li J, Jiang X, Li Z, et al. Economical and green synthesis of bagasse-derived fluorescent carbon dots for biomedical applications. Nanotechnology 2014;25:315702.

[154] Wang C, Wu D, Wang H, Gao Z, Xu F, Jiang K. Biomass derived nitrogen-doped hierarchical porous carbon sheets for supercapacitors with high performance. J Colloid Interface Sci 2018;523:133–43.

[155] Hao Y, Zhang X, Yang Q, Chen K, Guo J, Zhou D, et al. Highly porous defective carbons derived from seaweed biomass as efficient electrocatalysts for oxygen reduction in both alkaline and acidic media. Carbon 2018;137:93–103.

[156] Hoang VC, Nguyen LH, Gomes VG. High efficiency supercapacitor derived from biomass based carbon dots and reduced graphene oxide composite. J Electroanal Chem 2019;832:87–96.

[157] Pawlak R, Liu X, Ninova S, D'Astolfo P, Drechsel C, Sangtarash S, et al. Bottom-up synthesis of nitrogen-doped porous graphene nanoribbons. J Am Chem Soc 2020; 142:12568–73.

[158] Chao D, Zhu C, Xia X, Liu J, Zhang X, Wang J, et al. Graphene quantum dots coated VO$_2$ arrays for highly durable electrodes for Li and Na ion batteries. Nano Lett 2015;15:565–73.

[159] Jing M, Wang J, Hou H, Yang Y, Zhang Y, Pan C, et al. Carbon quantum dot coated Mn$_3$O$_4$ with enhanced performances for lithium-ion batteries. J Mater Chem A 2015;3:16824–30.

[160] Liu F, Wang Y, Zhang Y, Lin J, Su Q, Shi J, et al. A Facile Carbon Quantum Dot-Modified Reduction Approach Towards Tunable Sb@CQDs Nanoparticles for High Performance Sodium Storage. Batteries & Supercaps 2020;3:463–9.

[161] Zhang W, Xu T, Liu Z, Wu N-L, Wei M. Hierarchical TiO$_{2−x}$ imbedded with graphene quantum dots for high-performance lithium storage. Chem Commun 2018;54:1413–6.

[162] Yi X, He W, Zhang X, Yue Y, Yang G, Wang Z, et al. Graphene-like carbon sheet/Fe$_3$O$_4$ nanocomposites derived from soda papermaking black liquor for high performance lithium ion batteries. Electrochim Acta 2017;232:550–60.

[163] Peng H, Travas-Sejdic J. Simple aqueous solution route to luminescent carbogenic dots from carbohydrates. Chem Mater 2009;21:5563–5.

[164] Javed M, Saqib ANS, Ata-ur-Rehman, Ali B, Faizan M, Anang DA, et al. Carbon quantum dots from glucose oxidation as a highly competent anode material for lithium and sodium-ion batteries. Electrochim Acta 2019;297:250–7. https://doi.org/10.1016/j.electacta.2018.11.167.

[165] Monthioux M, Kuznetsov VL. Who should be given the credit for the discovery of carbon nanotubes? Carbon 2006;44:1621–3.

[166] Kanchi S, Ahmed S, Sabela MI, Hussain CM. Nanomaterials: Biomedical, Environmental, and Engineering Applications. John Wiley & Sons; 2018.

[167] Al-Saleh MH, Sundararaj U. Review of the mechanical properties of carbon nanofiber/polymer composites. Composites, Part A 2011;42:2126–42.

[168] Xie X, Goodell B, Qian Y, Daniel G, Zhang D, Nagle DC, et al. A method for producing carbon nanotubes directly from plant materials. Forest Prod J 2009;59.

[169] Goodell B, Xie X, Qian Y, Daniel G, Peterson M, Jellison J. Carbon nanotubes produced from natural cellulosic materials. J Nanosci Nanotechnol 2008;8: 2472–4.

[170] Gao Z, Song N, Zhang Y, Schwab Y, He J, Li X. Carbon nanotubes derived from yeast-fermented wheat flour and their energy storage application. ACS Sustain Chem Eng 2018;6:11386–96.

[171] De las Casas C, Li W. A review of application of carbon nanotubes for lithium ion battery anode material. J Power Sources 2012;208:74–85.

[172] Kawasaki S, Hara T, Iwai Y, Suzuki Y. Metallic and semiconducting single-walled carbon nanotubes as the anode material of Li ion secondary battery. Mater Lett 2008;62:2917–20.

[173] Landi BJ, Ganter MJ, Cress CD, DiLeo RA, Raffaelle RP. Carbon nanotubes for lithium ion batteries. Energy Environ Sci 2009;2:638–54.

[174] Dobrota AS, Pašti IA, Mentus SV, Skorodumova NV. A DFT study of the interplay between dopants and oxygen functional groups over the graphene basal plane–implications in energy-related applications. PCCP 2017;19:8530–40.

[175] Shimoda H, Gao B, Tang X, Kleinhammes A, Fleming L, Wu Y, et al. Lithium intercalation into opened single-wall carbon nanotubes: storage capacity and electronic properties. Phys Rev Lett 2001;88:015502.

[176] Chen WX, Lee JY, Liu Z. The nanocomposites of carbon nanotube with Sb and SnSb$_{0.5}$ as Li-ion battery anodes. Carbon 2003;41:959–66. https://doi.org/10.1016/S0008-6223(02)00425-6.

[177] Claye AS, Fischer JE, Huffman CB, Rinzler AG, Smalley RE. Solid-state electrochemistry of the Li single wall carbon nanotube system. J Electrochem Soc 2000;147:2845–52.

[178] Frackowiak E, Gautier S, Gaucher H, Bonnamy S, Beguin F. Electrochemical storage of lithium in multiwalled carbon nanotubes. Carbon 1999;37:61–9.

[179] Liu Y, Artyukhov VI, Liu M, Harutyunyan AR, Yakobson BI. Feasibility of lithium storage on graphene and its derivatives. J Phys Chem Lett 2013;4:1737–42.

[180] Lu Y-F, Lo S-T, Lin J-C, Zhang W, Lu J-Y, Liu F-H, et al. Nitrogen-doped graphene sheets grown by chemical vapor deposition: synthesis and influence of nitrogen impurities on carrier transport. ACS Nano 2013;7:6522–32.

[181] Meunier V, Kephart J, Roland C, Bernholc J. Ab initio investigations of lithium diffusion in carbon nanotube systems. Phys Rev Lett 2002;88:075506.

[182] Eom J, Kwon H-S, Liu J, Zhou O. Lithium insertion into purified and etched multi-walled carbon nanotubes synthesized on supported catalysts by thermal CVD. Carbon 2004;42:2589–96.

[183] Eom J, Kim D, Kwon H. Effects of ball-milling on lithium insertion into multi-walled carbon nanotubes synthesized by thermal chemical vapour deposition. J Power Sources 2006;157:507–14.

[184] Li Y, Hu YS, Titirici MM, Chen L, Huang X. Hard carbon microtubes made from renewable cotton as high-performance anode material for sodium-ion batteries. Adv Energy Mater 2016;6:1600659.

[185] Alves AK, Bergmann CP, Berutti FA. Novel synthesis and characterization of nanostructured materials. Novel synthesis and characterization of nanostructured materials. Berlin, Heidelberg: Springer-Verlag; 2013.

[186] Shin HJ, Kim KK, Benayad A, Yoon SM, Park HK, Jung IS, et al. Efficient reduction of graphite oxide by sodium borohydride and its effect on electrical conductance. Adv Funct Mater 2009;19:1987–92.

[187] Bagri A, Mattevi C, Acik M, Chabal YJ, Chhowalla M, Shenoy VB. Structural evolution during the reduction of chemically derived graphene oxide. Nat Chem 2010;2:581.

[188] Xing Y, Wang Y, Zhou C, Zhang S, Fang B. Simple synthesis of mesoporous carbon nanofibers with hierarchical nanostructure for ultrahigh lithium storage. ACS Appl Mater Interfaces 2014;6:2561–7.

[189] Fang B, Kim M-S, Kim JH, Lim S, Yu J-S. Ordered multimodal porous carbon with hierarchical nanostructure for high Li storage capacity and good cycling performance. J Mater Chem 2010;20:10253–9.

[190] Luo W, Schardt J, Bommier C, Wang B, Razink J, Simonsen J, et al. Carbon nanofibers derived from cellulose nanofibers as a long-life anode material for rechargeable sodium-ion batteries. J Mater Chem A 2013;1:10662–6.

[191] Jayaraman S, Singh G, Madhavi S, Aravindan V. Elongated graphitic hollow nanofibers from vegetable oil as prospective insertion host for constructing advanced high energy Li-ion capacitor and battery. Carbon 2018;134:9–14.

[192] Hiramatsu M, Hori M. Carbon nanowalls: synthesis and emerging applications. Carbon nanowalls: synthesis and emerging applications. Wien: Springer-Verlag; 2010.

[193] Terrones M. Science and technology of the twenty-first century: synthesis, properties, and applications of carbon nanotubes. Annu Rev Mater Res 2003;33: 419–501.

[194] Pollak E, Geng B, Jeon K-J, Lucas IT, Richardson TJ, Wang F, et al. The interaction of Li+ with single-layer and few-layer graphene. Nano Lett 2010;10:3386–8.

[195] Yao F, Gunes F, Ta HQ, Lee SM, Chae SJ, Sheem KY, et al. Diffusion mechanism of lithium ion through basal plane of layered graphene. J Am Chem Soc 2012;134: 8646–54.

[196] Radhakrishnan G, Cardema JD, Adams PM, Kim HI, Foran B. Fabrication and electrochemical characterization of single and multi-layer graphene anodes for lithium-ion batteries. J Electrochem Soc 2012;159:A752–AA61.

[197] Ji K, Han J, Hirata A, Fujita T, Shen Y, Ning S, et al. Lithium intercalation into bilayer graphene. Nat Commun 2019;10:275.

[198] Russo P, Xiao M, Zhou NY. Carbon nanowalls: A new material for resistive switching memory devices. Carbon 2017;120:54–62.

[199] Yang Y, Tang D-M, Zhang C, Zhang Y, Liang Q, Chen S, et al. Protrusions" or "holes" in graphene: which is the better choice for sodium ion storage? Energy Environ Sci 2017;10:979–86.

[200] Chen F, Yang J, Bai T, Long B, Zhou X. Facile synthesis of few-layer graphene from biomass waste and its application in lithium ion batteries. J Electroanal Chem 2016;768:18–26.

[201] Barthlott W, Neinhuis C, Cutler D, Ditsch F, Meusel I, Theisen I, et al. Classification and terminology of plant epicuticular waxes. Bot J Linnean Soc 1998;126:237–60. https://doi.org/10.1111/j.1095-8339.1998.tb02529.x.

[202] Pambou E, Li Z, Campana M, Hughes A, Clifton L, Gutfreund P, et al. Structural features of reconstituted wheat wax films. J R Soc, Interface 2016;13:20160396.

[203] Li X, Han C, Chen X, Shi C. Preparation and performance of straw based activated carbon for supercapacitor in non-aqueous electrolytes. Microporous Mesoporous Mater 2010;131:303–9.

[204] Sheng Z-H, Shao L, Chen J-J, Bao W-J, Wang F-B, Xia X-H. Catalyst-free synthesis of nitrogen-doped graphene via thermal annealing graphite oxide with melamine and its excellent electrocatalysis. ACS Nano 2011;5:4350–8.

[205] Hou J, Cao C, Idrees F, Ma X. Hierarchical porous nitrogen-doped carbon nanosheets derived from silk for ultrahigh-capacity battery anodes and supercapacitors. ACS Nano 2015;9:2556–64.

[206] Yun YS, Cho SY, Shim J, Kim BH, Chang SJ, Baek SJ, et al. Microporous carbon nanoplates from regenerated silk proteins for supercapacitors. Adv Mater 2013; 25:1993–8.

[207] Etacheri V, Hong CN, Pol VG. Upcycling of packing-peanuts into carbon microsheet anodes for lithium-ion batteries. Environ Sci Technol 2015;49: 11191–8.

[208] Zhou X, Chen F, Bai T, Long B, Liao Q, Ren Y, et al. Interconnected highly graphitic carbon nanosheets derived from wheat stalk as high performance anode materials for lithium ion batteries. Green Chem 2016;18:2078–88.

[209] Zhu Z, Liang F, Zhou Z, Zeng X, Wang D, Dong P, et al. Expanded biomass-derived hard carbon with ultra-stable performance in sodium-ion batteries. J Mater Chem A 2018;6:1513–22.

[210] Hooch Antink W, Choi Y, Seong Kd, Kim JM, Piao Y. Recent progress in porous graphene and reduced graphene oxide-based nanomaterials for electrochemical energy storage devices. Adv Mater Interfaces 2018;5:1701212. https://doi.org/10.1002/admi.201701212.

[211] Soltani N, Bahrami A, Pech-Canul M, González L. Review on the physicochemical treatments of rice husk for production of advanced materials. Chem Eng J 2015; 264:899–935.

[212] Xing Y, Fang B, Bonakdarpour A, Zhang S, Wilkinson DP. Facile fabrication of mesoporous carbon nanofibers with unique hierarchical nanoarchitecture for electrochemical hydrogen storage. Int J Hydrogen Energy 2014;39:7859–67.

[213] Xing Y, Wang S, Fang B, Song G, Wilkinson DP, Zhang S. N-doped hollow urchin-like anatase TiO2@C composite as a novel anode for Li-ion batteries. J Power Sources 2018;385:10–7.

[214] Zhang D, Zhao J, Feng C, Zhao R, Sun Y, Guan T, et al. Scalable synthesis of hierarchical macropore-rich activated carbon microspheres assembled by carbon nanoparticles for high rate performance supercapacitors. J Power Sources 2017; 342:363–70.

[215] Bahrami A, Simon U, Soltani N, Zavareh S, Schmidt J, Pech-Canul MI, et al. Eco-fabrication of hierarchical porous silica monoliths by ice-templating of rice husk ash. Green Chem 2017;19:188–95.

[216] Soltani N, Simon U, Bahrami A, Wang X, Selve S, Epping JD, et al. Macroporous polymer-derived SiO2/SiOC monoliths freeze-cast from polysiloxane and amorphous silica derived from rice husk. J Eur Ceram Soc 2017;37:4809–20.

[217] Jayaraman S, Jain A, Ulaganathan M, Edison E, Srinivasan MP, Balasubramanian R, et al. Li-ion vs. Na-ion capacitors: A performance evaluation with coconut shell derived mesoporous carbon and natural plant based hard carbon. Chem Eng J 2017;316:506–13.

[218] Sennu P, Arun N, Madhavi S, Aravindan V, Lee Y-S. All carbon based high energy lithium-ion capacitors from biomass: The role of crystallinity. J Power Sources 2019;414:96–102.

[219] Wenzel S, Hara T, Janek J, Adelhelm P. Room-temperature sodium-ion batteries: Improving the rate capability of carbon anode materials by templating strategies. Energy Environ Sci 2011;4:3342–5.

[220] Lee J, Chen Y-M, Zhu Y, Vogt BD. Tuning SEI formation on nanoporous carbon–titania composite sodium ion batteries anodes and performance with subtle processing changes. RSC Adv 2015;5:99329–38.

[221] Mao C, Wood M, David L, An SJ, Sheng Y, Du Z, et al. Selecting the best graphite for long-life, high-energy Li-Ion batteries. J Electrochem Soc 2018;165: A1837–1A45.

[222] Flandrois S, Simon B. Carbon materials for lithium-ion rechargeable batteries. Carbon 1999;37:165–80.

[223] Li Z, Bommier C, Chong ZS, Jian Z, Surta TW, Wang X, et al. Mechanism of Na-ion storage in hard carbon anodes revealed by heteroatom doping. Adv Energy Mater 2017;7:1602894.

[224] Chuenchom L, Kraehnert R, Smarsly BM. Recent progress in soft-templating of porous carbon materials. Soft Matter 2012;8:10801–12.

[225] Zhao X, Su F, Yan Q, Guo W, Bao XY, Lv L, et al. Templating methods for preparation of porous structures. J Mater Chem 2006;16:637–48.

[226] Strubel P, Thieme S, Biemelt T, Helmer A, Oschatz M, Brückner J, et al. ZnO hard templating for synthesis of hierarchical porous carbons with tailored porosity and high performance in lithium-sulfur battery. Adv Funct Mater 2015;25:287–97.

[227] Ryoo R, Joo SH, Jun S. Synthesis of highly ordered carbon molecular sieves via template-mediated structural transformation. J Phys Chem B 1999;103:7743–6.

[228] Jun S, Joo SH, Ryoo R, Kruk M, Jaroniec M, Liu Z, et al. Synthesis of new, nanoporous carbon with hexagonally ordered mesostructure. J Am Chem Soc 2000;122:10712–3.

[229] Fang B, Kim M, Hwang S, Yu J-S. Colloid-imprinted carbon with tailored nanostructure as an unique anode electrocatalyst support for formic acid oxidation. Carbon 2008;46:876–83.

[230] Fang B, Kim JH, Kim M-S, Bonakdarpour A, Lam A, Wilkinson DP, et al. Fabrication of hollow core carbon spheres with hierarchical nanoarchitecture for ultrahigh electrical charge storage. J Mater Chem 2012;22:19031–8.

[231] Kim JH, Fang B, Kim M-S, Yoon SB, Bae T-S, Ranade DR, et al. Facile synthesis of bimodal porous silica and multimodal porous carbon as an anode catalyst support in proton exchange membrane fuel cell. Electrochim Acta 2010;55:7628–33.

[232] Gogotsi Y, Nikitin A, Ye H, Zhou W, Fischer JE, Yi B, et al. Nanoporous carbide-derived carbon with tunable pore size. Nat Mater 2003;2:591–4.

[233] Oschatz M, Borchardt L, Pinkert K, Thieme S, Lohe MR, Hoffmann C, et al. Hierarchical carbide-derived carbon foams with advanced mesostructure as a versatile electrochemical energy-storage material. Adv Energy Mater 2014;4: 1300645.

[234] Morishita T, Soneda Y, Tsumura T, Inagaki M. Preparation of porous carbons from thermoplastic precursors and their performance for electric double layer capacitors. Carbon 2006;44:2360–7.

[235] Zhu C, Akiyama T. Cotton derived porous carbon via an MgO template method for high performance lithium ion battery anodes. Green Chem 2016;18:2106–14.

[236] Sun Q, Jiang T, Zhao G, Shi J. Porous Carbon material based on biomass prepared by MgO template method and ZnCl2 activation method as electrode for high performance supercapacitor. Int J Electrochem Sci 2019;14:1–14.

[237] Muller A, Scrivener K, Gajewicz A, McDonald P. Use of bench-top NMR to measure the density, composition and desorption isotherm of C–S–H in cement paste. Microporous Mesoporous Mater 2013;178:99–103.

[238] Unur E, Brutti S, Panero S, Scrosati B. Nanoporous carbons from hydrothermally treated biomass as anode materials for lithium ion batteries. Microporous Mesoporous Mater 2013;174:25–33.

[239] Morishita T, Suzuki R, Tsumura T, Habazaki H, Inagaki M. Preparation of mesoporous carbons by carbonization of the mixtures of poly (vinyl alcohol) with magnesium salts. TANSO 2006;2006:220–6.

[240] Nie P, Le Z, Chen G, Liu D, Liu X, Wu HB, et al. Graphene caging silicon particles for high-performance lithium-ion batteries. Small 2018;14:1800635.

[241] Xie Y, Kocaefe D, Chen C, Kocaefe Y. Review of research on template methods in preparation of nanomaterials. J. Nanomater 2016;2016.

[242] Thomas A, Goettmann F, Antonietti M. Hard templates for soft materials: creating nanostructured organic materials. Chem Mater 2008;20:738–55.

[243] Gonçalves TAP, Marcati CR, Scheel-Ybert R. The effect of carbonization on wood structure of dalbergia violacea, stryphnodendron polyphyllum, tapirira guianensis, Vochysia Tucanorum, and pouteria torta from the Brazilian Cerrado. IAWA J 2012;33:73–90.

[244] Märkle T, Rösch M. Experiments on the effects of carbonization on some cultivated plant seeds. Vegetation History Archaeobotany 2008;17:257–63.

[245] Braadbaart F, van Bergen PF. Digital imaging analysis of size and shape of wheat and pea upon heating under anoxic conditions as a function of the temperature. Vegetation History Archaeobotany 2005;14:67–75.

[246] Parameswaran N, Stamm A. Strukturelle und chemo-physikalische Veränderungen bei der Verkohlung von vier tropischen Laubhölzern. Holzforschung 1983;37:309–20.

[247] Wood AR, Garg R, Justus K, Cohen-Karni T, LeDuc P, Russell AJ. Intact mangrove root electrodes for desalination. RSC Adv 2019;9:4735–43.

[248] Momodu D, Madito M, Barzegar F, Bello A, Khaleed A, Olaniyan O, et al. Activated carbon derived from tree bark biomass with promising material properties for supercapacitors. J Solid State Electrochem 2017;21:859–72.

[249] Zhang F, Wang K-X, Li G-D, Chen J-S. Hierarchical porous carbon derived from rice straw for lithium ion batteries with high-rate performance. Electrochem Commun 2009;11:130–3.

[250] Ding J, Wang H, Li Z, Kohandehghan A, Cui K, Xu Z, et al. Carbon nanosheet frameworks derived from peat moss as high performance sodium ion battery anodes. ACS Nano 2013;7:11004–15.

[251] Um JH, Ahn C-Y, Kim J, Jeong M, Sung Y-E, Cho Y-H, et al. From grass to battery anode: agricultural biomass hemp-derived carbon for lithium storage. RSC Adv 2018;8:32231–40.

[252] Demir-Cakan R, Baccile N, Antonietti M, Titirici M-M. Carboxylate-rich carbonaceous materials via one-step hydrothermal carbonization of glucose in the presence of acrylic acid. Chem Mater 2009;21:484–90.

[253] Dou X, Hasa I, Hekmatfar M, Diemant T, Behm RJ, Buchholz D, et al. Pectin, Hemicellulose, or Lignin? Impact of the biowaste source on the performance of hard carbons for sodium-ion batteries. ChemSusChem 2017;10:2668–76.

[254] Mestre AS, Carvalho AP. Nanoporous carbons synthesis: an old story with exciting new chapters. editor. In: Hcine Ghrib T, editor. Porosity, Process, Technologies and Applications. London, UK: IntechOpen; 2018. p. 37–68.

[255] Ateş F, Özcan Ö. Preparation and characterization of activated carbon from poplar sawdust by chemical activation: comparison of different activating agents and carbonization temperature. Eur J Eng Res Sci 2018;3:6–11.

[256] Marsh H, Yan DS, O'Grady TM, Wennerberg A. Formation of active carbons from cokes using potassium hydroxide. Carbon 1984;22:603–11.

[257] Chen L, Zhang Y, Lin C, Yang W, Meng Y, Guo Y, et al. Hierarchically porous nitrogen-rich carbon derived from wheat straw as an ultra-high-rate anode for lithium ion batteries. J Mater Chem A 2014;2:9684–90.

[258] Fingolo AC, Bettini J, da Silva Cavalcante M, Pereira MP, Bufon CCB, Santhiago M, et al. Boosting electrical conductivity of sugarcane cellulose and lignin biocarbons through annealing under isopropanol vapor. ACS Sustain Chem Eng 2020;8:7002–10.

[259] Dai J, Yuan J. Modulating the electronic and magnetic structures of P-doped graphene by molecule doping. J Phys: Condens Matter 2010;22:225501.

[260] Luo Z, Lim S, Tian Z, Shang J, Lai L, MacDonald B, et al. Pyridinic N doped graphene: synthesis, electronic structure, and electrocatalytic property. J Mater Chem 2011;21:8038–44.

[261] Ma X, Ning G, Qi C, Xu C, Gao J. Phosphorus and nitrogen dual-doped few-layered porous graphene: a high-performance anode material for lithium-ion batteries. ACS Appl Mater Interfaces 2014;6:14415–22.

[262] Wang H, Zhang C, Liu Z, Wang L, Han P, Xu H, et al. Nitrogen-doped graphene nanosheets with excellent lithium storage properties. J Mater Chem 2011;21:5430–4.

[263] Pumera M. Heteroatom modified graphenes: electronic and electrochemical applications. J Mater Chem C 2014;2:6454–61.

[264] Li Z, Bommier C, Chong ZS, Jian Z, Surta TW, Wang X, et al. Mechanism of Na-ion storage in hard carbon anodes revealed by heteroatom doping. Adv Energy Mater 2017;7:1602894.

[265] Alvin S, Chandra C, Kim J. Extended plateau capacity of phosphorus-doped hard carbon used as an anode in Na- and K-ion batteries. Chem Eng J 2020;391:123576.

[266] Vassilev SV, Baxter D, Andersen LK, Vassileva CG. An overview of the chemical composition of biomass. Fuel 2010;89:913–33.

[267] Suzuki T, Nakajima H, Ikenaga N-o, Oda H, Miyake T. Effect of mineral matters in biomass on the gasification rate of their chars. Biomass Convers Biorefinery 2011;1:17–28.

[268] Gudka B, Jones JM, Lea-Langton AR, Williams A, Saddawi A. A review of the mitigation of deposition and emission problems during biomass combustion through washing pre-treatment. J Energy Inst 2016;89:159–71.

[269] Wang X, Sun G, Routh P, Kim D-H, Huang W, Chen P. Heteroatom-doped graphene materials: syntheses, properties and applications. Chem Soc Rev 2014;43:7067–98.

[270] Wu P, Du P, Zhang H, Cai C. Microscopic effects of the bonding configuration of nitrogen-doped graphene on its reactivity toward hydrogen peroxide reduction reaction. PCCP 2013;15:6920–8.

[271] Poh HL, Šimek P, Sofer Z, Tomandl I, Pumera M. Boron and nitrogen doping of graphene via thermal exfoliation of graphite oxide in a BF_3 or NH_3 atmosphere: contrasting properties. J Mater Chem A 2013;1:13146–53.

[272] Li D, Zhang L, Chen H, Ding L-x, Wang S, Wang H. Nitrogen-doped bamboo-like carbon nanotubes: promising anode materials for sodium-ion batteries. Chem Commun 2015;51:16045–8.

[273] Wu J, Pan Z, Zhang Y, Wang B, Peng H. The recent progress of nitrogen-doped carbon nanomaterials for electrochemical batteries. J Mater Chem A 2018;6:12932–44.

[274] Wang C, Wu D, Wang H, Gao Z, Xu F, Jiang K. A green and scalable route to yield porous carbon sheets from biomass for supercapacitors with high capacity. J Mater Chem A 2018;6:1244–54.

[275] Zhang D, Wang G, Xu L, Lian J, Bao J, Zhao Y, et al. Defect-rich N-doped porous carbon derived from soybean for high rate lithium-ion batteries. Appl Surf Sci 2018;451:298–305.

[276] Long W, Fang B, Ignaszak A, Wu Z, Wang Y-J, Wilkinson D. Biomass-derived nanostructured carbons and their composites as anode materials for lithium ion batteries. Chem Soc Rev 2017;46:7176–90.

[277] Hao E, Liu W, Liu S, Zhang Y, Wang H, Chen S, et al. Rich sulfur doped porous carbon materials derived from ginkgo leaves for multiple electrochemical energy storage devices. J Mater Chem A 2017;5:2204–14.

[278] Zhang S, Zheng M, Lin Z, Li N, Liu Y, Zhao B, et al. Activated carbon with ultrahigh specific surface area synthesized from natural plant material for lithium–sulfur batteries. J Mater Chem A 2014;2:15889–96.

[279] Guo D, Wei H, Chen X, Liu M, Ding F, Yang Z, et al. 3D hierarchical nitrogen-doped carbon nanoflower derived from chitosan for efficient electrocatalytic oxygen reduction and high performance lithium–sulfur batteries. J Mater Chem A 2017;5:18193–206.

[280] Li Y, Wang G, Wei T, Fan Z, Yan P. Nitrogen and sulfur co-doped porous carbon nanosheets derived from willow catkin for supercapacitors. Nano Energy 2016;19:165–75.

[281] Obernberger I, Brunner T, Bärnthaler G. Chemical properties of solid biofuels—significance and impact. Biomass Bioenergy 2006;30:973–82.

[282] Gislum R, Griffith S. Tiller production and development in perennial ryegrass in relation to nitrogen use. J Plant Nutr 2005;27:2135–48.

[283] Lim TK. Edible medicinal and non-medicinal plants. Edible medicinal and non-medicinal plants. Dordrecht: Springer; 2012.

[284] Zhao L, Fan LZ, Zhou MQ, Guan H, Qiao S, Antonietti M, et al. Nitrogen-containing hydrothermal carbons with superior performance in supercapacitors. Adv Mater 2010;22:5202–6.

[285] Sun F, Gao J, Zhu Y, Pi X, Wang L, Liu X, et al. A high performance lithium ion capacitor achieved by the integration of a Sn-C anode and a biomass-derived microporous activated carbon cathode. Sci Rep 2017;7:40990.

[286] Candelaria SL, Garcia BB, Liu D, Cao G. Nitrogen modification of highly porous carbon for improved supercapacitor performance. J Mater Chem 2012;22:9884–9.

[287] Kai D, Tan MJ, Chee PL, Chua YK, Yap YL, Loh XJ. Towards lignin-based functional materials in a sustainable world. Green Chem 2016;18:1175–200.

[288] Jin J, Ding J, Klett A, Thies MC, Ogale AA. Carbon fibers derived from fractionated–solvated lignin precursors for enhanced mechanical performance. ACS Sustain Chem Eng 2018;6:14135–42.

[289] Tenhaeff WE, Rios O, More K, McGuire MA. Highly Robust lithium ion battery anodes from lignin: an abundant, renewable, and low-cost material. Adv Funct Mater 2014;24:86–94.

[290] Zhao H, Wang Q, Deng Y, Shi Q, Qian Y, Wang B, et al. Preparation of renewable lignin-derived nitrogen-doped carbon nanospheres as anodes for lithium-ion batteries. RSC Adv 2016;6:77143–50.

[291] Yang J, Wang Y, Luo J, Chen L. Facile preparation of self-standing hierarchical porous nitrogen-doped carbon fibers for supercapacitors from plant protein–lignin electrospun fibers. ACS Omega 2018;3:4647–56.

[292] Du L, Wu W, Luo C, Xu D, Guo H, Wang R, et al. Lignin-derived nitrogen-doped porous carbon as a high-rate anode material for sodium ion batteries. J Electrochem Soc 2019;166:A423–A48.

[293] Zhao H, Wang Q, Deng Y, Shi Q, Qian Y, Wang B, et al. Preparation of renewable lignin-derived nitrogen-doped carbon nanospheres as anodes for lithium-ion batteries. RSC Adv 2016;6:77143–50.

[294] Graglia M, Pampel J, Hantke T, Fellinger T-P, Esposito D. Nitro lignin-derived nitrogen-doped carbon as an efficient and sustainable electrocatalyst for oxygen reduction. ACS Nano 2016;10:4364–71.

[295] Endo K, Tatsumi T. Nitrogen doped fluorinated amorphous carbon thin films grown by plasma enhanced chemical vapor deposition for low dielectric constant interlayer dielectrics. Appl Phys Lett 1996;68:3656–8.

[296] Li X-j, Yu X-x, Liu J-y, Fan X-d, Zhang K, Cai H-b, et al. Synthesis of nitrogen-doped graphene via thermal annealing graphene with urea. Chin J Chem Phys 2012;25:325.

[297] Soudani N, Najar-Souissi S, Abderkader-Fernandez VK, Ouederni A. Effects of nitrogen plasma treatment on the surface characteristics of olive stone-based activated carbon. Environ Technol 2017;38:956–66.

[298] Belgacem AB, Hinkov I, Yahia SB, Brinza O, Farhat S. Arc discharge boron nitrogen doping of carbon nanotubes. Mater Today Commun 2016;8:183–95.

[299] Schneidermann C, Jäckel N, Oswald S, Giebeler L, Presser V, Borchardt L. Solvent-free mechanochemical synthesis of nitrogen-doped nanoporous carbon for electrochemical energy storage. ChemSusChem 2017;10:2416–24.

[300] Yang L, Jiang S, Zhao Y, Zhu L, Chen S, Wang X, et al. Boron-doped carbon nanotubes as metal-free electrocatalysts for the oxygen reduction reaction. Angew Chem Int Ed 2011;50:7132–5.

[301] Ryu J, Park M, Cho J. Boron and nitrogen co-doped porous carbon materials derived from orange peels as an electrocatalyst for the all-vanadium redox flow batteries. Meeting Abstracts: The Electrochemical Society 2015;MA2015-03:652.

[302] Chen M-H, Wu G-T, Zhu G-M, You J-K, Lin Z-G. Characterization and electrochemical investigation of boron-doped mesocarbon microbead anode materials for lithium ion batteries. J Solid State Electrochem 2002;6:420–7.

[303] Tanaka U, Sogabe T, Sakagoshi H, Ito M, Tojo T. Anode property of boron-doped graphite materials for rechargeable lithium-ion batteries. Carbon 2001;39:931–6.

[304] Hagio T, Nakamizo M, Kobayashi K. Studies on X-ray diffraction and Raman spectra of B-doped natural graphite. Carbon 1989;27:259–63.

[305] Ling Z, Wang Z, Zhang M, Yu C, Wang G, Dong Y, et al. Sustainable synthesis and assembly of biomass-derived B/N co-doped carbon nanosheets with ultrahigh aspect ratio for high-performance supercapacitors. Adv Funct Mater 2016;26: 111–9.

[306] Xia Q, Yang H, Wang M, Yang M, Guo Q, Wan L, et al. High energy and high power lithium-ion capacitors based on boron and nitrogen dual-doped 3D carbon nanofibers as both cathode and anode. Adv Energy Mater 2017;7:1701336.

[307] Monteiro F, Larrude D, Maia da Costa M, Terrazos L, Capaz RB, Freire Jr F. Production and characterization of boron-doped single wall carbon nanotubes. J Phys Chem C 2012;116:3281–5.

[308] Shirasaki T, Derré A, Ménétrier M, Tressaud A, Flandrois S. Synthesis and characterization of boron-substituted carbons. Carbon 2000;38:1461–7.

[309] Cermignani W, Paulson TE, Onneby C, Pantano CG. Synthesis and characterization of boron-doped carbons. Carbon 1995;33:367–74.

[310] Endo M, Kim C, Nishimura K, Fujino T, Miyashita K. Recent development of carbon materials for Li ion batteries. Carbon 2000;38:183–97.

[311] Agnoli S, Favaro M. Doping graphene with boron: a review of synthesis methods, physicochemical characterization, and emerging applications. J Mater Chem A 2016;4:5002–25.

[312] Dahn JR, Reimers JN, Sleigh AK, Tiedje T. Density of states in graphite from electrochemical measurements on $Li_x(C_{1-z}B_z)_6$. Phys Rev B 1992;45:3773–7. https://doi.org/10.1103/PhysRevB.45.3773.

[313] Alvin S, Cahyadi HS, Hwang J, Chang W, Kwak SK, Kim J. Revealing the intercalation mechanisms of lithium, sodium, and potassium in hard carbon. Adv Energy Mater 2020;10:2000283.

[314] Chae Y-J, Kim S-O, Lee JK. Employment of boron-doped carbon materials for the anode materials of lithium ion batteries. J Alloys Compd 2014;582:420–7.

[315] Lu X, Chen L. Boron-doped carbon nano-/microballs from orthoboric acid-starch: preparation, characterization, and lithium ion storage properties. J Nanomater 2018;2018:4987340.

[316] Wu F, Dong R, Bai Y, Li Y, Chen G, Wang Z, et al. Phosphorus-doped hard carbon nanofibers prepared by electrospinning as an anode in sodium-ion batteries. ACS Appl Mater Interfaces 2018;10:21335–42.

[317] Ma C, Deng C, Liao X, He Y, Ma Z, Xiong H. Nitrogen and phosphorus codoped porous carbon framework as anode material for high rate lithium-ion batteries. ACS Appl Mater Interfaces 2018;10:36969–75.

[318] Jeon T, Lee S, Jung SC. Boron-, nitrogen-, aluminum-, and phosphorus-doped graphite electrodes for non-lithium ion batteries. Curr Appl Phys 2020;20: 988–93.

[319] Wu J, Yang Z, Sun Q, Li X, Strasser P, Yang R. Synthesis and electrocatalytic activity of phosphorus-doped carbon xerogel for oxygen reduction. Electrochim Acta 2014;127:53–60.

[320] Wang B, Yu L, Zhang J, Pu Y, Zhang H, Li W. Phosphorus-doped carbon supports enhance gold-based catalysts for acetylene hydrochlorination. RSC Adv 2014;4: 15877–85.

[321] Liu Q, Zhou Y, Chen S, Wang Z, Hou H, Zhao F. Cellulose-derived nitrogen and phosphorus dual-doped carbon as high performance oxygen reduction catalyst in microbial fuel cell. J Power Sources 2015;273:1189–93.

[322] Hou H, Shao L, Zhang Y, Zou G, Chen J, Ji X. Large-area carbon nanosheets doped with phosphorus: a high-performance anode material for sodium-ion batteries. Adv Sci 2017;4:1600243.

[323] Lü H-Y, Zhang X-H, Wan F, Liu D-S, Fan C-Y, Xu H-M, et al. Flexible P-doped carbon cloth: vacuum-sealed preparation and enhanced Na-storage properties as binder-free anode for sodium ion batteries. ACS Appl Mater Interfaces 2017;9: 12518–27.

[324] Yi J, Qing Y, Wu C, Zeng Y, Wu Y, Lu X, et al. Lignocellulose-derived porous phosphorus-doped carbon as advanced electrode for supercapacitors. J Power Sources 2017;351:130–7.

[325] Li Z, Ma L, Surta TW, Bommier C, Jian Z, Xing Z, et al. High capacity of hard carbon anode in Na-ion batteries unlocked by PO_x doping. ACS Energy Lett 2016; 1:395–401. https://doi.org/10.1021/acsenergylett.6b00172.

[326] Tao H, Du S, Zhang F, Xiong L, Zhang Y, Ma H, et al. Achieving a high-performance carbon anode through the P–O bond for lithium-ion batteries. ACS Appl Mater Interfaces 2018;10:34245–53.

[327] Lu K, Lu S, Gu T, Zheng X, Ke K, Li X, et al. Onium salts-derived B and P dual-doped carbon microspheres as anode material for high-performance sodium-ion batteries. Electrochem Commun 2019;103:22–6.

[328] Xing X, Liu J, Wang W, Chen Z, Yixuan F. Application of phosphorus-doped sunflower disc-based activated carbon in anode materials for lithium ion batteries. J Process Eng 2019;19:434–9.

[329] Han SS, Yu TH, Merinov BV, Van Duin AC, Yazami R, Goddard III WA. Unraveling structural models of graphite fluorides by density functional theory calculations. Chem Mater 2010;22:2142–54.

[330] Zbořil R, Karlický F, Bourlinos AB, Steriotis TA, Stubos AK, Georgakilas V, et al. Graphene fluoride: a stable stoichiometric graphene derivative and its chemical conversion to graphene. Small 2010;6:2885–91.

[331] Wasalathilake KC, Ayoko GA, Yan C. Effects of heteroatom doping on the performance of graphene in sodium-ion batteries: a density functional theory investigation. Carbon 2018;140:276–85.

[332] Robinson JT, Burgess JS, Junkermeier CE, Badescu SC, Reinecke TL, Perkins FK, et al. Properties of fluorinated graphene films. Nano Lett 2010;10:3001–5.

[333] Feng W, Long P, Feng Y, Li Y. Two-dimensional fluorinated graphene: synthesis, structures, properties and applications. Adv Sci 2016;3:1500413.

[334] Nakajima T, Koh M, Gupta V, Žemva B, Lutar K. Electrochemical behavior of graphite highly fluorinated by high oxidation state complex fluorides and elemental fluorine. Electrochim Acta 2000;45:1655–61.

[335] Sun X, Zhang Y, Song P, Pan J, Zhuang L, Xu W, et al. Fluorine-doped carbon blacks: highly efficient metal-free electrocatalysts for oxygen reduction reaction. ACS Catal 2013;3:1726–9.

[336] Kim J, Zhou R, Murakoshi K, Yasuda S. Advantage of semi-ionic bonding in fluorine-doped carbon materials for the oxygen evolution reaction in alkaline media. RSC Adv 2018;8:14152–6.

[337] Di Vittorio S, Dresselhaus M, Dresselhaus G. A model for disorder in fluorine-intercalated graphite. J Mater Res 1993;8:1578–85.

[338] Liu Y, Jiang L, Wang H, Wang H, Jiao W, Chen G, et al. A brief review for fluorinated carbon: synthesis, properties and applications. Nanotechnol Rev 2019;8:573–86.

[339] Gupta V, Nakajima T, Ohzawa Y, Iwata H. Electrochemical characteristics and structures of surface-fluorinated graphites with different particle sizes for lithium ion secondary batteries. J Fluorine Chem 2001;112:233–40.

[340] Gong YJ, Pyo S, Kim H, Cho J, Yun H, Kim H, et al. Advanced Li metal anode by fluorinated metathesis on conjugated carbon networks. Energy Environ Sci 2021; 14:940–54.

[341] Lee C, Han Y-J, Seo YD, Nakabayashi K, Miyawaki J, Santamaría R, et al. C_4F_8 plasma treatment as an effective route for improving rate performance of natural/synthetic graphite anodes in lithium ion batteries. Carbon 2016;103:28–35.

[342] Zhao Y, Yang L, Ma C, Han G. One-step fabrication of fluorine-doped graphite derived from a low-grade microcrystalline graphite ore for potassium-ion batteries. Energy Fuels 2020;34:8993–9001.

[343] Wang P, Qiao B, Du Y, Li Y, Zhou X, Dai Z, et al. Fluorine-doped carbon particles derived from lotus petioles as high-performance anode materials for sodium-ion batteries. J Phys Chem C 2015;119:21336–44.

[344] Zheng F, Yang Y, Chen Q. High lithium anodic performance of highly nitrogen-doped porous carbon prepared from a metal-organic framework. Nat Commun 2014;5:5261.

[345] Raj CR, Samanta A, Noh SH, Mondal S, Okajima T, Ohsaka T. Emerging new generation electrocatalysts for the oxygen reduction reaction. J. Mater. Chem. A 2016;4:11156–78.

[346] Xu A, Shi L, Zeng L, Zhao T. First-principle investigations of nitrogen-, boron-, phosphorus-doped graphite electrodes for vanadium redox flow batteries. Electrochim Acta 2019;300:389–95.

[347] Xie J, Zhao X, Wu M, Li Q, Wang Y, Yao J. Metal-free fluorine-doped carbon electrocatalyst for CO_2 reduction outcompeting hydrogen evolution. Angew Chem Int Ed 2018;57:9640–4.

[348] Serraon ACF, Del Rosario JAD, Abel Chuang P-Y, Chong MN, Morikawa Y, Padama AAB, et al. Alkaline earth atom doping-induced changes in the electronic and magnetic properties of graphene: a density functional theory study. RSC Adv 2021;11:6268–83.

[349] Toh RJ, Poh HL, Sofer Z, Pumera M. Transition metal (Mn, Fe, Co, Ni)-doped graphene hybrids for electrocatalysis. Chem Asian J 2013;8:1295–300.

[350] McRae E, Maréché JF. c-axis conductivity and conductivity anisotropy in graphite intercalation compounds. J Mater Res 1988;3:75–86.

[351] Kaskhedikar NA, Maier J. Lithium storage in carbon nanostructures. Adv Mater 2009;21:2664–80.

[352] Kaneko T, Saito R. First-principles study on interlayer state in alkali and alkaline earth metal atoms intercalated bilayer graphene. Surf Sci 2017;665:1–9.

[353] Chapman J. Alkali metal doped graphene: superconductivity, structural, magnetic and optical properties. The University of Manchester (United Kingdom); 2015.

[354] Matsumoto R, Arakawa M, Yoshida H, Akuzawa N. Alkali-metal-graphite intercalation compounds prepared from flexible graphite sheets exhibiting high air stability and electrical conductivity. Synth Met 2012;162:2149–54.

[355] Cahen S, El-Hajj I, Speyer L, Berger P, Medjahdi G, Lagrange P, et al. Original synthesis route of bulk binary superconducting graphite intercalation compounds with strontium, barium and ytterbium. New J Chem 2020;44:10050–5.

[356] Guerard D, Chaabouni M, Lagrange P, El Makrini M, Herold A. Insertion de metaux alcalino-terreux dans le graphite. Carbon 1980;18:257–64.

[357] Marsh H, Murdie N, Edwards AS, Boehm HP. In: Thrower PA, editor. Chemistry & Physics of Carbon, 20. New York: Marcel Dekker; 1987. p. 213.

[358] Hérinckx C, Perret R, Ruland W. Interstitial compounds of potassium with carbon fibres. Nature 1968;220:63–4. https://doi.org/10.1038/220063a0.

[359] Halpin MK, Jenkins GM. Interaction of glassy carbon with alkali metal vapours. Proceed R Soc Lond Ser A, Math Phys Sci 1969;313:421–31.

[360] Guerard D, Herold A. Intercalation of lithium into graphite and other carbons. Carbon 1975;13:337–45.

[361] Sato K, Noguchi M, Demachi A, Oki N, Endo M. A mechanism of lithium storage in disordered carbons. Science 1994;264:556.

[362] Shi C, Hu L, Hou J, Guo K, Zhai T, Li H. Alkali metal boosted atom rearrangement in amorphous carbon towards crystalline graphitic belt skeleton for high performance supercapacitors. Energy Storage Mater 2018;15:82–90.

[363] McNamara KW, Ayyappan P, Rajagopalan R, Chen JG, Foley HC. Localized crystallization of polyfurfuryl alcohol derived carbon by alkali metals. Carbon 2013;56:109–20.

[364] Wu F, Liu L, Yuan Y, Li Y, Bai Y, Li T, et al. Expanding interlayer spacing of hard carbon by natural K^+ doping to boost Na-ion storage. ACS Appl Mater Interfaces 2018;10:27030–8.

[365] Obrovac MN, Zhao X, Burke LT, Dunlap RA. Reversible lithium insertion in catalytically graphitized sugar carbon. Electrochem Commun 2015;60:221–4.

[366] Li Y, Hu J, Wang Z, Yang K, Huang W, Cao B, et al. Low-temperature catalytic graphitization to enhance Na-ion transportation in carbon electrodes. ACS Appl Mater Interfaces 2019;11:24164–71.

[367] Makrini ME, Guérard D, Lagrange P, Hérold A. Insertion de lanthanoides dans le graphite. Carbon 1980;18:203–9.

[368] Liu X, Wang CZ, Yao YX, Lu WC, Hupalo M, Tringides MC, et al. Bonding and charge transfer by metal adatom adsorption on graphene. Phys Rev B 2011;83: 235411.

[369] Chung DDL. A review of exfoliated graphite. J Mater Sci 2016;51:554–68.

[370] Hoffmann V, Rodriguez Correa C, Sautter D, Maringolo E, Kruse A. Study of the electrical conductivity of biobased carbonaceous powder materials under moderate pressure for the application as electrode materials in energy storage technologies. GCB Bioenergy 2019;11:230–48.

[371] Giraudet J, Claves D, Hamwi A. Transition metals oxyfluorides intercalated into graphite: new synthesis route and electrochemical properties. Synth Met 2001; 118:57–63.

[372] Zhong W, Chen J, Zhang P, Deng L, Yao L, Ren X, et al. Air plasma etching towards rich active sites in Fe/N-porous carbon for the oxygen reduction reaction with superior catalytic performance. J Mater Chem A 2017;5:16605–10.

[373] Cai S, Meng Z, Tang H, Wang Y, Tsiakaras P. 3D Co-N-doped hollow carbon spheres as excellent bifunctional electrocatalysts for oxygen reduction reaction and oxygen evolution reaction. Appl Catal, B 2017;217:477–84.

[374] Lee YJ, Jung JC, Park S, Seo JG, Baeck S-H, Yoon JR, et al. Nano-sized Ni-doped carbon aerogel for supercapacitor. J Nanosci Nanotechnol 2011;11:6528–32.

[375] Sung C-M, Tai M-F. Reactivities of transition metals with carbon: implications to the mechanism of diamond synthesis under high pressure. Int J Refract Met Hard Mater 1997;15:237–56.

[376] Yan Q, Li J, Zhang X, Hassan EB, Wang C, Zhang J, et al. Catalytic graphitization of kraft lignin to graphene-based structures with four different transitional metals. J Nanopart Res 2018;20:223.

[377] Maldonado-Hódar FJ, Moreno-Castilla C, Rivera-Utrilla J, Hanzawa Y, Yamada Y. Catalytic graphitization of carbon aerogels by transition metals. Langmuir 2000; 16:4367–73.

[378] Hunter RD, Rowlandson JL, Smales GJ, Pauw BR, Ting VP, Kulak A, et al. The effect of precursor structure on porous carbons produced by iron-catalyzed graphitization of biomass. Mater Adv 2020;1:3281–91.

[379] Balach J, Singh HK, Gomoll S, Jaumann T, Klose M, Oswald S, et al. Synergistically enhanced polysulfide chemisorption using a flexible hybrid separator with N and S dual-doped mesoporous carbon coating for advanced lithium–sulfur batteries. ACS Appl Mater Interfaces 2016;8:14586–95.

[380] Wang Q, Gao C, Zhang W, Luo S, Zhou M, Liu Y, et al. Biomorphic carbon derived from corn husk as a promising anode materials for potassium ion battery. Electrochim Acta 2019;324:134902.

[381] Yuan C, Liu X, Jia M, Luo Z, Yao J. Facile preparation of N-and O-doped hollow carbon spheres derived from poly (o-phenylenediamine) for supercapacitors. J Mater Chem A 2015;3:3409–15.

[382] Qin D, Liu Z, Zhao Y, Xu G, Zhang F, Zhang X. A sustainable route from corn stalks to N, P-dual doping carbon sheets toward high performance sodium-ion batteries anode. Carbon 2018;130:664–71.

[383] Zhao G, Shi L, Xu J, Yan X, Zhao T. Role of phosphorus in nitrogen, phosphorus dual-doped ordered mesoporous carbon electrocatalyst for oxygen reduction reaction in alkaline media. Int J Hydrogen Energy 2018;43:1470–8.

[384] Zhang Y, Li L, Hong W, Qiu T, Xu L, Zou G, et al. Influence of P doping on Na and K storage properties of N-rich carbon nanosheets. Mater Chem Phys 2019;236: 121809.

[385] Shanmugam S, Nachimuthu S, Subramaniam V. DFT study of adsorption of ions on doped and defective graphene. Materials Today Communications 2020;22: 100714.

[386] Bommier C, Ji X, Greaney PA. Electrochemical properties and theoretical capacity for sodium storage in hard carbon: Insights from first principles calculations. Chem Mater 2018;31:658–77.

[387] Share K, Cohn AP, Carter R, Rogers B, Pint CL. Role of nitrogen-doped graphene for improved high-capacity potassium ion battery anodes. ACS Nano 2016;10: 9738–44.

[388] Yoshio M, Wang H, Fukuda K, Abe T, Ogumi Z. Soft carbon-coated hard carbon beads as a lithium-ion battery anode material. Chem Lett 2003;32:1130–1.

[389] Lian Y, Xin W, Zhang M, Li Y, Yang L, Guo Y, et al. Low-content Ni-doped CoS_2 embedded within N, P-codoped biomass-derived carbon spheres for enhanced lithium/sodium storage. J Mater Sci 2019;54:8504–14.

[390] Li H, Wang Q, Shi L, Chen L, Huang X. Nanosized SnSb alloy pinning on hard non-graphitic carbon spherules as anode materials for a Li ion battery. Chem Mater 2002;14:103–8.

[391] Yang R, Wang Z, Liu J, Chen L. Nano Co_3O_4 particles embedded in porous hard carbon spherules as anode material for Li-ion batteries. Electrochem Solid-State Lett 2004;7:A496–9. https://doi.org/10.1149/1.1819861.

[392] Guo B, Shu J, Tang K, Bai Y, Wang Z, Chen L. Nano-Sn/hard carbon composite anode material with high-initial coulombic efficiency. J Power Sources 2008;177: 205–10.

[393] Cheng H, Garcia-Araez N, Hector AL, Soulé S. Synthesis of hard carbon-TiN/TiC composites by reacting cellulose with TiCl4 followed by carbothermal nitridation/reduction. Inorg Chem 2019;58:5776–86.

[394] Jian Z, Hwang S, Li Z, Hernandez AS, Wang X, Xing Z, et al. Hard–soft composite carbon as a long-cycling and high-rate anode for potassium-ion batteries. Adv Funct Mater 2017;27:1700324.

[395] Nie P, Le Z, Chen G, Liu D, Liu X, Wu HB, et al. Graphene caging silicon particles for high-performance lithium-ion batteries. Small 2018;14:1800635.

[396] Jeong S, Li X, Zheng J, Yan P, Cao R, Jung HJ, et al. Hard carbon coated nano-Si/ graphite composite as a high performance anode for Li-ion batteries. J Power Sources 2016;329:323–9.

[397] Noh M, Kwon Y, Lee H, Cho J, Kim Y, Kim MG. Amorphous carbon-coated tin anode material for lithium secondary battery. Chem Mater 2005;17:1926–9.

[398] Ge C, Fan Z, Zhang J, Qiao Y, Wang J, Ling L. Novel hard carbon/graphite composites synthesized by a facile in situ anchoring method as high-performance anodes for lithium-ion batteries. RSC Adv 2018;8:34682–9.

[399] Yang Z, Zhang J, Kintner-Meyer MC, Lu X, Choi D, Lemmon JP, et al. Electrochemical energy storage for green grid. Chem Rev 2011;111:3577–613.

[400] Ge P, Fouletier M. Electrochemical intercalation of sodium in graphite. Solid State Ion 1988;28:1172–5.

[401] Moriwake H, Kuwabara A, Fisher CA, Ikuhara Y. Why is sodium-intercalated graphite unstable? RSC Adv 2017;7:36550–4.

[402] Nobuhara K, Nakayama H, Nose M, Nakanishi S, Iba H. First-principles study of alkali metal-graphite intercalation compounds. J Power Sources 2013;243:585–7.

[403] Liu Y, Merinov BV, Goddard WA. Origin of low sodium capacity in graphite and generally weak substrate binding of Na and Mg among alkali and alkaline earth metals. Proc Natl Acad Sci 2016;113:3735–9.

[404] Xu Y-S, Duan S-Y, Sun Y-G, Bin D-S, Tao X-S, Zhang D, et al. Recent developments in electrode materials for potassium-ion batteries. J Mater Chem A 2019;7: 4334–52.

[405] Gaddam RR, Yang D, Narayan R, Raju K, Kumar NA, Zhao X. Biomass derived carbon nanoparticle as anodes for high performance sodium and lithium ion batteries. Nano Energy 2016;26:346–52.

[406] Luo W, Wan J, Ozdemir B, Bao W, Chen Y, Dai J, et al. Potassium ion batteries with graphitic materials. Nano Lett 2015;15:7671–7.

[407] Maibach J, Jeschull F, Brandell D, Edström K, Valvo M. Surface layer evolution on graphite during electrochemical sodium-tetraglyme co-intercalation. ACS Appl Mater Interfaces 2017;9:12373–81.

[408] Yamada Y, Yamada A. Superconcentrated electrolytes for lithium batteries. J Electrochem Soc 2015;162:A2406–2A23.

[409] Wen Y, He K, Zhu Y, Han F, Xu Y, Matsuda I, et al. Expanded graphite as superior anode for sodium-ion batteries. Nat Commun 2014;5:4033.

[410] Jache B, Adelhelm P. Use of graphite as a highly reversible electrode with superior cycle life for sodium-ion batteries by making use of co-intercalation phenomena. Angew Chem Int Ed 2014;53:10169–73.

[411] Moon H, Mandai T, Tatara R, Ueno K, Yamazaki A, Yoshida K, et al. Solvent activity in electrolyte solutions controls electrochemical reactions in Li-ion and Li-sulfur batteries. J Phys Chem C 2015;119:3957–70.

[412] Nie M, Abraham DP, Seo DM, Chen Y, Bose A, Lucht BL. Role of solution structure in solid electrolyte interphase formation on graphite with $LiPF_6$ in propylene carbonate. J Phys Chem C 2013;117:25381–9.

[413] Buqa H, Würsig A, Goers D, Hardwick LJ, Holzapfel M, Novák P, et al. Behaviour of highly crystalline graphites in lithium-ion cells with propylene carbonate containing electrolytes. J Power Sources 2005;146:134–41.

[414] Jung SC, Kang Y-J, Han Y-K. Origin of excellent rate and cycle performance of Na$^+$-solvent cointercalated graphite vs. poor performance of Li$^+$-solvent case. Nano Energy 2017;34:456–62.

[415] Kim H, Yoon G, Lim K, Kang K. A comparative study of graphite electrodes using the co-intercalation phenomenon for rechargeable Li, Na and K batteries. Chem Commun 2016;52:12618–21.

[416] Yoon G, Kim H, Park I, Kang K. Conditions for reversible Na intercalation in graphite: theoretical studies on the interplay among guest ions, solvent, and graphite host. Adv Energy Mater 2017;7:1601519.

[417] Kim H, Hong J, Park YU, Kim J, Hwang I, Kang K. Sodium storage behavior in natural graphite using ether-based electrolyte systems. Adv Funct Mater 2015;25: 534–41.

[418] Xu Z-L, Yoon G, Park K-Y, Park H, Tamwattana O, Kim SJ, et al. Tailoring sodium intercalation in graphite for high energy and power sodium ion batteries. Nat Commun 2019;10:2598.

[419] Klein F, Jache B, Bhide A, Adelhelm P. Conversion reactions for sodium-ion batteries. PCCP 2013;15:15876–87.

[420] Zhong Y, Xia X, Shi F, Zhan J, Tu J, Fan HJ. Transition metal carbides and nitrides in energy storage and conversion. Adv Sci 2016;3:1500286.

[421] Wang L, Yang J, Li J, Chen T, Chen S, Wu Z, et al. Graphite as a potassium ion battery anode in carbonate-based electrolyte and ether-based electrolyte. J Power Sources 2019;409:24–30.

[422] Li L, Liu L, Hu Z, Lu Y, Liu Q, Jin S, et al. Understanding high-rate K$^+$-solvent Co-intercalation in natural graphite for potassium-ion batteries. Angew Chem Int Ed 2020;59:12917–24.

[423] Wu X, Leonard DP, Ji X. Emerging non-aqueous potassium-ion batteries: challenges and opportunities. Chem Mater 2017;29:5031–42.

[424] Qiu S, Xiao L, Sushko ML, Han KS, Shao Y, Yan M, et al. Manipulating adsorption–insertion mechanisms in nanostructured carbon materials for high-efficiency sodium ion storage. Adv Energy Mater 2017;7:1700403.

[425] Cao Y, Xiao L, Sushko ML, Wang W, Schwenzer B, Xiao J, et al. Sodium ion insertion in hollow carbon nanowires for battery applications. Nano Lett 2012;12: 3783–7.

[426] Xiao B, Rojo T, Li X. Hard carbon as sodium-ion battery anodes: progress and challenges. ChemSusChem 2019;12:133–44.

[427] Komaba S, Murata W, Ishikawa T, Yabuuchi N, Ozeki T, Nakayama T, et al. Electrochemical Na insertion and solid electrolyte interphase for hard-carbon

electrodes and application to Na-ion batteries. Adv Funct Mater 2011;21: 3859–67.

[428] Ponrouch A, Goñi A, Palacín MR. High capacity hard carbon anodes for sodium ion batteries in additive free electrolyte. Electrochem Commun 2013;27:85–8.

[429] Eshetu GG, Grugeon S, Kim H, Jeong S, Wu L, Gachot G, et al. Comprehensive insights into the reactivity of electrolytes based on sodium ions. ChemSusChem 2016;9:462–71.

[430] Chen C, Wang Z, Zhang B, Miao L, Cai J, Peng L, et al. Nitrogen-rich hard carbon as a highly durable anode for high-power potassium-ion batteries. Energy Storage Mater 2017;8:161–8. https://doi.org/10.1016/j.ensm.2017.05.010.

[431] Wang T, Su D, Shanmukaraj D, Rojo T, Armand M, Wang G. Electrode materials for sodium-ion batteries: considerations on crystal structures and sodium storage mechanisms. Electrochem Energy Rev 2018;1:200–37.

[432] Ohzuku T, Iwakoshi Y, Sawai K. Formation of lithium-graphite intercalation compounds in nonaqueous electrolytes and their application as a negative electrode for a lithium ion (shuttlecock) cell. J Electrochem Soc 1993;140:2490.

[433] Jian Z, Luo W, Ji X. Carbon electrodes for K-ion batteries. J Am Chem Soc 2015; 137:11566–9.

[434] Zhang S, Ding MS, Xu K, Allen J, Jow TR. Understanding solid electrolyte interface film formation on graphite electrodes. Electrochem Solid-State Lett 2001;4:A206–2A8.

[435] Gallagher KG, Dees DW, Jansen AN, Abraham DP, Kang S-H. A volume averaged approach to the numerical modeling of phase-transition intercalation electrodes presented for Li$_x$C$_6$. J Electrochem Soc 2012;159:A2029–2A37.

[436] Shellikeri A, Watson V, Adams D, Kalu E, Read J, Jow T, et al. Investigation of pre-lithiation in graphite and hard-carbon anodes using different lithium source structures. J Electrochem Soc 2017;164:A3914–3A24.

[437] Boesenberg U, Sokaras D, Nordlund D, Weng T-C, Gorelov E, Richardson TJ, et al. Electronic structure changes upon lithium intercalation into graphite–Insights from *ex situ* and *operando* x-ray Raman spectroscopy. Carbon 2019;143:371–7.

[438] Euchner H, Vinayan BP, Reddy MA, Fichtner M, Groß A. Alkali metal insertion into hard carbon – the full picture. J Mater Chem A 2020;8:14205–13.

[439] Beltrop K, Beuker S, Heckmann A, Winter M, Placke T. Alternative electrochemical energy storage: potassium-based dual-graphite batteries. Energy Environ Sci 2017;10:2090–4. https://doi.org/10.1039/C7EE01535F.

[440] Zhao J, Zou X, Zhu Y, Xu Y, Wang C. Electrochemical intercalation of potassium into graphite. Adv Funct Mater 2016;26:8103–10.

[441] Share K, Cohn AP, Carter RE, Pint CL. Mechanism of potassium ion intercalation staging in few layered graphene from in situ Raman spectroscopy. Nanoscale 2016;8:16435–9.

[442] Novák P, Ufheil J, Buqa H, Krumeich F, Spahr ME, Goers D, et al. The importance of the active surface area of graphite materials in the first lithium intercalation. J Power Sources 2007;174:1082–5.

[443] Verma P, Maire P, Novák P. A review of the features and analyses of the solid electrolyte interphase in Li-ion batteries. Electrochim Acta 2010;55:6332–41.

[444] An SJ, Li J, Daniel C, Mohanty D, Nagpure S, Wood III DL. The state of understanding of the lithium-ion-battery graphite solid electrolyte interphase (SEI) and its relationship to formation cycling. Carbon 2016;105:52–76.

[445] Naylor AJ, Carboni M, Valvo M, Younesi R. Interfacial reaction mechanisms on graphite anodes for K-ion batteries. ACS Appl Mater Interfaces 2019;11: 45636–45.

[446] Aurbach D, Levi MD, Levi E, Schechter A. Failure and stabilization mechanisms of graphite electrodes. J Phys Chem B 1997;101:2195–206.

[447] Kang S-H, Abraham D, Xiao A, Lucht BL. Investigating the solid electrolyte interphase using binder-free graphite electrodes. J Power Sources 2008;175: 526–32.

[448] Besenhard J, Winter M, Yang J, Biberacher W. Filming mechanism of lithium-carbon anodes in organic and inorganic electrolytes. J Power Sources 1995;54: 228–31.

[449] Elizabeth I, Mathur R, Maheshwari P, Singh B, Gopukumar S. Development of SnO$_2$/multiwalled carbon nanotube paper as free standing anode for lithium ion batteries (LIB). Electrochim Acta 2015;176:735–42.

[450] Hong K-l, Qie L, Zeng R, Yi Z-q, Zhang W, Wang D, et al. Biomass derived hard carbon used as a high performance anode material for sodium ion batteries. J Mater ChemA 2014;2:12733–8.

[451] Lu P, Li C, Schneider EW, Harris SJ. Chemistry, impedance, and morphology evolution in solid electrolyte interphase films during formation in lithium ion batteries. J Phys Chem C 2014;118:896–903.

[452] Nie M, Chalasani D, Abraham DP, Chen Y, Bose A, Lucht BL. Lithium ion battery graphite solid electrolyte interphase revealed by microscopy and spectroscopy. J Phys Chem C 2013;117:1257–67.

[453] Kim S-P, Van Duin AC, Shenoy VB. Effect of electrolytes on the structure and evolution of the solid electrolyte interphase (SEI) in Li-ion batteries: a molecular dynamics study. J Power Sources 2011;196:8590–7.

[454] Ganesh P, Kent P, Jiang D-e. Solid–electrolyte interphase formation and electrolyte reduction at Li-ion battery graphite anodes: Insights from first-principles molecular dynamics. J Phys Chem C 2012;116:24476–81.

[455] Wang H, Liu J, Shen Z., Solid Electrolyte Interphase and Nitrogen Doping Effect on Potassium Storage Mechanism in Graphite. ECS Meeting Abstracts; MA2018-01:450, 2018. 10.1149/MA2018-01/3/450.

[456] Fondard J, Irisarri E, Courrèges C, Palacín MR, Ponrouch A, Dedryvère R. SEI composition on hard carbon in Na-ion batteries after long cycling: influence of salts (NaPF$_6$, NaTFSI) and additives (FEC, DMCF). J Electrochem Soc 2020;167: 070526.

[457] Eshetu GG, Diemant T, Hekmatfar M, Grugeon S, Behm RJ, Laruelle S, et al. Impact of the electrolyte salt anion on the solid electrolyte interphase formation in sodium ion batteries. Nano Energy 2019;55:327–40.

[458] Soto FA, Yan P, Engelhard MH, Marzouk A, Wang C, Xu G, et al. Tuning the solid electrolyte interphase for selective Li-and Na-ion storage in hard carbon. Adv Mater 2017;29:1606860.

[459] Xiao B, Soto FA, Gu M, Han KS, Song J, Wang H, et al. Lithium-pretreated hard carbon as high-performance sodium-ion battery anodes. Adv Energy Mater 2018; 8:1801441.

[460] Bai P, He Y, Zou X, Zhao X, Xiong P, Xu Y. Elucidation of the sodium-storage mechanism in hard carbons. Adv Energy Mater 2018;8:1703217.

[461] Kim H, Hong J, Park Y-U, Kim J, Hwang I, Kang K. Sodium storage behavior in natural graphite using ether-based electrolyte systems. Adv Funct Mater 2015;25: 534–41.

[462] Bai P, He Y, Xiong P, Zhao X, Xu K, Xu Y. Long cycle life and high rate sodium-ion chemistry for hard carbon anodes. Energy Storage Mater 2018;13:274–82.

[463] Komaba S, Ishikawa T, Yabuuchi N, Murata W, Ito A, Ohsawa Y. Fluorinated ethylene carbonate as electrolyte additive for rechargeable Na batteries. ACS Appl Mater Interfaces 2011;3:4165–8.

[464] Bie X, Kubota K, Hosaka T, Chihara K, Komaba S. A novel K-ion battery: hexacyanoferrate (II)/graphite cell. J Mater Chem A 2017;5:4325–30.

[465] Katorova NS, Luchkin SY, Rupasov DP, Abakumov AM, Stevenson KJ. Origins of irreversible capacity loss in hard carbon negative electrodes for potassium-ion batteries. J Chem Phys 2020;152:194704.

[466] Sawicki M, Shaw LL. Advances and challenges of sodium ion batteries as post lithium ion batteries. RSC Adv 2015;5:53129–54.

[467] Rangom Y, Gaddam RR, Duignan TT, Zhao X. Improvement of hard carbon electrode performance by manipulating SEI formation at high charging rates. ACS Appl Mater Interfaces 2019;11:34796–804.

[468] Lim DG, Kim K, Razdan M, Diaz R, Osswald S, Pol VG. Lithium storage in structurally tunable carbon anode derived from sustainable source. Carbon 2017; 121:134–42.

[469] Nakadaira M, Saito R, Kimura T, Dresselhaus G, Dresselhaus M. Excess Li ions in a small graphite cluster. J Mater Res 1997;12:1367–75.

[470] Cheng F, Liang J, Zhao J, Tao Z, Chen J. Biomass waste-derived microporous carbons with controlled texture and enhanced hydrogen uptake. Chem Mater 2008;20:1889–95.

[471] Cheng Q, Tamura N. Boron-doped activated carbon material. WO2016157508A1. 2016.

[472] Wu XL, Chen LL, Xin S, Yin YX, Guo YG, Kong QS, et al. Preparation and Li storage properties of hierarchical porous carbon fibers derived from alginic acid. ChemSusChem 2010;3:703–7.

[473] Mabuchi A. A survey on the carbon anode materials for rechargeable lithium batteries. TANSO 1994;1994:298–306.

[474] Hwang YJ, Jeong SK, Nahm KS, Shin JS, Stephan AM. Pyrolytic carbon derived from coffee shells as anode materials for lithium batteries. J Phys Chem Solids 2007;68:182–8.

[475] Fong R, Von Sacken U, Dahn JR. Studies of lithium intercalation into carbons using nonaqueous electrochemical cells. J Electrochem Soc 1990;137:2009–13.

[476] Kikuchi M, Ikezawa Y, Takamura T. Surface modification of pitch-based carbon fibre for the improvement of electrochemical lithium intercalation. J Electroanal Chem 1995;396:451–5.

[477] Xie H, Wu Z, Wang Z, Qin N, Li Y, Cao Y, et al. Solid electrolyte interface stabilization via surface oxygen species functionalization in hard carbon for superior performance sodium-ion batteries. J Mater Chem A 2020;8:3606–12.

[478] Buiel E, Dahn JR. Reduction of the irreversible capacity in hard-carbon anode materials prepared from sucrose for Li-ion batteries. J Electrochem Soc 1998;145: 1977–81.

[479] Béguin F, Chevallier F, Vix C, Saadallah S, Rouzaud JN, Frackowiak E. A better understanding of the irreversible lithium insertion mechanisms in disordered carbons. J Phys Chem Solids 2004;65:211–7.

[480] Ohzawa Y, Yamanaka Y, Naga K, Nakajima T. Pyrocarbon-coating on powdery hard-carbon using chemical vapor infiltration and its electrochemical characteristics. J Power Sources 2005;146:125–8.

[481] Irisarri E, Ponrouch A, Palacin MR. Review—hard carbon negative electrode materials for sodium-ion batteries. J Electrochem Soc 2015;162:A2476–82.

[482] Papanek P, Radosavljević M, Fischer J. Lithium insertion in disordered carbon–hydrogen alloys: intercalation vs covalent binding. Chem Mater 1996;8:1519–26.

[483] Tao L, Liu L, Chang R, He H, Zhao P, Liu J. Structural and interface design of hierarchical porous carbon derived from soybeans as anode materials for potassium-ion batteries. J Power Sources 2020;463:228172.

[484] Lu H, Chen X, Jia Y, Chen H, Wang Y, Ai X, et al. Engineering Al$_2$O$_3$ atomic layer deposition: enhanced hard carbon-electrolyte interface towards practical sodium ion batteries. Nano Energy 2019;64:103903.

[485] Lu W, Liang L, Sun X, Sun X, Wu C, Hou L, et al. Recent progresses and development of advanced atomic layer deposition towards high-performance Li-ion batteries. Nanomaterials 2017;7.

[486] Tatsumi K, Conard J, Nakahara M, Menu S, Lauginie P, Sawada Y, et al. ^{7}Li NMR studies on a lithiated non-graphitizable carbonfibre at low temperatures. Chem Commun 1997;687–8.

[487] Nagao M, Pitteloud C, Kamiyama T, Otomo T, Itoh K, Fukunaga T, et al. Structure characterization and lithiation mechanism of nongraphitized carbon for lithium secondary batteries. J Electrochem Soc 2006;153:A914–9A9.

[488] Hardwick LJ, Ruch PW, Hahn M, Scheifele W, Kötz R, Novák P. In situ Raman spectroscopy of insertion electrodes for lithium-ion batteries and supercapacitors: First cycle effects. J Phys Chem Solids 2008;69:1232–7.

[489] Wu Z, Wang L, Huang J, Zou J, Chen S, Cheng H, et al. Loofah-derived carbon as an anode material for potassium ion and lithium ion batteries. Electrochim Acta 2019;306:446–53.

[490] Stevens DA, Dahn JR. High capacity anode materials for rechargeable sodium-ion batteries. J Electrochem Soc 2000;147:1271.

[491] Kubota K, Shimadzu S, Yabuuchi N, Tominaka S, Shiraishi S, Abreu-Sepulveda M, et al. Structural analysis of sucrose-derived hard carbon and correlation with the electrochemical properties for lithium, sodium, and potassium insertion. Chem Mater 2020;32:2961–77.

[492] Su X, Dogan F, Ilavsky J, Maroni VA, Gosztola DJ, Lu W. Mechanisms for lithium nucleation and dendrite growth in selected carbon allotropes. Chem Mater 2017; 29:6205–13.

[493] Bommier C, Surta TW, Dolgos M, Ji X. New mechanistic insights on Na-ion storage in nongraphitizable carbon. Nano Lett 2015;15:5888–92.

[494] Wang K, Jin Y, Sun S, Huang Y, Peng J, Luo J, et al. Low-cost and high-performance hard carbon anode materials for sodium-ion batteries. ACS Omega 2017;2:1687–95.

[495] Zhang N, Liu Q, Chen W, Wan M, Li X, Wang L, et al. High capacity hard carbon derived from lotus stem as anode for sodium ion batteries. J Power Sources 2018; 378:331–7.

[496] Wang P, Zhu X, Wang Q, Xu X, Zhou X, Bao J. Kelp-derived hard carbons as advanced anode materials for sodium-ion batteries. J Mater Chem A 2017;5: 5761–9.

[497] Rybarczyk MK, Li Y, Qiao M, Hu Y-S, Titirici M-M, Lieder M. Hard carbon derived from rice husk as low cost negative electrodes in Na-ion batteries. J Energy Chem 2019;29:17–22.

[498] Guo H, Sun K, Lu Y, Wang H, Ma X, Li Z, et al. Hard carbons derived from pine nut shells as anode materials for Na-ion batteries. Chin Phys B 2019;28:068203.

[499] Liu P, Li Y, Hu Y-S, Li H, Chen L, Huang X. A waste biomass derived hard carbon as a high-performance anode material for sodium-ion batteries. J Mater Chem A 2016;4:13046–52.

[500] Zhang F, Yao Y, Wan J, Henderson D, Zhang X, Hu L. High temperature carbonized grass as a high performance sodium ion battery anode. ACS Appl Mater Interfaces 2017;9:391–7.

[501] Jian Z, Bommier C, Luo L, Li Z, Wang W, Wang C, et al. Insights on the mechanism of Na-ion storage in soft carbon anode. Chem Mater 2017;29:2314–20.

[502] Anji Reddy M, Helen M, Groß A, Fichtner M, Euchner H. Insight into sodium insertion and the storage mechanism in hard carbon. ACS Energy Lett 2018;3: 2851–7.

[503] Komaba S, Murata W, Ishikawa T, Yabuuchi N, Ozeki T, Nakayama T, et al. Electrochemical Na insertion and solid electrolyte interphase for hard-carbon electrodes and application to Na-ion batteries. Adv Funct Mater 2011;21: 3859–67.

[504] Stratford JM, Allan PK, Pecher O, Chater PA, Grey CP. Mechanistic insights into sodium storage in hard carbon anodes using local structure probes. Chem Commun 2016;52:12430–3.

[505] Wang Z, Huang X, Chen L. Lithium insertion/extraction in pyrolyzed phenolic resin. J Power Sources 1999;81:328–34. https://doi.org/10.1016/S0378-7753 (99)00262-1.

[506] Wang Z, Huang X, Xue R, Chen L. A new possible mechanism of lithium insertion and extraction in low-temperature pyrolytic carbon electrode. Carbon 1999;37: 685–92.

[507] Zhang B, Ghimbeu CM, Laberty C, Vix-Guterl C, Tarascon JM. Correlation between microstructure and Na storage behavior in hard carbon. Adv Energy Mater 2016;6:1501588.

[508] Kano A, Hojo N, Ito S, Fujimoto M, Nakura K. New carbon materials with large closed pore volume as anode for high energy Na-ion batteries. 228th ECS Meeting Phoenix. The Electrochemical Society; 2015. p. 221.

[509] Kano A, Okano T, Hojo N, Ito S, Fujimoto M, Nakura K. New carbon materials with large closed pore volume for the anode of high energy Na-ion batteries. Meeting Abstracts, MA2016-02. The Electrochemical Society; 2016. p. 668. https://doi.org/10.1149/MA2016-02/5/668.

[510] Kamiyama A, Kubota K, Nakano T, Fujimura S, Shiraishi S, Tsukada H, et al. High-capacity hard carbon synthesized from macroporous phenolic resin for sodium-ion and potassium-ion battery. ACS Appl Energy Mater 2020;3:135–40.

[511] Chen C, Wu M, Wang Y, Zaghib K. Insights into pseudographite-structured hard carbon with stabilized performance for high energy K-ion storage. J Power Sources 2019;444:227310.

[512] Li W, Li Z, Zhang C, Liu W, Han C, Yan B, et al. Hard carbon derived from rice husk as anode material for high performance potassium-ion batteries. Solid State Ionics 2020;351:115319.

[513] Qian Y, Jiang S, Li Y, Yi Z, Zhou J, Tian J, et al. Understanding mesopore volume-enhanced extra-capacity: Optimizing mesoporous carbon for high-rate and long-life potassium-storage. Energy Storage Materials 2020;29:341–9.

[514] Jian Z, Xing Z, Bommier C, Li Z, Ji X. Hard carbon microspheres: potassium-ion anode versus sodium-ion anode. Adv Energy Mater 2016;6:1501874.

[515] Yang J, Ju Z, Jiang Y, Xing Z, Xi B, Feng J, et al. Enhanced capacity and rate capability of nitrogen/oxygen dual-doped hard carbon in capacitive potassium-ion storage. Adv Mater 2018;30:1700104.

[516] Wu X, Xing Z, Hu Y, Zhang Y, Sun Y, Ju Z, et al. Effects of functional binders on electrochemical performance of graphite anode in potassium-ion batteries. Ionics 2019;25:2563–74.

[517] Adams RA, Varma A, Pol VG. Temperature dependent electrochemical performance of graphite anodes for K-ion and Li-ion batteries. J Power Sources 2019;410-411:124–31.

[518] Yang J, Ju Z, Jiang Y, Xing Z, Xi B, Feng J, et al. Enhanced capacity and rate capability of nitrogen/oxygen dual-doped hard carbon in capacitive potassium-ion storage. Adv Mater 2018;30:1700104.

[519] Jiang Q, Zhang Z, Yin S, Guo Z, Wang S, Feng C. Biomass carbon micro/nano-structures derived from ramie fibers and corncobs as anode materials for lithium-ion and sodium-ion batteries. Appl Surf Sci 2016;379:73–82.

[520] Elizabeth I, Singh BP, Trikha S, Gopukumar S. Bio-derived hierarchically macro-meso-micro porous carbon anode for lithium/sodium ion batteries. J Power Sources 2016;329:412–21.

[521] Luna-Lama F, Rodríguez-Padrón D, Puente-Santiago AR, Muñoz-Batista MJ, Caballero A, Balu AM, et al. Non-porous carbonaceous materials derived from coffee waste grounds as highly sustainable anodes for lithium-ion batteries. J Cleaner Prod 2019;207:411–7.

[522] Mullainanathan V, Sathish R, Kalaiselvi N. Coir pith derived bio-carbon: demonstration of potential anode behavior in Lithium-ion batteries. Electrochim Acta 2017;225:143–50.

[523] Gao G, Cheong L-Z, Wang D, Shen C. Pyrolytic carbon derived from spent coffee grounds as anode for sodium-ion batteries. Carbon Res Conv 2018;1:104–8.

[524] Liu T, Luo R, Qiao W, Yoon S-H, Mochida I. Microstructure of carbon derived from mangrove charcoal and its application in Li-ion batteries. Electrochim Acta 2010; 55:1696–700.

[525] Wang L, Schnepp Z, Titirici MM. Rice husk-derived carbon anodes for lithium ion batteries. J Mater Chem A 2013;1:5269–73.

[526] Zhang Y, Zhang F, Li G-D, Chen J-S. Microporous carbon derived from pinecone hull as anode material for lithium secondary batteries. Mater Lett 2007;61: 5209–12.

[527] Lv W, Wen F, Xiang J, Zhao J, Li L, Wang L, et al. Peanut shell derived hard carbon as ultralong cycling anodes for lithium and sodium batteries. Electrochim Acta 2015;176:533–41.

[528] Zhang X, Hu J, Chen X, Zhang M, Huang Q, Du X, et al. Microtubular carbon fibers derived from bamboo and wood as sustainable anodes for lithium and sodium ion batteries. J Porous Mater 2019;26:1821–30.

[529] Xiang J, Lv W, Mu C, Zhao J, BJJoA Wang. Activated hard carbon from orange peel for lithium/sodium ion battery anode with long cycle life. J Alloys Compd 2017;701:870–4.

[530] Selvamani V, Ravikumar R, Suryanarayanan V, Velayutham D, Gopukumar S. Fish scale derived nitrogen doped hierarchical porous carbon—a high rate performing anode for lithium ion cell. Electrochim Acta 2015;182:1–10.

[531] Niu J, Shao R, Liang J, Dou M, Li Z, Huang Y, et al. Biomass-derived mesopore-dominant porous carbons with large specific surface area and high defect density as high performance electrode materials for Li-ion batteries and supercapacitors. Nano Energy 2017;36:322–30.

[532] Han S-W, Jung D-W, Jeong J-H, Oh E-S. Effect of pyrolysis temperature on carbon obtained from green tea biomass for superior lithium ion battery anodes. Chem Eng J 2014;254:597–604.

[533] Caballero A, Hernán L, Morales J. Limitations of disordered carbons obtained from biomass as anodes for real lithium-ion batteries. ChemSusChem 2011;4: 658–63.

[534] Ou J, Zhang Y, Chen L, Yuan H, Xiao D. Heteroatom doped porous carbon derived from hair as an anode with high performance for lithium ion batteries. RSC Adv 2014;4:63784–91.

[535] Campbell B, Ionescu R, Favors Z, Ozkan CS, Ozkan M. Bio-derived, binderless, hierarchically porous carbon anodes for Li-ion batteries. Sci Rep 2015;5:14575.

[536] Nagalakshmi M, Kalaiselvi N. Mesoporous dominant cashewnut sheath derived bio-carbon anode for LIBs and SIBs. Electrochim Acta 2019;304:175–83. https://doi.org/10.1016/j.electacta.2019.02.123.

[537] Tao L, Zheng Y, Zhang Y, Ma H, Di M, Zheng Z. Liquefied walnut shell-derived carbon nanofibrous mats as highly efficient anode materials for lithium ion batteries. RSC Adv 2017;7:27113–20.

[538] Sun N, Liu H, Xu B. Facile synthesis of high performance hard carbon anode materials for sodium ion batteries. J Mater Chem A 2015;3:20560–6.

[539] Mullaivananathan V, Packiyalakshmi P, Kalaiselvi N. Multifunctional bio carbon: a coir pith waste derived electrode for extensive energy storage device applications. RSC Adv 2017;7:23663–70.

[540] Rath PC, Patra J, Huang HT, Bresser D, Wu TY, Chang JK. Carbonaceous anodes derived from sugarcane bagasse for sodium-ion batteries. ChemSusChem 2019; 12:2302–9.

[541] Zhang F, Yao Y, Wan J, Henderson D, Zhang X, Hu L. High temperature carbonized grass as a high performance sodium ion battery anode. ACS Appl Mater Interfaces 2016;9:391–7.

[542] Nakabayashi K, Dabin C, Han Y, Oh J, Miyawaki J, Yoon S-H. Structural effects on the enhancement of first-cycle Coulombic efficiency of mangrove-derived hard carbon as an anode material in sodium ion batteries. SN Appl Sci 2019;1:177.

[543] Wang Q, Zhu X, Liu Y, Fang Y, Zhou X, Bao J. Rice husk-derived hard carbons as high-performance anode materials for sodium-ion batteries. Carbon 2018;127: 658–66.

[544] Dahbi M, Kiso M, Kubota K, Horiba T, Chafik T, Hida K, et al. Synthesis of hard carbon from argan shells for Na-ion batteries. J Mater Chem A 2017;5:9917–28.

[545] Wu L, Buchholz D, Vaalma C, Giffin GA, Passerini S. Apple-biowaste-derived hard carbon as a powerful anode material for Na-ion Batteries. ChemElectroChem 2016;3:292–8.

[546] Meng X, Savage PE, Deng D. Trash to treasure: from harmful algal blooms to high-performance electrodes for sodium-ion batteries. Environ Sci Technol 2015;49: 12543–50.

[547] Qin D, Chen S. A sustainable synthesis of biomass carbon sheets as excellent performance sodium ion batteries anode. J Solid State Electrochem 2017;21: 1305–12.

[548] Li X, Liang J, Hou Z, Zhu Y, Qian Y. Recycling chicken eggshell membranes for high-capacity sodium battery anodes. RSC Adv 2014;4:50950–4.

[549] Wahid M, Gawli Y, Puthusseri D, Kumar A, Shelke MV, Ogale S. nutty carbon: morphology replicating hard carbon from walnut shell for Na ion battery anode. ACS Omega 2017;2:3601–9.

[550] Xu S-D, Zhao Y, Liu S, Ren X, Chen L, Shi W, et al. Curly hard carbon derived from pistachio shells as high-performance anode materials for sodium-ion batteries. J Mater Sci 2018;53:12334–51.

[551] Zheng P, Liu T, Yuan X, Zhang L, Liu Y, Huang J, et al. Enhanced performance by enlarged nano-pores of holly leaf-derived lamellar carbon for sodium-ion battery anode. Sci Rep 2016;6:26246.

[552] Shen F, Zhu H, Luo W, Wan J, Zhou L, Dai J, et al. Chemically crushed wood cellulose fiber towards high-performance sodium-ion batteries. ACS Appl Mater Interfaces 2015;7:23291–6.

[553] Cao W, Zhang E, Wang J, Liu Z, Ge J, Yu X, et al. Potato derived biomass porous carbon as anode for potassium ion batteries. Electrochim Acta 2019;293:364–70.

[554] Yang M, Dai J, He M, Duan T, Yao W. Biomass-derived carbon from Ganoderma lucidum spore as a promising anode material for rapid potassium-ion storage. J Colloid Interface Sci 2020;567:256–63.

[555] Gao C, Wang Q, Luo S, Wang Z, Zhang Y, Liu Y, et al. High performance potassium-ion battery anode based on biomorphic N-doped carbon derived from walnut septum. J Power Sources 2019;415:165–71.

[556] Xu B, Qi S, Li F, Peng X, Cai J, Liang J, et al. Cotton-derived oxygen/sulfur co-doped hard carbon as advanced anode material for potassium-ion batteries. Chin Chem Lett 2020;31:217–22.

[557] Prabakar SJR, Han SC, Park C, Bhairuba IA, Reece MJ, Sohn K-S, et al. Spontaneous formation of interwoven porous channels in hard-wood-based hard-carbon for high-performance anodes in potassium-ion batteries. J Electrochem Soc 2017;164:A2012–6.

[558] Ellingsen LA-W, Hung CR, Strømman AH. Identifying key assumptions and differences in life cycle assessment studies of lithium-ion traction batteries with focus on greenhouse gas emissions. Transp Res Part D: Transp Environ 2017;55: 82–90.

[559] Shinogi Y, Kanri Y. Pyrolysis of plant, animal and human waste: physical and chemical characterization of the pyrolytic products. Bioresour Technol 2003;90: 241–7.

[560] Heitkötter J, Marschner B. Interactive effects of biochar ageing in soils related to feedstock, pyrolysis temperature, and historic charcoal production. Geoderma 2015;245:56–64.

[561] Arundale RA, Bauer S, Haffner FB, Mitchell VD, Voigt TB, Long SP. Environment has little effect on biomass biochemical composition of miscanthus × giganteus across soil types, nitrogen fertilization, and times of harvest. BioEnergy Res 2015; 8:1636–46.

[562] Azar C, Lindgren K, Larson E, Möllersten K. Carbon capture and storage from fossil fuels and biomass – costs and potential role in stabilizing the atmosphere. Clim Change 2006;74:47–79.

[563] Schmidt H-P, Anca-Couce A, Hagemann N, Werner C, Gerten D, Lucht W, et al. Pyrogenic carbon capture and storage. GCB Bioenergy 2019;11:573–91.

[564] Sayre R. Microalgae: the potential for carbon capture. Bioscience 2010;60:722–7.

[565] Mathews JA. Carbon-negative biofuels. Energy Policy 2008;36:940–5.

[566] Searchinger TD. Biofuels and the need for additional carbon. Environ Res Lett 2010;5:024007.

[567] Abbasi T, Abbasi SA. Biomass energy and the environmental impacts associated with its production and utilization. Renew Sustain Energy Rev 2010;14:919–37.

[568] Sterner M, Fritsche U. Greenhouse gas balances and mitigation costs of 70 modern Germany-focused and 4 traditional biomass pathways including land-use change effects. Biomass Bioenergy 2011;35:4797–814.

[569] Blanco-Canqui H, Lal R. Crop residue removal impacts on soil productivity and environmental quality. Crit Rev Plant Sci 2009;28:139–63.

Niloofar Soltani received her M.S. in Materials Science and Engineering from Sharif University of Technology, Iran. She obtained her Ph.D. in material science from the National Polytechnic Institute -CINVESTAV, Mexico and during her Ph. D., she joined Professor Aleksander Gurlo's group at Berlin Institute of Technology for 7 months. She then moved to the National Autonomous University of Mexico (UNAM) to work as a postdoctoral research fellow. She was later awarded the "Leibniz-DAAD and then Alexander von Humboldt Fellowship" working in Leibniz Institute for Solid State and Materials Research in Dresden, Germany. Her present research activities focus on synthesizing of new anode materials for Li-ion batteries.

Amin Bahrami is an Alexander von Humboldt Research Fellow at Leibniz Institut für Festkörper- und Werkstoffforschung Dresden (IFW), Germany. In 2016 he received his Ph.D. in Materials Science from CINVESTAV-IPN (México). He worked as a post-doctoral researcher at Universidad Nacional Autónoma de México (UNAM) until end of 2018. His present research activity is focused on the synthesis of new bulk and thin film thermoelectric materials. He has been engaged in several research projects, and authored or co-authored more than 35 academic papers in high level international journals.

Lars Giebeler studied chemistry at the Universities of Gießen and Leipzig and received his doctoral degree from the Materials Science's Institute at TU Darmstadt under supervision of Prof. Hartmut Fueß. After his postdoctoral research at the KU Leuven (Prof. Johan Martens) and at the TU Darmstadt (Prof. Christian Hess), he joined the Leibniz Institute for Solid State and Materials Research (IFW) Dresden's Institute of Complex Materials in 2009 and has become group leader in 2011. In 2018 he joined EXCOR Korrosionsforschung GmbH and after a two years period he has taken the central X-ray diffraction facility of the IFW Dresden over in December 2020. His research interests focus on active (nanosized) materials for technically relevant applications, operando diffraction and spectroscopy techniques

Thomas Gemming obtained a diploma in physics at the Karlsruhe Institute of Technology, Germany, in 1994 on the topic of electro ceramics. In 1998 he received his doctoral degree in chemistry from the University Stuttgart, Germany. From 1994 to 2000 he worked at the Max-Planck-Institute for Metal Research in Stuttgart. In 2000 he joined the Leibniz Institute for Solid State and Material Research (IFW) Dresden where he is currently heading the IKM-Division Structure Analytics and the Department for Micro- and Nanostructures. From 2015 to 2019 he served as acting director of the Institute for Complex Materials. Furthermore, he has been the Executive Secretary of the German Society for Electron Microscopy since 2006. His research interests center around microscopy, spectroscopy, and the understanding of the microscopic principles of the function of electronic and chemically active materials and devices e.g. for energy applications.

Daria Mikhailova has obtained a diploma in chemistry in 1996 and a PhD degree in chemistry in 2000 at the Moscow State University, Russia. Her research included physical and chemical aspects of solid-state synthesis of high-temperature superconductors with target cationic and anionic stoichiometries. From 2005 to 2010, she did a post-doctoral work at the Technical University of Darmstadt, Germany, on the field of high-pressure synthesis and characterization of novel magnetic transition metal oxides as well as synthesis and electrochemical characterization of new cathode materials for Li-ion batteries. From 2011 to 2017, she worked as a senior scientist at the Max Planck Institute of Chemical Physics of Solids in Dresden, Germany, and at the Karlsruhe Institute for Technology, Germany. Her research dealt with studies of novel oxides for magnetic and electrochemical applications. From 2017, she is working at the Leibniz Institute for Solid State and Materials Research in Dresden, Germany, in the electrochemical energy storage group, and from 2018 she is the head of the group. Her research focuses on development of metal-ion batteries and supercapacitors including all cell components as cathodes, anodes, binder and electrolytes.